Nonlinear pulse propagation in nanoscale waveguides

Niet-lineaire pulspropagatie in nanoschaal golfgeleiders

Samenstelling van de promotiecommissie:

prof. dr. L. Kuipers (promotor)	Universiteit Twente
prof. dr. C. Lienau	Universität Oldenburg
prof. dr. J. I. Dijkhuis	Universiteit Utrecht
prof. dr. K. J. Boller	Universiteit Twente
prof. dr. J. L. Herek	Universiteit Twente
prof. dr. W. L. Vos	Universiteit Twente

This research is part of the research program of the
Foundation for Fundamental Research on Matter (FOM),
which is financially supported by the
Netherlands Organisation for Scientific Research (NWO).

This work was carried out at:
NanoOptics Group,
FOM Institute for Atomic and Molecular Physics (AMOLF)
Science Park 104, 1098 XG Amsterdam, The Netherlands,
where a limited number of copies of this thesis is available.

Cover: Artist impresssion of a soliton propagating in a photonic crystal waveguide, drawn by Henk-Jan Boluijt.

ISBN: 978-90-77209-88-2

Nonlinear pulse propagation in nanoscale waveguides

PROEFSCHRIFT

ter verkrijging van
de graad van doctor aan de Universiteit Twente,
op gezag van de rector magnificus,
prof. dr. H. Brinksma,
volgens besluit van het College voor Promoties
in het openbaar te verdedigen
op vrijdag 23 januari 2015 om 12:45 uur

door

Matthias Wulf

geboren op 26 augustus 1982
te Holzminden, Duitsland

Dit proefschrift is goedgekeurd door:
prof. dr. L. (Kobus) Kuipers

To my parents

Contents

1

Introduction

ABSTRACT: In this chapter we describe the two different waveguiding platforms and strategies employed in this thesis to achieve an integration of nonlinear optical effects on chip. First, we describe the importance of light in optical communication systems. Thereafter, we introduce the concept of nonlinear optics and its potential for all-optical signal processing. In specific, we discuss the nonlinear optical effects, which will play an important role in this thesis, and how to improve their inherent low efficiency to enable an integration on chip. Finally, we describe the two approaches to enhance nonlinear optics, which are investigated in this thesis.

1.1 Light in the telecommunication era

Light plays a crucial role in the information era, since the intercontinental data traffic in the internet is based on optical communication systems [1]. Here, light pulses are used as information carriers and sent through optical fibers lying on the ground of the oceans. Optical communication is beneficial and widely used since it offers the largest bandwidth and allows for the prevention of power dissipation caused by ohmic losses in copper cables. At the moment, however, most signal processing is still performed using electronics, where the conversion between optical and electrical signals is one of the bottlenecks of optical communication systems. There is the possibility to increase the bandwidth of optical communication networks and lower their power dissipation by executing the signal processing all optically. The most promising approach to process optical communication signals all optically is by using nonlinear optical effects. As a result, thriving research effort exists to exploit nonlinear effects in waveguides to integrate all-optical signal-processing schemes on chip.

1.2 Light propagation in materials and nonlinear optics

When light enters a medium its electric field will polarize the material's atomic constituents. The response of the material, i.e., its polarization, will be a function of the applied electric field. Mathematically, this can be stated as the following [2]:

$$\begin{aligned} \mathrm{P}(\omega) = \epsilon_0[\chi^{(1)}(\omega_1)\mathrm{E}(\omega_1) + \chi^{(2)}(\omega_1,\omega_2)\mathrm{E}(\omega_1)\mathrm{E}(\omega_2) \\ +\chi^{(3)}(\omega_1,\omega_2,\omega_3)\mathrm{E}(\omega_1)\mathrm{E}(\omega_2)\mathrm{E}(\omega_3) + \ldots] \end{aligned} \tag{1.1}$$

where $\mathrm{P}(\omega)$ is the polarization of the matter, i.e., its dipole moment per volume, ϵ_0 the permittivity of vacuum and $\mathrm{E}(\omega)$ the applied electric field. The quantity $\chi^{(\mathrm{n})}$ is called the susceptibility of order n and describes the response of the matter. The regime in which only the term containing the first-order susceptibility is of importance is that of linear optics. Here, the refractive index n_0 of the material can be related to $\chi^{(1)}$:

$$n_0 = \sqrt{\epsilon_r} = \sqrt{1 + \chi^{(1)}}, \tag{1.2}$$

where we have assumed that the material is non-magnetic and ϵ_r is the material's relative permittivity or dielectric constant.

The case in which higher terms in Eq. (1.1) are required is the nonlinear optical regime. This happens when the electric field strength is so strong that the deflection of the electron from its unperturbed position in the atom cannot be modeled as a harmonic oscillator [3]. Consequently, the material polarization is no longer a linear function of the applied electric field.

The second-order susceptibility $\chi^{(2)}$ causes second-harmonic generation and sum- and difference-frequency generation [4]. These are all processes where the nonlinear response of the matter induces a new electric field, which has a different frequency content than that of the applied electric field. The third-order susceptibility $\chi^{(3)}$ is responsible for effects like third-harmonic generation, optical parametric amplification, four-wave mixing and an intensity-dependent refractive index [4].

Nonlinear optical effect are used today in a variety of different applications ranging from creating new light sources to new microscopy techniques, for example, for the investigation of biological samples [5]. Nonlinear optics also offers a promising route towards ultrafast all-optical communication [6], i.e., the control of light with light.

1.2.1 Nonlinear optical effects in waveguides

Only a few nonlinear optical effects are important in the scope of this thesis and will be discussed in this section. We confine ourselves to one pulse and the lowest order nonlinear effects which alter the pulse itself during its propagation. In practice, these effects stem from the third-order susceptibility $\chi^{(3)}$, since the second-order susceptibility is zero in most cases due to symmetry constraints, i.e., $\chi^{(2)}$ is only nonvanishing in structures which lack inversion symmetry. We will consider self-phase modulation (SPM) and two-photon absorption (2PA), which are both third-order nonlinear effects. Since 2PA is negligible in large band gap semiconductors, we also discuss three-photon absorption (3PA), the next higher order nonlinear absorption process after 2PA. In addition, we consider free-carrier effects, which are linear in themselves but a result of the nonlinear absorption pro-

cesses. Finally, we discuss the interaction of the various effects, which lead to temporal solitons and soliton fission events.

The most important nonlinear optical process that occurs virtually in every case of high intensity pulse propagation is SPM which deserves its name from the fact that the effect causes a pulse to modulate its own phase. SPM originates from the optical Kerr effect, which results from the real part of the third-order susceptibility. The optical Kerr effect is very often the lowest order nonlinear process and therefore the most dominant nonlinear effect which has to be considered. The Kerr effect causes an intensity-dependent refractive index [7]:

$$\mathrm{n(I)} \;=\; \mathrm{n_0} \;+\; \mathrm{n_2} \cdot \mathrm{I}, \tag{1.3}$$

where $\mathrm{n_0}$ is the refractive index valid for linear optics and I is the intensity applied to the nonlinear material. The Kerr coefficient $\mathrm{n_2}$ is a function of the third-order nonlinear susceptibility $\chi^{(3)}$:

$$\mathrm{n_2} \;=\; \frac{3\,\chi^{(3)}}{2\,\mathrm{n_0^2}\epsilon_0 \mathrm{c}}, \tag{1.4}$$

where c is the speed of light in vacuum.

In the case of the optical Kerr effect the intensity, which causes the change in the refractive index, is the intensity of the optical signal itself. Since the intensity of a pulse is a function of time, the refractive index will also become a function of time. As a consequence, the pulse experiences an additional time-dependent phase during propagation which alters its spectral density.

The reason for the change in the spectral density is easiest understood by using the concept of the instantaneous frequency, which is the temporal derivative of the phase experienced by the pulse [8]. Mathematically it holds that:

$$\omega(\mathrm{t}) \;=\; \frac{\mathrm{d}\phi(\mathrm{t})}{\mathrm{dt}} \;=\; \frac{\mathrm{d}(\omega_0 \cdot \mathrm{t} - \frac{2\pi}{\lambda_0}\mathrm{n(t)} \cdot \mathrm{z})}{\mathrm{dt}} \;=\; \omega_0 - \frac{2\pi \mathrm{z}}{\lambda_0}\frac{\mathrm{dn(t)}}{\mathrm{dt}} \tag{1.5}$$

where $\omega(\mathrm{t})$ is the instantaneous frequency, ω_0 is the carrier frequency and λ_0 is the central wavelength of the pulse. Therefore, any time-dependent refractive index will create new frequencies.

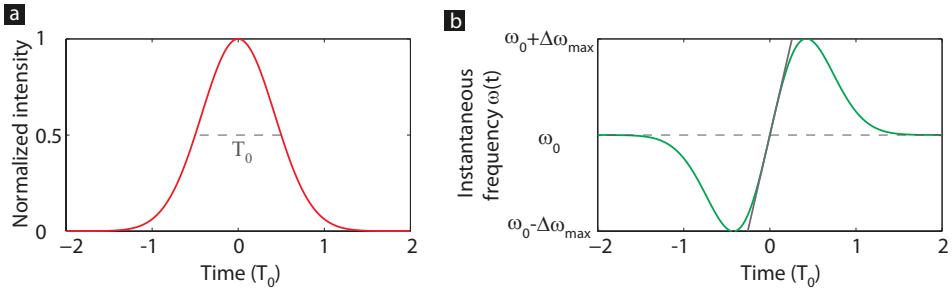

Figure 1.1: Effect of SPM on a pulse. a) Temporal envelope of a Gaussian shaped pulse with a FWHM of T_0*. b) Resulting time-varying instantaneous frequency, which shows a dip in frequency at the trailing edge of the pulse and a peak at the rising edge.*

Figure 1.1 illustrates the effect of SPM on the instantaneous frequency $\omega(t)$ of a Gaussian shaped pulse with a full width at half maximum (FWHM) of T_0. Since the pulse features a symmetric envelope, the changes in the instantaneous frequency will be symmetric around the center frequency ω_0. This symmetric broadening of the spectral density is a typical observation for SPM. As can be seen in Fig. 1.1b at the trailing pulse edge SPM causes a dip in frequency of $\omega(t)$, whereas at the rising edge SPM leads to a peak [9]. The exact amount of the spectral broadening, i.e., the change in frequency of $\Delta\omega_{max}$ at the peak and the dip in $\omega(t)$, depends on a variety of variables, including the Kerr coefficient, the peak intensity and the pulse width.

The Kerr effect is not the only nonlinear optical effect which is caused by the third-order susceptibility. Two-photon absorption (2PA) is caused by the imaginary part of $\chi^{(3)}$. As a result of the absorption the propagating light will lose intensity which can be described with:

$$\frac{dI(t,z)}{dz} = -\alpha_{nPA} \cdot I^n(z,t), \tag{1.6}$$

where α_{nPA} is the n-photon absorption coefficient. In the case that n is 2 we are talking about 2PA which scales quadratically with intensity. If n is 3 this equation describes three-photon absorption (3PA), which is based on the imaginary part of the fifth-order susceptibility.

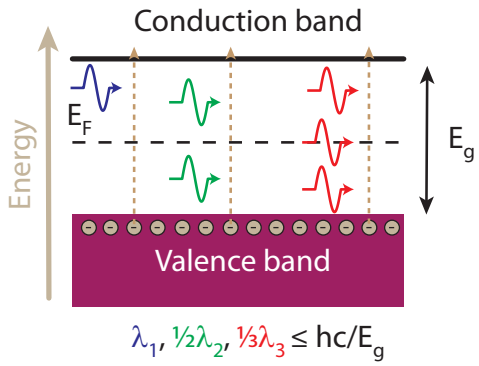

Figure 1.2: Schematic of multi-photon absorption processes in the energy diagram of a semiconductor. Here, electrons are excited from the valence to the conduction band. In the case of linear absorption only one photon is involved. For 2PA and 3PA two or three photons are simultaneously absorbed, respectively. Due to the different number of photons involved in the absorption, there is a different maximum wavelength for which absorption can occur.

In an absorption process the absorbed photons must have enough energy to raise an electron to an available free state. This typically means for a semiconductor that the electronic band gap has to be bridged (see Fig. 1.2) to raise an electron from the valence to the conduction band. In this case we speak about interband absorption. Thus, there is a maximum wavelength of light required before 2PA and 3PA can occur inside a medium. With the extra photon that is absorbed in 3PA compared to 2PA, 3PA can have an impact on pulse propagation in materials of larger bandgap energy, where the effect of 2PA is negligible at the considered wavelength.

Multi-photon absorption limits the peak intensity of a pulse that can be used since the decay increases with intensity. Hence, a nonlinear absorption process often restricts the impact of other nonlinear effects.

However, absorption processes are not only obstructive for nonlinear pulse propagation. They can also be used beneficially. Any absorption process generates free carriers, which in their turn alter the optical properties of the underlying material. In detail, there are two different free-carrier effects, the free-carrier absorption (FCA) and the free-carrier dispersion (FCD). FCA describes the fact that free electrons are able to absorb pho-

tons, whereas FCD represents a change of the refractive index due to free carriers [10]. It has been shown that free-carrier effects, besides offering rich interesting physics, can also be useful to implement optical devices like optical modulators [11, 12, 13] or optical delay lines [14, 15, 16].

In FCA there is no bandgap to bridge since the free electrons already occupy a partially empty band. Absorption of light leading to excitations within this band is called intraband absorption. Since in FCA a photon and a free electron interact the absorption process will be proportional to both the free-carrier density and the light intensity, leading to a decrease in light intensity as:

$$\frac{\mathrm{dI(t,z)}}{\mathrm{dz}} \;=\; -\sigma \mathrm{N_c(t)I(z,t)}, \tag{1.7}$$

where $\mathrm{N_c(t)}$ is the free-carrier density and σ the FCA cross-section.

FCD describes the process that the refractive index of the underlying material changes due to the presence of free carriers for which holds [17]:

$$\mathrm{n(t)} \;=\; \mathrm{n_0} + \mathrm{k_c N_c(t)}, \tag{1.8}$$

where $\mathrm{k_c}$ is the so-called FCD coefficient. In the case of pulse propagation there will be temporal dynamics in the free-carrier density. Free carriers will be generated by absorption processes, which might depend on the time-varying intensity. Further, the free-carrier density will decay with a lifetime τ_{rec} specific for the material due to recombination. This means that in the presence of 2PA and 3PA the time evolution of $\mathrm{N_c(t)}$ can be described by a rate equation:

$$\frac{\mathrm{dN(z,t)}}{\mathrm{dt}} \;=\; \frac{\alpha_{\mathrm{2PA}}}{2\hbar\omega_0}\mathrm{I^2(z,t)} \;+\; \frac{\alpha_{\mathrm{3PA}}}{3\hbar\omega_0}\mathrm{I^3(z,t)} \;-\; \frac{\mathrm{N_c(z,t)}}{\tau_{\mathrm{rec}}}, \tag{1.9}$$

where $\hbar$ is the Planck constant divided by 2π. Here, we have specifically assumed that linear absorption is negligible, as will typically be the case in dielectric waveguides. Moreover, free-carrier diffusion is neglected since it occurs on a much longer time scale than the duration of an ultrashort pulse.

1.2.2 Dispersion effects in waveguides

The strength of nonlinear optical effects in a waveguide depends on the peak intensity of the pulse propagating in it. The peak intensity of a pulse is related to its temporal length. If a pulse broadens temporally, the peak intensity decreases. Consequently, dispersion in a waveguide is of crucial importance, since it governs the temporal reshaping of the pulse.

Temporal reshaping will occur if the dispersion relation $k(\omega)$ of the mode in a waveguide is not simply proportional to ω, which is usually the case. To identify and describe the different effects which cause a change in the temporal shape of the pulse, the dispersion relation is expanded in a Taylor series:

$$k(\omega) = \beta_0 + \beta_1(\omega - \omega_0) + \frac{\beta_2}{2}(\omega - \omega_0)^2 + \frac{\beta_3}{6}(\omega - \omega_0)^3 + ... \quad (1.10)$$

The different expansion coefficients $\beta_n = d^n k(\omega)/d\omega^n|_{\omega=\omega_0}$ describe different contributions related to the temporal evolution of the pulse. β_0 is inversely proportional to the phase velocity v_ϕ ($\beta_0 = \omega_0/v_\phi$). A common way to describe the phase advance is the use of a refractive index or effective mode index n_{eff} in the case of waveguide. n_{eff} is defined as the ratio of the speed of light in vacuum to v_ϕ ($n_{eff} = c/v_\phi$). At the same time, the effective mode index describes the increase of the wavevector k_{eff} of the mode in comparison to the one of light in vacuum given by $k_0 = \omega/c$, i.e., $n_{eff} = k_{eff}/k_0$. The inverse of the group velocity v_g, where v_g determines the speed of the pulse envelope, is given by β_1 ($\beta_1 = 1/v_g$). An alternative way to characterize the group velocity is the group index n_g, which is defined as the ratio of the speed of light in vacuum to v_g ($n_g = c/v_g$). The term β_2 is related to group-velocity dispersion (GVD) that causes a symmetric temporal broadening of the pulse envelope. Third-order dispersion (TOD) is determined by β_3 and leads to an asymmetric broadening of the pulse. Higher terms in the Taylor expansion are usually much smaller and therefore neglected.

1.2.3 Modeling nonlinear pulse propagation

In a waveguide the described effects will not occur separately but at the same time. The common way to model the resulting complex interplay during nonlinear pulse propagation is by using the generalized nonlinear

Schrödinger equation (NLSE). This method semi-analytically describes how the envelope of a pulse changes as it experience a variety of effects during propagation. In general, there are three different categories of effects which might occur. The pulse may experience loss, it might change in phase or it might reshape. In the context of this thesis, the NLSE will take linear loss, dispersion, nonlinear effects and free-carrier effects into account. However, the NLSE could easily be expanded to include even more effects such as Raman or Brillouin scattering into the equation which are not considered here for the sake of simplicity. Thus, the NLSE takes the following form:

$$\begin{aligned}\frac{\partial \mathrm{A}}{\partial \mathrm{z}} =& -\frac{\alpha_{\mathrm{eff}}}{2}\mathrm{A} - \mathrm{i}\frac{\beta_2}{2}\frac{\partial^2 \mathrm{A}}{\partial \mathrm{t}^2} + \frac{\beta_3}{6}\frac{\partial^3 \mathrm{A}}{\partial \mathrm{t}^3} + \mathrm{i}\gamma_{\mathrm{eff}}|\mathrm{A}|^2\mathrm{A} - \frac{\alpha_{\mathrm{2PA,eff}}}{2}|\mathrm{A}|^2\mathrm{A} \\ & -\frac{\alpha_{\mathrm{3PA,eff}}}{2}|\mathrm{A}|^4\mathrm{A} + (\mathrm{i}k_0 k_{\mathrm{c,eff}} - \frac{\sigma_{\mathrm{eff}}}{2})\mathrm{N_c}\mathrm{A}, \end{aligned} \tag{1.11}$$

where A(z,t) is the slowly-varying envelope of the pulse, which is a complex quantity featuring an amplitude and a phase. We have omitted the spatial and temporal dependence of A(z,t) for the sake of brevity. Further, this equation is formulated in the moving reference frame, i.e., the time frame moves with the same group velocity as the pulse. This is done to eliminate the time shift caused by the group velocity and to focus on the reshaping of the envelope instead. A moving reference frame will be used in all NLSE calculations presented in this thesis.

Equation (1.11) consists of several terms, which describe different effects. There are three terms, which represent loss mechanisms leading to a decay of the amplitude of A(z,t). These are the linear loss term $-\alpha/2\mathrm{A}$ and the two multi-photon absorption processes 2PA and 3PA, that are taken into account by the terms $-\alpha_{\mathrm{2PA,eff}}/2|\mathrm{A}|^2\mathrm{A}$ and $-\alpha_{\mathrm{3PA,eff}}/2|\mathrm{A}|^4\mathrm{A}$, respectively. The effective 2PA and 3PA coefficients are given by their bulk values divided by an effective mode area characteristic for a third- and fifth-order nonlinear process, respectively, i.e.: $\alpha_{\mathrm{2PA,eff}} = \alpha_{\mathrm{2PA,bulk}}/\mathrm{A}_{\mathrm{3,eff}}$ and $\alpha_{\mathrm{3PA,eff}} = \alpha_{\mathrm{3PA,bulk}}/\mathrm{A}^2_{\mathrm{5,eff}}$. The term $\mathrm{i}\gamma_{\mathrm{eff}}|\mathrm{A}|^2\mathrm{A}$ describes the effect of SPM. Included here is the effective nonlinear parameter γ_{eff}, which consists out of the following terms $2\pi/\mathrm{A}_{\mathrm{3,eff}}\mathrm{n}_2$. The dispersion terms $-\mathrm{i}\beta_2/2\partial^2\mathrm{A}/\partial\mathrm{t}^2$ and $\beta_3/6\partial^3\mathrm{A}/\partial\mathrm{t}^3$ describe the effect of GVD and TOD, respectively. Finally, there are two terms given by $(\mathrm{i}k_0 k_{\mathrm{c,eff}} - \sigma_{\mathrm{eff}}/2)\mathrm{N_c}\mathrm{A}$ and related to free-carrier effects, namely FCA and FCA, which scale with the free-carrier density $\mathrm{N_c}$. FCA leads to a decay with propagation, whereas FCD causes

an additional phase experienced by the pulse, as discussed in the previous section.

In addition to the NSLE an auxiliary equation has to be solved, which considers the temporal evolution of the free-carrier density. For this, Eq. (1.9) is rewritten in terms of the pulse amplitude:

$$\frac{\mathrm{dN(z,t)}}{\mathrm{dt}} = \frac{\alpha_{\mathrm{2PA,eff}}}{2\hbar\omega_0 \mathrm{A}_{\mathrm{3,eff}}}|\mathrm{A(z,t)}|^4 + \frac{\alpha_{\mathrm{3PA,eff}}}{3\hbar\omega_0 \mathrm{A}_{\mathrm{5,eff}}}|\mathrm{A(z,t)}|^6 - \frac{\mathrm{N_c(z,t)}}{\tau_{\mathrm{rec}}}. \tag{1.12}$$

The NLSE is a nonlinear partial differential equation and can only be analytically solved in a limited number of cases. One example, where analytic solutions are available, is the description of soliton propagation. Here, the NLSE consists only of two terms, which consider GVD and SPM. In the general case, the NLSE has to be solved numerically. There are several possible approaches, the most common one is the split-step Fourier method (SSFM) [18]. Here, the NLSE gets separated in two pieces: a part that takes the nonlinear effects into account (including the linear losses) and a part that considers the dispersion effects. The solving of the NLSE gets split into two steps. First, the terms that take the nonlinear effects into account are solved in the time domain. Second, the dispersion effects are considered in the spectral domain. In this simplified approach the nonlinear effects and the dispersion are taken not to occur at the same time. Thus, it is assumed that the complete propagation distance can be stitched together out of periodically recurring pieces with length Δz, where only nonlinear or dispersion effects have to be taken into account. This approach has the advantage that easy solutions exist for the two separate steps of the algorithm. Moreover, the error of the SSFM can be made arbitrarily small by choosing an appropriate step size Δz. Finally, since the free-carrier density is coupled to the NLSE, the rate equation describing the evolution of $\mathrm{N_c}$ has to be solved concurrently, which can be achieved by, for example, a finite difference scheme.

1.2.4 Influence of free carriers during pulse propagation

It has been shown that free carriers can have a significant effect on pulse propagation in semiconductor waveguides. To illustrate this we consider and reproduce here an example from literature [19], where it is calculated

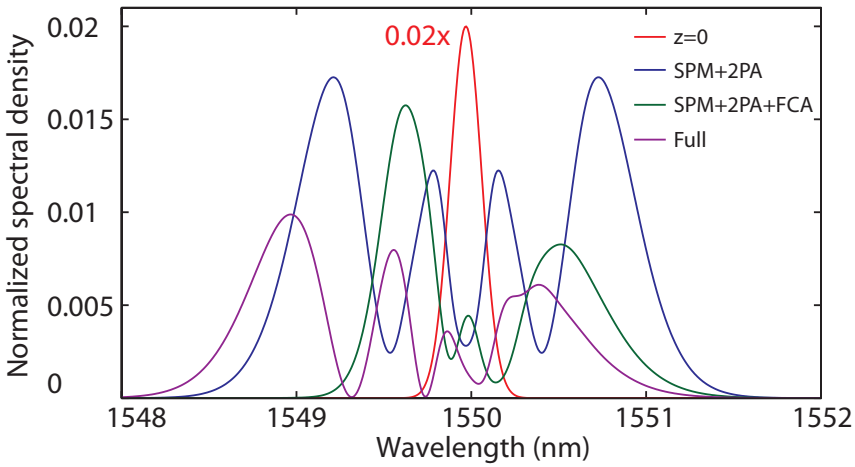

Figure 1.3: Evolution of the spectral density of a 10 ps pulse propagating through a waveguide. The original Gaussian shaped spectrum before propagation is shown as a red curve (scaled down by a factor of 0.02). If free-carrier effects are neglected SPM leads to a spectral density after propagation which is branched into four peaks despite the occurrence of 2PA (blue curve). Taking additionally FCA into account leads to an asymmetric spectrum (green curve). If FCD is also considered, the spectral density shows a shift to shorter wavelengths (purple curve).

how the spectral density of a 10 ps Gaussian shaped pulse changes after propagation through a 10 cm long silicon-on-insulator waveguide due to the generation of free carriers. Three different scenarios are considered and solved by using the NLSE. In the first scenario only GVD, linear loss, 2PA and SPM have an effect on the pulse evolution. For the next scenarios, first FCA is included and then finally also FCD is taken into account.

In the first case where only SPM is considered and no FC effects are included, the original Gaussian shaped spectrum (red curved) can be observed to broaden symmetrically leading to four peaks in the spectral density (blue curve) (cf. Fig. 1.3). In the second scenario, where FCD is additionally taken into account, less broadening than in the prior case can be observed (green curve). Further, the spectral density is broadened asymmetrically rather than symmetrically. The asymmetry of the spectral density is due to the fact that the free-carrier density, created by 2PA, builds up dur-

ing the pulse envelope and therefore different spectral components, which are propagating at different temporal positions inside the pulse envelope due to GVD, experience a FCA contribution with a different strength. In the last scenario, where FCD is also included, the spectral density of the pulse shows additionally a blueshift (purple curve). This wavelength shift is a signature of the FCD effect, where the refractive index gets temporally changed due to the time evolution of the free-carrier density.

1.2.5 Temporal soliton

A rich interplay of the various aforementioned effects can happen. Interestingly, for example, SPM and GVD can counteract and balance each other. A delicate interplay of both effects can lead to a class of nonlinear waves which show peculiar propagation behavior. These waves are called temporal solitons, or for the sake of simplicity just solitons [20]. Their propagation behavior is peculiar, because they do not temporally broaden with propagation, but instead remain unchanged or show a periodic evolution, sometimes called breathing.

There is a variety of solitons which are usually classified by an increasing ordering number. It can be shown that to create and sustain a certain soliton, so that GVD and SPM compensate each other, a defined peak intensity is required. The ordering number determines the intensity required to generate a soliton and describes its propagation behavior. The higher the order of a soliton is the more complex is its periodic evolution in the time and the frequency domain.

The order of a soliton is quantized to integer numbers and can be calculated by the following equation:

$$N = \sqrt{\frac{L_D}{L_{Nl}}} = \sqrt{\frac{2\pi n_2 P_0 T_0^2}{\lambda_0 A_{3,\mathrm{eff}} |\beta_2|}} \tag{1.13}$$

where P_0 is the peak intensity of the pulse, T_0 the temporal pulse length and β_2 is the GVD coefficient. The effective mode area $A_{3,\mathrm{eff}}$ describes the spatial confinement of the soliton, for example by guiding it inside a waveguide or optical fiber. The dispersion length $L_D = T_0^2/|\beta_2|$ determines the length after which GVD becomes significant. For a Gaussian pulse L_D equals the propagation distance after which the amplitude of the pulse has

broadened by a factor of $\sqrt{2}$ due to GVD. Analogously, a nonlinear length $L_{NL} = (\lambda A_{3,eff})/(2\pi n_2 P_0)$ is defined which describes the strength of SPM [8]. To generate a fundamental soliton (i.e. N=1) the dispersion length has to equal the nonlinear length. In the case of higher order solitons the nonlinear length has to be much smaller than the dispersion length. A fundamental soliton (N=1) is described by the following equation [20]:

$$A(x,t) = \sqrt{P'_0}\,\mathrm{sech}(\frac{t}{T_0})\exp(i\frac{x}{2L_D}) \tag{1.14}$$

where $P'_0 = \lambda_0 A_{3,eff}|\beta_2|/(2\pi n_2 T_0^2)$ is the peak intensity to create a fundamental soliton of wavelength λ_0 and temporal width T_0 for a given GVD and Kerr coefficient. It can be seen that the fundamental soliton has a hyperbolic secant shape in time and exhibits a harmonic phase evolution with propagation. Interestingly, the shape of the soliton does not change with propagation, which means that the wave packet does not suffer from temporal broadening although it propagates through a dispersive medium (see Fig. 1.4a). At the same time, also the spectrum of the pulse does not change as shown in Fig. 1.4b, in contrast to what will happen if only SPM occurs. That is, the dispersion and the optical Kerr effect exactly balance each other.

In contrast, higher-order solitons (i.e. $N > 1$) behave differently. In general, they feature a periodic evolution of both the temporal envelope and the spectrum with propagation distance. Figure 1.4c shows that in the case of a higher-order soliton the wave packet broadens and narrows periodically in time as it propagates. At the same time, the spectrum also shows periodic oscillations (cf. Fig. 1.4d). When the soliton is temporally compressed its spectrum is broadened and vice versa. It can be shown that the periodicity x_0 of a higher-order soliton is given by:

$$x_0 = \frac{\pi}{2} L_D. \tag{1.15}$$

In general, the periodic behavior of higher-order solitons becomes more complex with increasing order. As can be seen by comparing Fig. 1.4c-f this means they exhibit more features during one period.

Interestingly, solitons are quite robust to changes in the initial conditions. If, for example, the injected pulse has more energy than required for

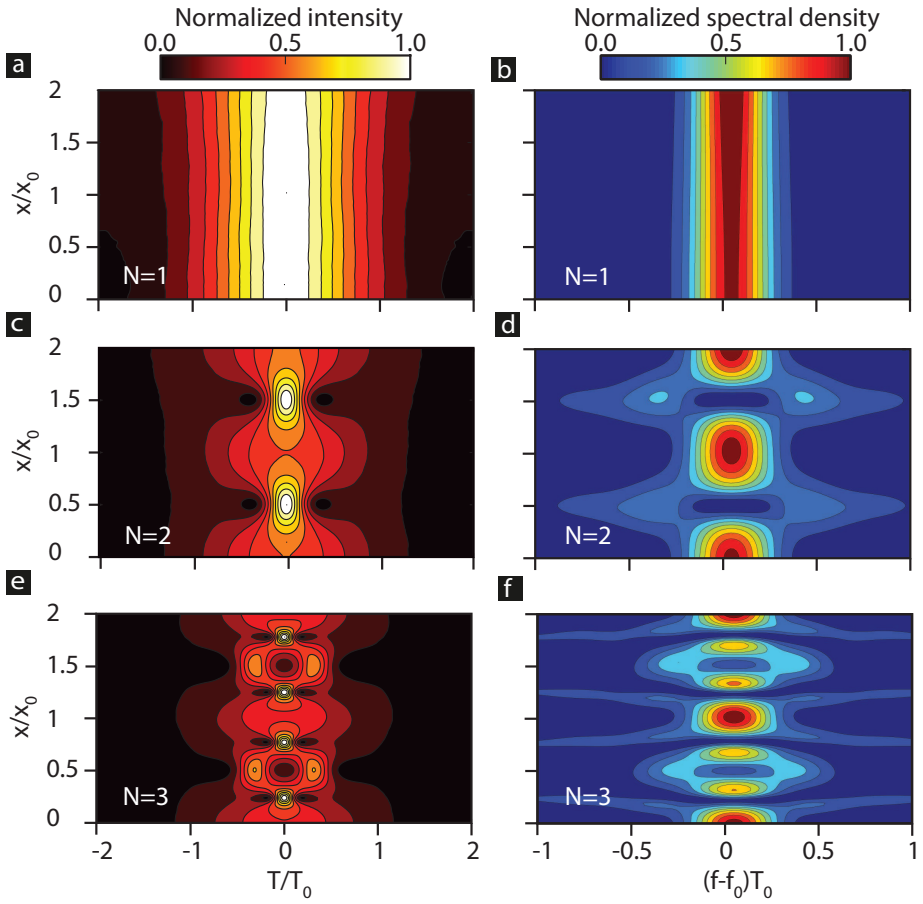

Figure 1.4: Temporal and spectral evolution of the three lowest order solitons propagating in a waveguide. A fundamental soliton (N = 1) does not show a change in the temporal (a) as well as the spectral domain (b). The second-order soliton (N = 2) shows a periodic behavior with propagation. In the time domain the pulse compresses and broadens (c), whereas the spectral density shows a concurrent broadening and narrowing (d). The behavior of the third-order soliton (N = 3) is also periodic with propagation in the time (e) and the spectral (f) domain, but features a more complex evolution during one period. All plots are normalized to their respective maxima amplitude to allow a better comparison of the temporal and spectral evolution.

the generation of a soliton, the wave packet will lose energy, by emitting dispersive radiation, until the soliton condition is fulfilled. If the injected pulse has a wrong shape, i.e., not a hyperbolic secant shape, the wave packet will reshape until a soliton is formed. Important to note is that other effects that affect pulse propagation, beside GVD and SPM, can perturb soliton propagation. In the case of a higher-order soliton this means that a soliton fission event can occur in which wave packets break apart into several other wave packets. In contrast, the fundamental soliton is robust against other effects and will not undergo fission. Physical effects, which have proven to cause a soliton fission event, are higher-order dispersion [21] and Raman scattering [22]. In chapter 4, we show that free-carrier effects in semiconductor waveguides can also cause a fission. It can be shown that the propagation distance, the fission length, after which such a fission event typically happens, is given by:

$$\mathrm{L_{fission}} = \frac{\mathrm{L_D}}{\mathrm{N}}. \tag{1.16}$$

Soliton fission events are instrumental in supercontinuum generation where spatially coherent "white" light sources are created [23], which feature extremely broad spectra. These light sources are used in a variety of different applications ranging from optical coherence tomography [24], frequency metrology [25], optical communications [26] and gas sensing [27].

1.3 Enhancing nonlinear optical effects

Generally, nonlinear optical effects are weak. However, they scale with powers of the intensity and propagation length. Thus, straightforward ways to improve their influence is to extend either the propagation distance, which prohibits compact optical devices, or increase the laser power, which represents a higher energy consumption. Thus, more clever approaches to increase the influence of the nonlinearities, so that they can be beneficially exploited in applications, are required.

One approach is to choose the right material, which features a strong nonlinear optical response. Different materials exhibit a different electronical configuration, which also governs the susceptibilities $\chi^{(n)}$. Consequently, choosing the proper material can enhance a nonlinear effect tremendously.

In photonics, the nonlinear properties of semiconductors are usually exploited, since mature fabrication techniques exist for these materials to create integrated photonic circuits.

At the same time absorption processes need to be minimized as they obstruct the efficient use of nonlinear effects. There are two ways to achieve this: a material is used, which either has a high electronic band gap so that photons are not absorbed, or, which has a low absorption coefficient. An example for the first case is the use of indium gallium phosphide (InGaP) instead of silicon (Si) for application at telecommunication wavelengths (i.e. $\lambda_0 \approx 1.55\,\mu m$) [28].

An approach, which enhances every nonlinear optical process, is to use higher intensities. That is the reason why nonlinear optics is usually investigated using a pulsed laser, where a high intensity over a short period of time can be achieved, while keeping the required time-averaged energy limited. Another common way to increase the intensity is to confine the light spatially, for example, by focusing or using waveguiding structures.

The two waveguiding platforms, which will be used in this thesis to enhance nonlinear effects, are photonic crystal and plasmonic waveguides. Plasmonic waveguides are interesting because light can be confined in this structure to arbitrarily small cross-sections [29, 30]. In photonic crystal waveguides light can be significantly slowed down resulting in slow-light enhancement effects [31, 32].

1.4 Subwavelength spatial confinement using plasmonics

1.4.1 Light at a metal-dielectric interface

A metal-dielectric interface supports a surface wave, which is called surface plasmon polariton (SPP). This surface wave is a hybrid wave, which combines an oscillation of the electron density in the metal with an electromagnetic field propagating along the interface of the metal. By solving the Maxwell's equations it can be shown that the SPP is a transverse-magnetic (TM) wave of which the amplitude peaks at the metal surface and decays exponentially away from the interface. A snapshot of the corresponding electric field lines is given in Fig. 1.5. Since the SPP is a TM wave, it possesses one magnetic component H_y transversal to the propagation direction

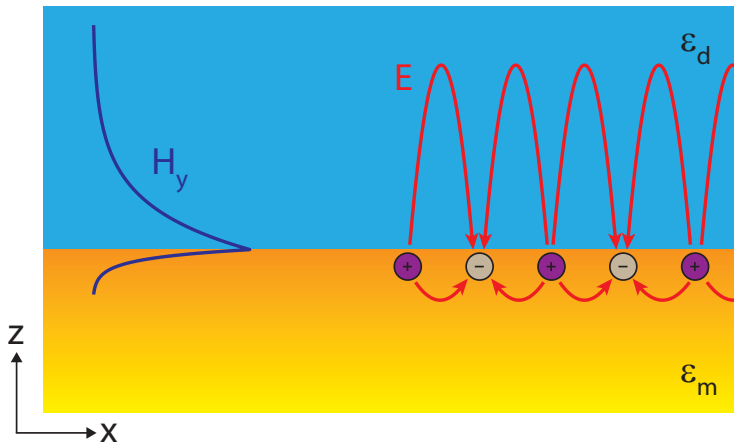

Figure 1.5: Schematic of the electromagnetic field lines of a SPP propagating on a metal-dielectric interface. A SPP is a TM wave, which features one magnetic component H_y *transversal to the propagation direction x. This component* H_y *has maximum amplitude at the interface and decays exponentially in the normal direction. The electric field E is predominantly oscillating in the direction normal to the interface, but also features a component in the direction along the propagation direction. Additionally, in a SPP the electron density inside the metal oscillates.*

(here the x direction). The electric field E oscillates predominantly normal to the interface, but also has a component along the propagation direction. For a flat metal-dielectric interface it can be shown that the SPP dispersion relation is [33]:

$$k_{SPP} = k_0 \sqrt{\frac{\epsilon_d \epsilon_m}{\epsilon_d + \epsilon_m}}, \tag{1.17}$$

where k_{SPP} is the propagation constant of the SPP and ϵ_d and ϵ_m are the dielectric constants of the dielectric and the metal, respectively.

The dispersion relation of the SPP is of course tightly bound to the dispersion of the material dielectric constants. Thus, to understand the behavior of the wavevector of the SPP with varying frequency, it is necessary to discuss the material properties. Relative permittivities of dielectrics can be usually considered as constants, at least far away from absorption

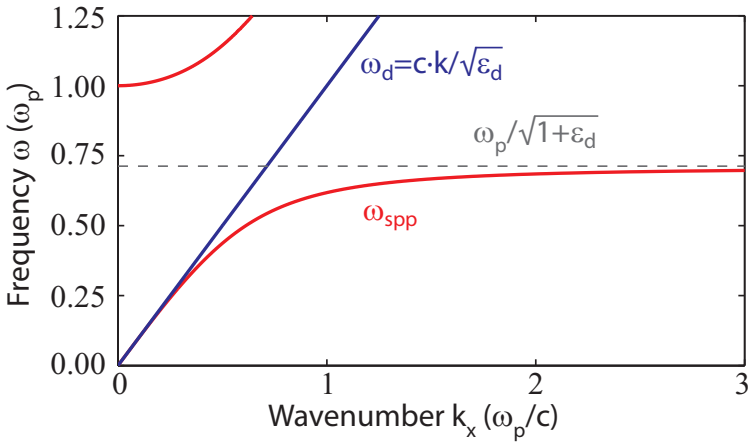

Figure 1.6: Dispersion relation for a SPP propagating along a metal dielectric interface. Here, the dielectric constant of the metal ϵ_m is described by a Drude model without losses. For low frequencies, the dispersion relation of the SPP ω_spp (red line) follows closely the light line ω_d (blue line), i.e., the dispersion relation of the light propagating in the dielectric. By increasing the frequency towards the plasmon frequency (gray dashed line) the wavevector of the SPP diverges. There is also a branch of the dispersion relation above the plasma frequency, which we do not consider here, since it does not describe a wave guided along the metal interface.

peaks, whereas metals are commonly very dispersive. A good model for the dielectric constant ϵ_m of a metal is the Drude model [34]. Inserting the Drude model in Eq. (1.17) allows to plot the dispersion relation and to gain basic understanding of the behavior of SPPs.

Figure 1.6 illustrates the dispersion relation of a SPP for a Drude metal-air interface. For simplicity, damping was taken to be negligible. Two branches of the dispersion relation can be observed, one below and one above the plasma frequency ω_p. We will consider here only the lower branch, which describes a SPP confined to the metal interface. In contrast, the metal becomes transparent for frequencies above ω_p and features therefore no guided surface mode anymore. For low frequencies SPPs exhibit a wavevector that is close to the light line in the dielectric, which is described by $\omega = \mathrm{c} \cdot \mathrm{k}/\sqrt{\epsilon_\mathrm{d}}$. Thus, in this regime, the SPP behaves very similar to

light propagating in the bulk dielectric. However, for frequencies close to the surface plasmon resonance frequency $\omega_{sp} = \omega_p/\sqrt{1+\epsilon_d}$ the wavevector diverges. Further, the wavevector of the SPP always lies below the light line. The resulting momentum mismatch for a given frequency therefore precludes excitation of a SPP with free space light on a smooth metal surface. However, defects, which scatter light, can allow to excite a SPP. Periodic grating structures can also provide the missing the momentum [35]. Alternatively, a prism in combination with frustrated total internal reflection can be used to excite SPPs [36].

In general, metals feature losses and the wavevector of a SPP becomes a complex number, since the dielectric constant of a metal will also contain an imaginary part. As a consequence, the electromagnetic field of a SPP decays exponentially along its propagating direction x. The amplitude decay is related to ohmic losses in the metal, i.e., the electrons dissipating energy into heat. The amplitude decay of a SPP is usually described by the propagation length l_{prop}, which equals the propagation distance after which the intensity has decayed by a factor of e^{-1}. The propagation length is given by the following equation:

$$l_{prop} = \frac{1}{2\mathrm{Im}\{k_{SPP}\}}. \tag{1.18}$$

In essence, SPPs are surface waves, which allow a very good spatial confinement of light due to their large wavevector. The downside of using metal structures as waveguides is the inherent ohmic losses, which cause absorption of light.

1.4.2 Plasmonic waveguides

So far, we have only discussed SPPs which propagate on a single metal-dielectric interface and are therefore only confined in one direction. However, it has been shown that SPPs can also be confined in two dimensions by using a plasmonic waveguide, which is usually based on a patterned metal film. Examples for plasmonic waveguides are metal stripes on dielectric substrates [37], wedges [38] and grooves [39] in metal films, dielectric stripes on metal films [40] or metallic rods and tapers [41] and combinations of all those structures. Some of these geometries are illustrated in Fig. 1.7.

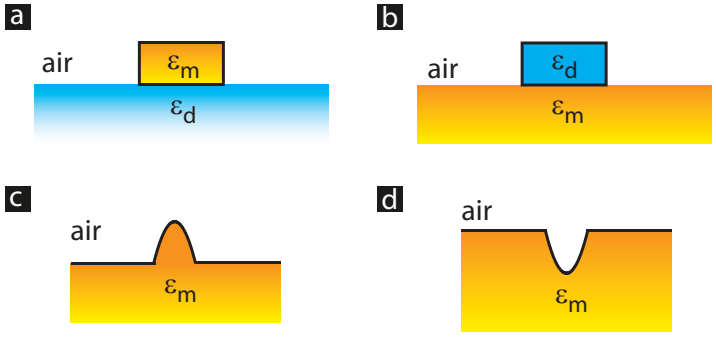

Figure 1.7: Plasmonic waveguide geometries. There are variety of possibilities to confine an SPP in two dimensions, which always involves a metallic and a dielectric material. Shown here as examples are a) a metal stripe located on a dielectric substrate and b) the inverse situation. c) A wedge on a metallic surface or d) a groove in a metallic surface.

For most of the plasmonic waveguides a deep subwavelength confinement can be achieved. Guiding of SPPs in waveguides with cross-sections as small as 50 nm × 60 nm have easily been reached [42]. Consequently, a large field enhancement and a high intensity of the guided mode is possible, which is useful for exploiting nonlinear optical effects more efficiently, as mentioned above. Examples of an enhanced nonlinear response due to confining light with a SPP are enhanced photoluminescence [43, 44] and higher harmonic generation [45] in tapered plasmonic waveguides.

1.5 Slowing light down in photonic crystal waveguides

1.5.1 Light in periodic dielectric structures

Photonic crystals (PhC) are usually man-made dielectric structures where the dielectric constant is periodically modulated [46, 47]. The idea behind a PhC is to control the properties of light by shaping the geometry of the materials instead of relying only on the material properties. For the sake of simplicity we will explain the optical properties of a PhC by considering a one-dimensional periodic stack of alternating layers (see Fig. 1.8a) [48]. This simple structure is very often used as a high reflecting mirror and is

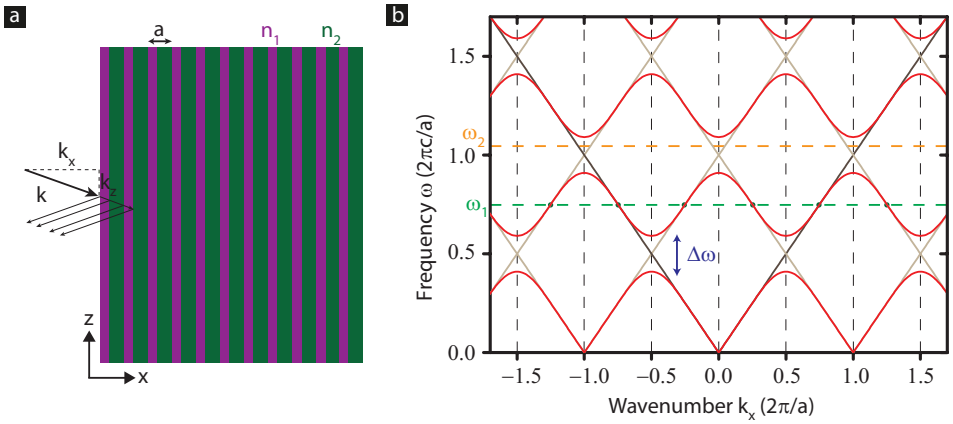

Figure 1.8: Band structure of a one-dimensional photonic crystal. a) A stack of periodic alternating layers with different refractive indices forms a one-dimensional photonic crystal. Light that impinges on the structure will reflect at every interface. If all partial reflections add up constructively, the layer stack will act as a high reflective mirror. b) Due to the periodicity of the layer stack and the contrast in the refractive indices of the layers avoided crossings appear in the bands of the dispersion relation. As a consequence, stop gaps are formed. For any frequency in one of the continua of bands, there are an infinite number of wavevectors. For a frequency in one of the stop gaps no modes exist and light of those frequencies is not allowed to propagate inside the structure. In this case the layer stack acts as a mirror. The dark gray line represents the dispersion relation for a continuous material, whereas the light gray lines illustrate the extra bands created by a hypothetical periodicity.

called a Distributed Bragg Reflector (DBR).

Light propagation in the DBR is best understood by examining its dispersion relation for an electromagnetic wave. In a periodic structure the dispersion relation consists of an infinite number of bands, which are separated by an integer amount of the reciprocal lattice vector. In the case of a vanishing contrast of the dielectric constants of the alternating layers of the DBR, the bands of the dispersion relation $k_x(\omega)$ will be simply given by two straight lines, as depicted by the dark gray lines in Fig. 1.8b. This resembles the propagation of light through a continuous material with constant dielectric constant. The light gray lines illustrate the creation of extra bands in the case of a hypothetical periodicity. Due to a refractive index contrast, avoided crossings between the different bands of the dispersion relation occur [49, 50]. As a consequence, there will be a frequency range where no propagating mode exists, which is called a stop gap. Such a stop gap can be explained by the interference between the multiple light reflections at the interfaces of the multilayer stack. In a certain wavelength range, all reflections will interfere constructively and the DBR will work as a perfect mirror in the direction of the periodicity. The size of the stop gap $\Delta\omega$ is related to the amount of reflection at the interfaces, which depends on the contrast of the dielectric constants. A larger contrast will lead to a larger stop gap.

All considerations made here for a one-dimensional periodic structure can be extended to structures with two- or three-dimensional periodicity.

1.5.2 Controlled slowdown of light

It is possible to guide light using PhCs by creating defects in otherwise periodic structures. It has been shown that a 2D PhC waveguide (PhCW) in a thin membrane can be used to achieve high spatial confinement transversal to a propagation direction [51]. Here, a thin dielectric membrane, usually about 220 nm thick, and consisting of a high refractive index material like Si or InGaP, is periodically perforated by air holes (see Fig. 1.9). The actual waveguide is formed by creating a line defect, i.e., leaving the dielectric unperforated, in an otherwise two-dimensional periodic crystal. The spatial confinement in the line defect is created by a combination of total internal reflection for the z direction and a photonic band gap of the PhC in the (x,y) plane [52]. Consequently, light can theoretically propagate along the created line defect without losses [53].

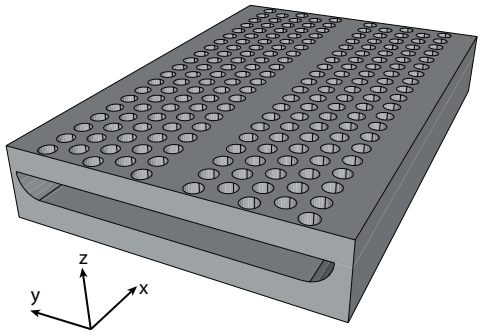

Figure 1.9: Schematic of a photonic crystal waveguide. Here, a thin dielectric membrane is perforated by periodically arranged air holes. A line defect, which acts as the actual waveguide for guiding light along the x direction, is created by leaving the dielectric unperforated. The spatial confinement is achieved by total internal reflection in the z direction, and a photonic band gap in the (x,y) plane.

The achievable high spatial confinement is one reason why PhCWs are interesting for exploiting nonlinear optical effects. PhCWs with a cross-section of 730 nm × 220 nm are readily fabricated nowadays. This means that the confinement is weaker than for plasmonic waveguides but still much better than in optical fibers.

The dispersion relation of the guided mode in the PhCW depends on the width of the line defect and the geometry of the surrounding crystal. A typical dispersion relation for a PhCW is presented in Fig. 1.10. It is common to plot only half of the first Brillouin zone, which due to symmetry contains all necessary information about the dispersion of the modes. Further, the diagram is usually plotted with normalized wavevectors in units of $2\pi/a$ and normalized frequency in units of $2\pi c/a$. We are interested in the frequency region where the surrounding PhC has a 2D photonic band gap. Therefore, we first examine the dispersion relation of a PhC without a line defect (see Fig. 1.10a-b). In this case two continua of bands are formed that lie below and above a photonic band gap. We create a PhCW by inserting a line defect of certain width, here $\sqrt{3}a$, to generate two bands in the dispersion relation, which lie in the band gap (cf. 1.10c-d). These two new bands describe modes that are confined to the line defect. These modes have a different in-plane symmetry, e.g., the even mode has an even

H_z distribution, while for the odd mode this component exhibits an odd symmetry [54]. The band, which stays nearly constant in frequency with varying wavevector, represents the odd symmetric mode, whereas the other band characterizes the even symmetric mode.

In Fig. 1.10 we also show the light line, which represents the dispersion relation of light in free space. If the dispersion relation of the waveguide mode lies above this light line, light in the defect can couple to free space. Thus, we are interested only in the part of the dispersion relation, which lies below the light line.

We confine our discussion here to the even symmetric mode. The band of this mode decreases in frequencies with increasing wavevector (cf. Fig. 1.10d). This negative slope indicates that the mode features a negative group velocity. However, this dispersion relation is the back folded version, i.e., mirrored at $k_x = 0$, of a similar band in the other half of the first Brillouin zone, which exhibits the same but positive v_g. This curve therefore also represents the dispersion properties for a similar mode propagating in the positive x direction, but with inverted sign of the dispersion properties (e.g. GVD and TOD coefficient). In general, this guided mode will slow down with decreasing frequencies. For large frequencies, the group velocity in a typical PhCW tends to a value close to roughly the speed of light divided by the refractive index of the background material. For example, for a PhCW fabricated in a silicon membrane, v_g reaches a value of $c/5$ for large ω. At small frequencies the group velocity converges to zero.

It has been shown that certain linear and nonlinear effects can be effectively enhanced in PhCW by slowing the guided mode down [55]. This enhancement originates from two reasons [56]: (I) a slower pulse has more time to interact with matter, and (II) the pulse is spatially compressed upon entering from a fast light into a slow light waveguide, leading to an increase in its intensity. The second reasoning is based on a simplified view which takes the energy flux conservation across the interface between waveguide sections of different group velocities into account. In essence, the deceleration of the mode leads to an enhancement with the slowdown factor S, which is defined as $S = n_g^{(2)}/n_g^{(1)}$ when the mode experiences a change in the group index from $n_g^{(1)}$ to $n_g^{(2)}$. In the case that the mode enters the waveguide from a bulk material the slowdown factor is defined by $S = n_g/n$, where n_g is the group index in the waveguide and n the refractive index of the material. It has been shown that nonlinear effects, which

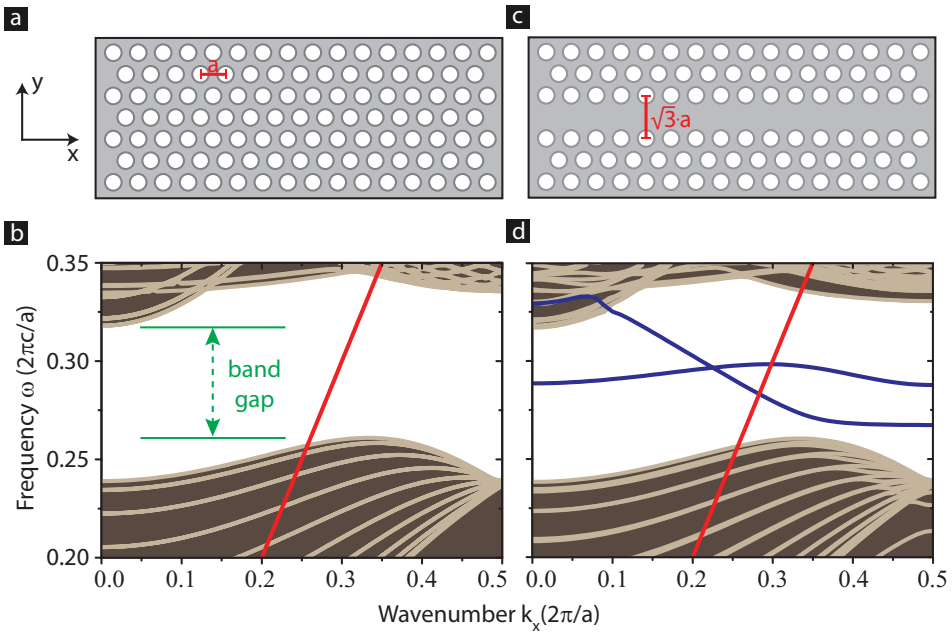

Figure 1.10: Creation of waveguide modes in a line defect in a two-dimensional PhC. a) Topview of a PhC created by perforating a thin dielectric membrane with periodical arrangement of air holes. b) Dispersion relation of the modes that propagate inside the PhC. In detail, two continuum frequency ranges are formed, where many modes are supported. These bands are separated by the photonic band gap, a frequency range where no mode is available. c) Topview of the PhCW generated by leaving one row of air holes out of the otherwise periodic arrangement. d) Dispersion relation of the modes in the PhC, which also contains a line defect. Due to the line defect two bands in the band diagram appear (blue lines), which are situated in the band gap. These two bands represent modes, which propagate and are spatially confined to the line defect. Additionally, the light line is shown in red in b) and d).

Parameter	Name	Slow-light enhancement
α	Linear absorption coefficient	S
α_{2PA}	2PA coefficient	S^2
n_2	Kerr coefficient	S^2
α_{3PA}	3PA coefficient	S^3
σ	FCA cross-section	S
k_c	FCD coefficient	S

Table 1.1: Enhancement of different effects due to the slowdown of light.

scale with intensity, scale also with a power of S [55, 57]. In detail, 2PA and SPM are enhanced by S^2. Further, 3PA scales cubic with S. In contrast, effects that do not depend on the intensity are linearly enhanced by S. Thus, linear absorption, FCA and FCD scale linearly with S. A summary of the slow-light enhancement for the processes considered in this thesis is given in table 1.1.

The fact that a PhCW is highly dispersive can be used for implementing various interesting devices [58]. However, it also means that a pulse propagating inside the waveguide will temporally broaden, which is detrimental for the use of nonlinear optical effects since the peak intensity will consequently decrease. It would therefore be beneficial to achieve a low group velocity or a high group index, respectively, which is constant over a broad frequency range. Interestingly, it is possible to design the dispersion relation of a PhCW by changing the geometry of the crystal, for example by adjusting the position of the air holes adjacent to the line defect [59]. Thus, a slow-light enhancement for nonlinear optical effects is possible in combination with pulses in the pico- and femtosecond regime, while avoiding strong temporal reshaping. It has been experimentally shown that the slow-light enhancement of the intensity together with dispersion engineering can be beneficially used for enhancing third-harmonic generation [60], SPM and free-carrier effects [57] or enabling soliton propagation on much shorter length scales than in optical fibers [61].

1.6 Outline thesis

This thesis describes experiments and calculations of pulse propagation in nanoscale waveguides, where nonlinear optical effects and free carriers play

a significant role. In detail, the different concepts and the waveguiding structures discussed in this chapter will be employed.

Chapter 2 will introduce the experimental setup, a near-field microscope that we use to investigate pulse propagation directly in a waveguide. We discuss and illustrate the different operation modes of this setup. We show how it is possible to track the temporal pulse envelope in-situ. Further, we demonstrate that the spectral density of propagating pulses can be measured.

In chapter 3 we show experimentally how by means of point-to-point measurements we can extract the nonlinear optical characteristic of single devices in an integrated photonic chip. In detail, we demonstrate that local measurements of the spectral density allow us to understand and model the propagation of a pulse in a single component without the need to take the other components into account.

Chapter 4 presents the first direct observation of a soliton fission event. We illustrate how a higher-order soliton splits into several wave packets by propagating through a PhCW. We report a record short fission length of 166 µm and show for the first time that free carriers can perturb the propagation of a higher-order soliton.

In Chapter 5 we investigate the potential of gold nanowires for guiding ultrashort pulses. We compare the properties of this plasmonic waveguide to the properties of a silicon nanowire. Especially, we show that the metal structure features superior dispersion properties. Further, we demonstrate that the dielectric waveguide suffers from a cut-off of the fundamental mode if high spatial confinement is required. We show that if only the decay of the peak intensity is of interest the gold nanowire can outperform their silicon analogon in the ultrafast regime.

Chapter 6 contains future research directions and possible applications of the results presented in this thesis. We propose to enhance the capabilities of the near-field microscope to characterize ultrashort pulses by changing the detection scheme. Further, we suggest the implementation of an on-chip white-light source by using supercontinuum generation in a nanophotonic waveguide. Finally, we discuss the possibilities to create an optical generator based on nonlinear pulse propagation in a gold nanowire.

2

Near-field microscopy

ABSTRACT: In this chapter we describe the concept of phase- and time-resolved near-field microscopy that is used throughout the thesis for various experiments. We explain all features required of this technique to characterize ultrashort pulse propagation in waveguides. First, we illustrate how a collection aperture near-field microscope can be used to investigate the properties, including the phase, of light propagating in a waveguiding structure. Further, we explain the spectroscopic mode of our setup, which allows local investigation of the spectral density. Time resolution is achieved by using an optical delay line and a pulsed laser source. To illustrate the features of the near-field microscope we present various measurements on a PhCW.

2.1 Introduction

Near-field microscopy [62, 63] allows the investigation of electromagnetic fields with a resolution beyond the diffraction limit. The general principle of this measurement technique is that a scanning nano-probe is employed to act as a point source of light or to locally collect the electromagnetic field. There are two inherent benefits of a near-field microscope. First, its optical resolution is not limited by diffraction, but given by properties of the near-field probe [64, 65, 66]. This feature is increasingly important since more optical structures are scaled down to the nanoscale. Second, by using a near-field microscope it is straightforward to investigate guided modes [67, 68, 69, 70, 71]. Nowadays, in analogy to electronics, more and more complex photonic circuits are implemented by integrating an increasing number of optical devices on chip. As a consequence, the ability to measure the separate components of integrated photonic circuits in a nondestructive fashion is important.

To investigate ultrashort pulse propagation, featuring a pulse width of a few tens to a few hundreds of femtoseconds, a near-field microscope with ultrafast time resolution is required. Optical measurement techniques, where ultrashort pulses can be measured, have in common that their time resolution is achieved by cross-correlating two ultrashort optical pulses. Time-resolved near-field microscopes have been implemented with an interferometric correlation approach. It has been shown that integrating a near-field probe and an optical delay line in an interferometer allows to track ultrashort pulse propagation in waveguides [72, 73].

Spectral information can be also obtained in a near-field microscope. Spectrally analyzing the light picked up by a near-field probe provides the possibility to locally investigate the spectral density of the guided light. Especially important for this thesis is that it is possible to track the evolution of the spectral density of a propagating pulse [74]. Nonlinear optical effects often change the spectral content of a pulse during propagation, e.g., self-phase modulation broadens the spectrum. Commonly, there is also not just one nonlinear effect occurring, rather several occur simultaneously. As a consequence, to understand the spectral evolution of a pulse experiencing various nonlinear optical effects during propagation is a nontrivial problem and usually requires a huge modeling effort. Thus, applying spectrally resolved near-field microscopy can provide additional information which helps to understand the various complex processes during nonlinear pulse

propagation.

In this chapter, we explain how a phase-resolved near-field microscope with a femtosecond time resolution is implemented. We start with the most basic configuration of a near-field microscope, which measures the intensity distribution of guided modes in section 2.2. In section 2.3, an alternative measurement approach is introduced, where the spectral density of the guided mode is measured. Next, in section 2.4 we show how phase resolution is achievable by integrating the near-field microscope into an interferometric setup. The chapter is concluded in section 2.5, which contains an explanation of the time resolution of our near-field microscope.

2.2 Intensity near-field microscopy

Near-field microscopes can be generally used in two different operation modes: the collection and the illumination mode. In the collection mode, light is locally picked up by a near-field probe. In contrast, in the illumination the near-field probe acts as a local electromagnetic point source. Naturally, both modes have different application areas. The collection mode is useful in the investigation of spatially confined light, e.g., imaging the spatial distribution of an electromagnetic field profile. The illumination mode is beneficial where local excitation is required, e.g., exciting single molecules.

Another differentiation can be made by the specific near-field probe used in the microscope. There are aperture and apertureless near-field microscopes. Here, we limit ourselves to microscopes where a tapered optical fiber is used as near-field probe in the collection mode. The optical aperture nano-probe frustrates evanescently decaying waves and converts a small fraction into propagating modes in a single-mode detection fiber which can be detected in the far-field. An aperture probe is usually covered with an optically thick metal layer with a sub-wavelength well defined opening at the tip where light can enter the probe, the aperture [75]. As a consequence, the near-field probe detects the electromagnetic field only at the location of the aperture. The typical aperture size applied in our experiment ranges from 200 to 300 nm. In contrast, in the case of an apertureless probe the metal layer is missing. To limit the scope of the discussion, we will not further consider apertureless near-field microscopy, where, for example, a nanoscopic scatterer is used as probe. Detailed information about

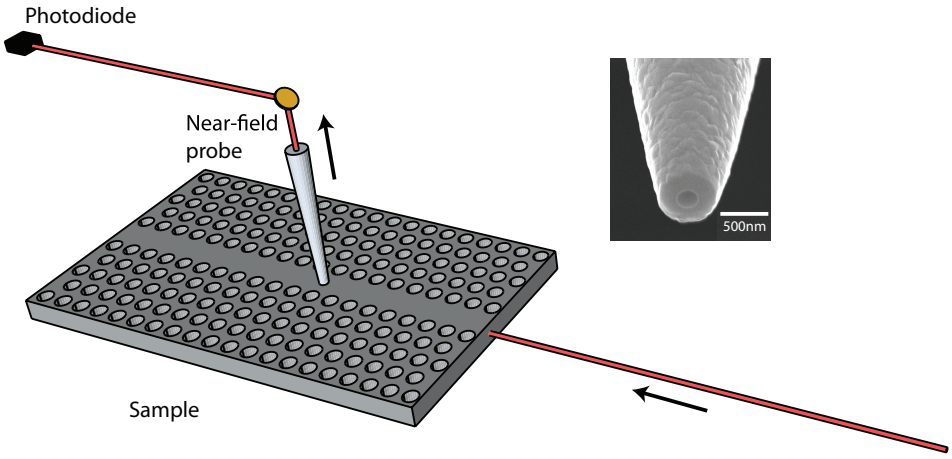

Figure 2.1: Schematic of an aperture near-field microscope in collection mode measuring intensity of a mode guided in the sample under investigation. The setup consists of a near-field probe, a photodiode, the sample and far-field optics to excite the guided mode in the sample. In this figure a photonic crystal waveguide was chosen as example for the sample under investigation. The inset shows a SEM micrograph of the tip of a typical aperture near-field probe. Visible in the aluminum coating is the aperture with a diameter of 200 nm.

this technique can be found in literature [76].

In this thesis, we will solely investigate light as it propagates through waveguiding structures. For this purpose, an aperture near-field microscope in collection mode is highly suitable [77]. In the experiments, light is coupled into the sample under investigation by far-field optics and the guided mode is investigated by a near-field probe. The tip is kept close (i.e. 20 nm above) to the sample by means of a shear-force feedback mechanism [78, 79]. The probe follows the topography of the sample by keeping the resonance properties of an attached tuning fork constant by means of an electronic feedback loop. As a consequence, we can measure the topography of the sample at the same time as the optical signal [80].

In the simplest measurement mode of a near-field microscope the light that is detected by the probe is directly measured by a photodiode as shown in Fig. 2.1. We first consider a continuous wave (CW) light field which creates the following signal on the photodiode:

$$V_{Det}(x, y) = C_{Det} C_{Tip}^2 |E_s(x, y)|^2, \quad (2.1)$$

where C_{Det} describes the sensitivity of the photodiode and C_{Tip} stands for the detection sensitivity of the aperture near-field probe for the electric field. Further, the microscope detects the intensity, which is related to squared amplitude of the electric field components $E_s(x, y)$ in the plane of the sample, at the coordinate (x,y). By scanning the near-field probe over the sample a spatial map of the intensity distribution of the guided light is created. Recently, it has been shown that an aperture near-field microscope is not only sensitive to the in-plane electric fields but also the magnetic ones [81]. However, for the sake of simplicity we will in the remainder of this thesis only focus on the electric contribution. This simplification does not invalidate any of the results presented further on.

2.2.1 Intensity map

Figure 2.2 presents a typical measurement of a spatial modal pattern in a model system, a PhCW. Here, CW laser light of a wavelength of 1.55 µm is coupled into the sample and the near-field probe is raster-scanned over the surface. The waveguide is running along the x-direction and is centered around y = 3 µm.

The left panel of the figure shows the topography gained by the shear-force mechanism by scanning the near-field probe over an area of 6 × 6 µm^2. The periodically arranged air holes are clearly visible as is the waveguide in the center of the scanned region. The right panel shows the voltage V_{Det} measured simultaneously on the photodiode which is proportional to the squared amplitude of the in-plane electric fields of the guided mode. The detected light is clearly confined to the missing row of holes. Moreover, the periodic pattern of the Bloch mode supported by the photonic crystal waveguide is clearly visible in the measurement. The periodicity of the measured intensity approximately equals the lattice constant of 420 nm. In conclusion, this example shows that near-field microscopy allows us to map the complex intensity of the mode guided in a PhCW on a subwavelength scale.

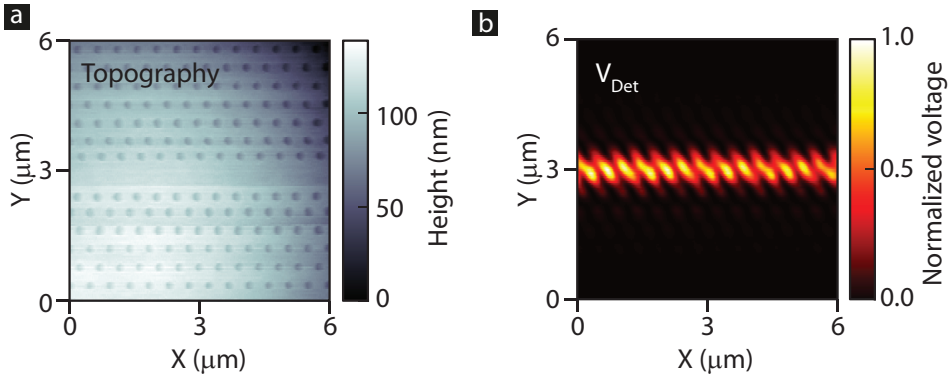

Figure 2.2: Spatial intensity near-field microscope measurement on a PhCW with CW excitation of the guided mode at a wavelength of 1.55 µm. *In the measurement the near-field probe was scanned over a* $6 \times 6\,\mu m^2$ *large area. The actual waveguide is created by the row of left out holes at* $y = 3\,\mu m$ *running along the x-direction. a) The measured topography revealing the periodic arranged air holes and the missing row of holes. b) Normalized photodiode voltage which is proportional to the intensity of the guided mode showing the periodic modulation expected for a Bloch mode.*

2.3 Spectrally resolved detection of guided light

Collection near-field microscopy can be used to perform near-field spectroscopy. Combining the superior resolution of a near-field probe with a spectroscopic measurement approach allows the spectral investigation of light on the nanoscale, enabling a variety of new applications. For example, spectrally resolved near-field microscopy was used to gain local information about photoluminescence from quantum wires [82] or quantum wells [83]. Moreover, using an apertureless scattering near-field microscope it was shown that Fourier-transform infrared (FTIR) spectroscopy can be performed to, e.g., measure locally the free-carrier concentration in doped silicon [84]. Further, it was demonstrated that spectrally resolved near-field microscopy allows the extraction of the group velocity of a guided mode [85] or the visualization of supercontinuum generation in a nonlinear waveguide [74]. Thus, new information about pulse propagation can be gained which cannot be extracted from simple transmission measurements.

To perform near-field spectroscopy on pulses propagating in waveguides,

the light that is collected by the probe is spectrally analyzed by, for example, a grating spectrometer. Nearly the same setup can be used as for the intensity near-field microscope (see Fig. 2.1), only a detector with spectral resolution is required instead of a simple photodiode. As a consequence, the near-field microscope measures the power spectral density of the intensity at the local position of the probe, a quantity that contains information about the spectral distribution of the optical power of the guided light. Mathematically, we can define the quantity that is picked up by the near-field probe as the spectral density of the detected in-plane electric field $E_s(x, y)$ at coordinate (x_0, y_0):

$$P(\omega)_{x_0,y_0} = C_{Spec}\,\mathscr{F}\{\int E_{x_0,y_0}(t)E^*_{x_0,y_0}(t-\tau)d\tau\}, \tag{2.2}$$

where $\mathscr{F}$ denotes a temporal Fourier transform and C_{Spec} is the sensitivity of the spectrometer.

By performing near-field spectroscopy at different locations the spectral evolution with propagation can be extracted. It is even possible to determine the spectral transfer function of a component of a more complex integrated photonic circuit. For this purpose, spectrally resolved near-field microscopy has to be performed before and after the device so that the changes in the spectral density caused by only this device are measured.

The idea of near-field spectroscopy is to locally measure the spectral density of light with maximal spectral bandwidth and the best possible spatial and spectral resolution. To achieve the best spatial resolution in the case of aperture near-field microscopy the aperture size has to be minimized. This approach has one downside since it decreases the detected signal level. Consequently, the achievable signal-to-noise ratio, which determines the minimum amount of light that can be detected, is of crucial importance. The signal-to-noise ratio of near-field spectroscopy will decrease in comparison to intensity near-field microscopy, since the detected light is spectrally split leading to a decreased signal at each detector, while the electronic noise will not be reduced. The lowest measured signal levels, where a decent signal-to-noise was reached, were in the tens pW/nm regime. Potentially, smaller signals can be detected by switching to nitrogen-cooled grating spectrometers, which feature a higher sensitivity and a lower noise level.

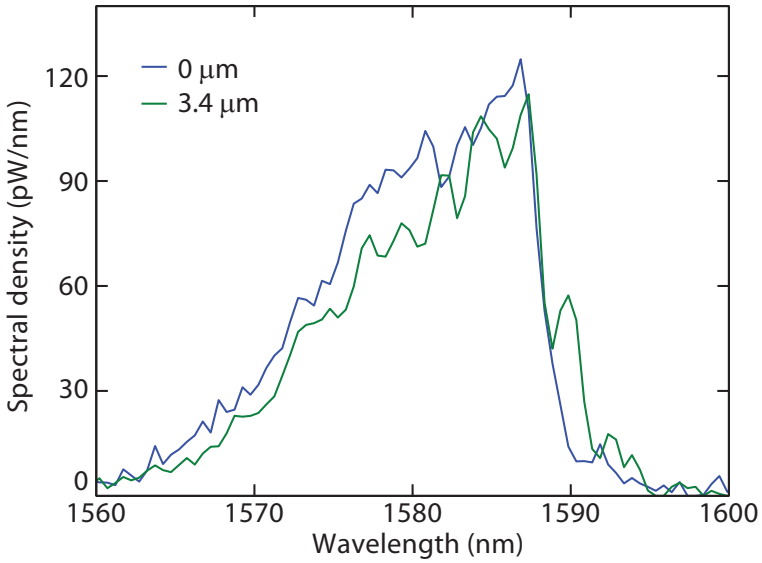

Figure 2.3: Near-field measurements of the spectral density of a 120 fs short pulse propagating inside a PhCW. There are measurements at 2 different propagation distances, tracking the way the spectrum changes as the pulse propagates.

The spectral resolution is simply determined by the detector used. In the case of a CCD grating spectrometer, a spectral resolution of well below 0.1 nm can be reached. In contrast, the spectral regime, which is covered by near-field spectroscopy, is not only based on the detector used, but the near-field probe sets limitations on the wavelength range that can be measured. Bethe-Bouwkamp theory predicts that the transmission of an aperture in a metal film scales as $1/\lambda^4$. Consequently, the near-field probe collects light of shorter wavelength more easily. Finally, the optical properties of the single mode fiber that we use to guide the light will also influence the spectral sensitivity.

Figure 2.3 shows two typical measurements where the spectral density of a propagating pulse is measured at different locations in a photonic crystal waveguide. As light source used is a 120 fs pulsed laser system which features a Gaussian-shaped spectrum centered around 1588 nm with a FWHM of 24 nm. The measured spectra indeed have maximum amplitude around a wavelength of 1588 nm. However, the spectral densities are not Gaussian

shaped, but asymmetric. This is attributed to the cut-off at 1590 nm of the mode in the PhCW. The fact that both spectra measured at different locations inside the PhCW are very similar shows the reproducibility of this measurement approach. We do not expect any spectral changes since the pulse features a low intensity and so nonlinear effects should not occur. This example demonstrates that near-field spectroscopy is sensitive enough to characterize the spectral density of a pulse propagating in a waveguide.

2.4 Phase-resolved detection

Measuring the phase of light is commonly achieved by an interferometric approach [86, 87], which means that the interference of two beams is measured to extract the phase difference between them. Our setup is based on a Mach-Zehnder interferometer [88, 89]. We use a laser as input light source and its beam is split into branches by a beam splitter. The two generated branches we call 'sample' and 'reference' branch. The sample branch contains the sample under investigation and the near-field probe plus fiber which collects light from a known location on the sample. The reference branch is just a free-space optical path. Both branches are recombined in a fiber y-splitter and the interference signal is measured by a photodiode. The detected signal can be described as follows:

$$\begin{aligned} V_{Det}(x,y) &= C_{Det}\left(|C_{Tip}E_s(x,y) + E_r|^2\right) \\ &= C_{Det}\left(C_{Tip}^2|E_s(x,y)|^2 + |E_r|^2\right. \\ &\qquad \left. + C_{Tip}|E_s(x,y)||E_r|\cos(\Delta\phi(x,y))\right), \end{aligned} \tag{2.3}$$

where E_r is the electric field of the light propagating in the reference branch and $\Delta\phi(x,y)$ is the phase difference between the two branches of the interferometer.

In general, the interferometric approach also allows us to perform polarization-resolved measurement [90]. However, for simplicity, we neglect any effect of the light polarization in the following description.

To extract the phase evolution of the light propagating inside the sample, it is easiest to use a balanced interferometer. In this special case, the interferometer branches are built in such a way that both optical paths have exactly the same length, without the sample being present. Thus, the

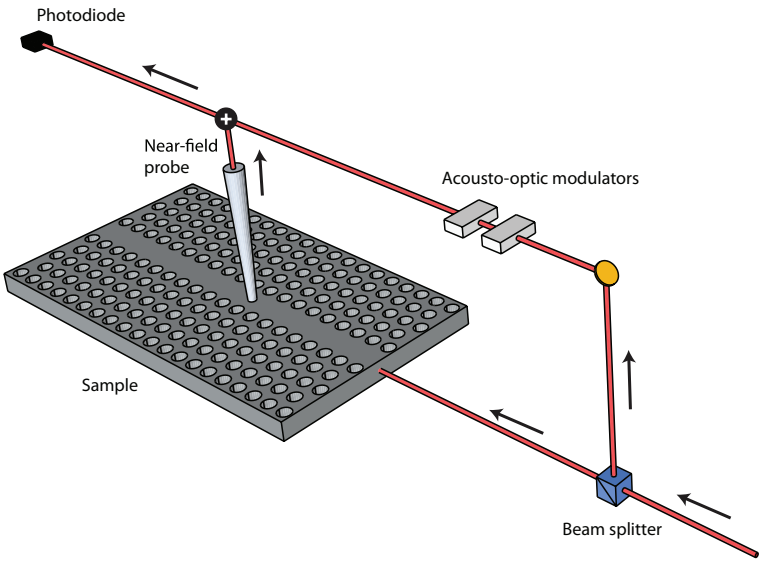

Figure 2.4: Schematic of the phase-resolved near-field microscope where the near-field probe and the sample are inserted in one of the branches of a Mach-Zehnder interferometer. The light in the other interferometer branch gets frequency-shifted by two AOMs to enable heterodyne detection.

interference term in Eq. (2.3), consisting out of the product of the electric fields in the two branches and the phase difference, is zero. By including the sample into the interferometer a path length difference is created which results in a $\Delta\phi(x, y)$ and an interference term that directly represents the phase retardation inside the sample.

The near-field probe picks up only a minute amount of light, usually in the mV/m regime, so that $E_s(x, y)$ is much smaller than E_r. As a result, the signal detected by the photodiode (Eq. (2.3)) is dominated by the term caused by the intensity of the light in the reference branch. The interference term, which contains the phase information, is hidden as a small modulation on top of this huge background.

One approach, which can be used to detect the interference term in Eq. (2.3), is called heterodyne detection. In this concept the frequency of the light in one of the interferometer branches is shifted, so that the interference term, containing the phase information, beats in time and can therefore be filtered out, e.g., with a lock-in-amplifier (LIA) [91, 92].

In our setup, which is schematically depicted in Fig. 2.4, the frequency shift of the light is accomplished by including two traveling wave acousto-optical modulators (AOMs) in the reference branch. In an AOM an acoustic wave is created which acts as a diffraction grating for light [93]. The diffracted light will be shifted in frequency due to the Doppler effect. To achieve a frequency shift of 40 kHz, which is easily detected by means of electronics, two AOMs are arranged after each other in the reference branch. First the +1 diffracted order is used, then the -1 order, where the AOMs are driven with two different frequencies in the megahertz that differ by the desired frequency shift. In detail, the first AOM will be operated at a frequency of 80.04 MHz, whereas the second one is working at a frequency of 80 MHz. As a consequence of this frequency-shift, the voltage delivered by the photodiode will be modulated in time:

$$\begin{aligned} V_{Det}(x,y) \;=\; C_{Det}\,(C_{Tip}^2|E_s(x,y)|^2 + |E_r|^2 \\ +C_{Tip}|E_s(x,y)||E_r|\cos(\Delta\omega\, t + \Delta\phi(x,y))), \end{aligned} \tag{2.4}$$

where $\Delta\omega$ is the frequency shift caused by the AOMs.

A very convenient and efficient way to filter the time-modulated part out of this signal is the use of a LIA. This acts basically as a very narrow bandpass filter around a given frequency (with a bandwidth of a few Hz to a few hundreds Hz) [94, 95], in our case the frequency shift of the AOMs. Lock-in detection is beneficial since it is possible to detect harmonic time-varying signals of small amplitude in a very noisy background. This can be achieved since noise at frequencies outside the filter bandwidth gets suppressed. In particular, the influence of the 1/f noise can be significantly reduced by filtering out the spectral components around 0 Hz.

To detect the temporally varying part of Eq. (2.4) the lock-in amplifier multiplies the voltage on the photodiode with two harmonic signals (a cosine and a sine signal) of desired frequency and phase and integrates the product for a given time T. This results in the quadrature components X and Y [49]:

$$\begin{aligned} X(x,y) &= C_s \frac{1}{T} \int_0^T |E_s(x,y)||E_r| \cos(\Delta\omega\, t + \Delta\phi(x,y)) \cos(\Delta\omega\, t + \theta) dt \\ &= C_s\, |E_s(x,y)||E_r| \frac{1}{2T} \int_0^T \cos(\theta - \Delta\phi(x,y)) \\ &\qquad + \cos(2\Delta\omega\, t + \Delta\phi(x,y) + \theta) dt \end{aligned} \tag{2.5}$$

and

$$\begin{aligned} Y(x,y) &= C_s \frac{1}{T} \int_0^T |E_s(x,y)||E_r| \cos(\Delta\omega\, t + \Delta\phi(x,y)) \sin(\Delta\omega\, t + \theta) dt \\ &= C_s\, |E_s(x,y)||E_r| \frac{1}{2T} \int_0^T \sin(\theta - \Delta\phi(x,y)) \\ &\qquad + \sin(2\Delta\omega\, t + \Delta\phi(x,y) + \theta) dt, \end{aligned} \tag{2.6}$$

where θ is the phase of the LIA and the proportional constant C_s contains besides the amplification of the LIA C_{LIA} also the prior proportional coefficients, i.e., $C_s = C_{LIA} C_{Tip} C_{Det}$.

Equations 2.5 and 2.6 can be further simplified in the case that the LIA integration time T is much longer than the time period related to frequency shift (i.e. $T >> \frac{2\pi}{\Delta\omega}$):

$$X(x,y) = \frac{C_s}{2} |E_s(x,y)||E_r| \cos(\theta - \Delta\phi(x,y)) \tag{2.7}$$

and

$$Y(x,y) = \frac{C_s}{2} |E_s(x,y)||E_r| \sin(\theta - \Delta\phi(x,y)). \tag{2.8}$$

This condition is always fulfilled in our experiments, since the time related to a frequency shift of 40 kHz is 25 µs and therefore much shorter than the LIA integration time of 3 ms that we typically use.

The quadrature components X and Y can be merged in one complex quantity S:

$$S(x,y) = X(x,y) + \imath Y(x,y) = \frac{C_s}{2} |E_s(x,y)||E_r| \, e^{-\imath \Delta\phi(x,y)} \tag{2.9}$$

where for the sake of simplicity the phase θ of the LIA was set to zero. A quantity is generated of which the amplitude is proportional to the electric field amplitude inside the sample. In addition, the phase of S represents the phase retardation caused by the sample. Further, the desired signal picked up by the probe is amplified by the factor $E_r/E_s(x,y)$ which can be seen by comparing Eq. (2.3) and Eq. (2.9). This amplification is called the heterodyning gain and can be several orders of magnitude big [77], since the optical power levels in the signal and reference branch are usually on the order of pW-nW and μW, respectively.

2.4.1 Phase-resolved maps

Figure 2.5 presents a phase-resolved near-field microscope measurement on the same PhCW shown in Fig. 2.2. As before, we see a periodic field pattern which is confined to the missing row of holes and decays transversally in the y-direction. However, since this time we detect a signal proportional to the electric field, the detected signal oscillates around zero, where the oscillations represent the phase evolution. Due to phase sensitivity, the measured pattern shows the phase evolution of the Bloch mode which is determined by its wavevector. Thus, the measured electric field shows a periodicity which does not equal the lattice constant of the PhCW. Instead an interference pattern, which features a period of $\sim 1.5\,\mu$m, is visible. The right panel depicts only the phase $\phi(x,y)$ of the guided Bloch mode.

2.5 Time-resolved detection

Due to the interferometric approach the setup also allows time-resolved measurements to track, for example, a pulse propagating through a waveguide. To achieve time resolution, we use a light source with a finite coherence time τ_{coh} and include an optical delay line in one of the interferometer branches. A finite coherence time indicates that there is a time delay after which the light coming from the light source will not produce interference anymore with light from the same source [96]. For the sake of simplicity,

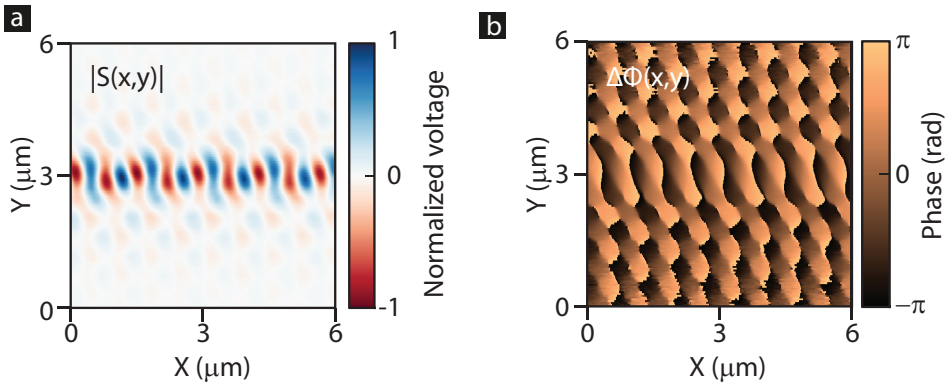

Figure 2.5: Phase-resolved near-field microscope measurements on a PhCW under the same conditions as in Fig. 2.2. a) Real part X(x,y) of the complex electric field. Clearly visible beside the light concentration in the waveguide created by the row of left out holes is the spatial oscillation representing the wavevector of the Bloch mode. b) Phase of the complex electric field exhibiting the same periodicity.

in the remaining part of this thesis we will always talk about a pulsed laser as an example for a light source with finite coherence time.

The optical delay line, which can extend the optical path length of one of the interferometer arms, is used to set up a desired time delay between pulses traveling in the different interferometer branches. Now there are two ways to change the path length difference and therefore also the phase difference in the interferometer: either moving the probe or the delay line. Thus, in the case of our near-field microscopy setup shown in Fig. 2.6 there are two different operation modes to visualize a pulse propagating inside a waveguiding structure in time and space [97]:

- The optical delay line is scanned while keeping the near-field probe at a fixed position during that time. As a consequence, we gain local information about the temporal envelope of the pulse. By repeating this procedure at different probe positions we can track changes of the temporal envelope as the pulse advances in space.

- The probe is scanned over the sample at a fixed delay line position. This creates a map of the two-dimensional electric field distribution

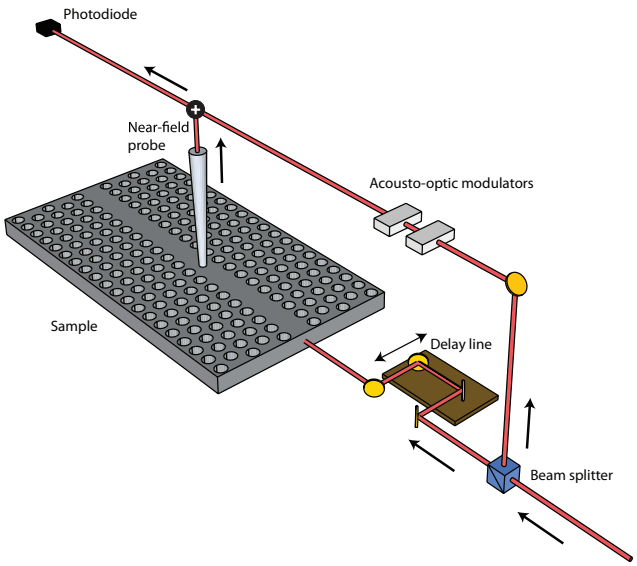

Figure 2.6: Schematic of a time-resolved near-field microscope where additionally an optical delay is inserted in one of the interferometer branches. To enable time resolution also a light source with finite coherence time is required.

of the propagating pulse at a fixed time. By repeating this procedure for different delay line positions, we can track the spatial evolution of the modal field pattern in time.

The next two subsections will explain the differences of these two operation modes in more detail.

2.5.1 Measuring local temporal cross-correlations

In this mode the delay line is scanned while the probe stays at a defined location. As a consequence, the electric field of the pulse gets delayed in one of the interferometer branches in relation to the pulse in the other branch (assuming negligible dispersion in air).

Inserting time-varying electric fields, which are also dependent on a delay time, into the Eq. (2.5) and Eq. (2.6) leads to the following quadrature components that are measured on the LIA [49, 98]:

$$\begin{aligned} X(\tau) &= C_s \frac{1}{T} \int_0^T |E_s(t+\tau)||E_r(t)|\cos(\Delta\omega\, t)\cos(\Delta\omega\, t + \Delta\phi(\tau))dt \\ &= C_s \cos(-\Delta\phi(\tau)) \frac{1}{2T} \int_0^T |E_s(t+\tau)||E_r(t)|dt \end{aligned} \tag{2.10}$$

and

$$\begin{aligned} Y(\tau) &= C_s \frac{1}{T} \int_0^T |E_s(t+\tau)||E_r(t)|\sin(\Delta\omega\, t)\cos(\Delta\omega\, t + \Delta\phi(\tau))dt \\ &= C_s \sin(-\Delta\phi(\tau)) \frac{1}{2T} \int_0^T |E_s(t+\tau)||E_r(t)|dt, \end{aligned} \tag{2.11}$$

where the phase θ of the LIA has been set to zero again and τ is the time delay generated by the optical delay line.

These two quadrature components can, of course, again be merged into one complex quantity:

$$S(\tau) = X(\tau) + \imath Y(\tau) = C_s\, e^{-\imath\Delta\phi(\tau)} \frac{1}{2T} \int_0^T |E_s(t+\tau)||E_r(t)|\, dt \tag{2.12}$$

As a result, we measure an interference signal that depends of the delay time τ. In detail, the quantity $S(\tau)$ is a cross-correlation of the electric fields of the pulses propagating in both branches of the interferometer.

The spectral density of a cross-correlation in the time domain equals a multiplication of the spectra of the temporal functions, which are cross-correlated, in the frequency domain:

$$S(\tau) = \frac{C_s}{2}\, e^{\imath\omega_0\cdot\tau}\, \mathscr{F}^{-1}\{E_s(\omega)\cdot E_r(\omega) e^{\imath(\gamma_s(\omega)-\gamma_r(\omega))}\}, \tag{2.13}$$

where $\mathscr{F}^{-1}$ denotes an inverse Fourier transform. Further, ω_0 is the angular carrier frequency, $E_s(\omega)$ and $E_r(\omega)$ are the amplitudes and $\gamma_s(\omega)$ and $\gamma_r(\omega)$ the phases of the frequency spectra of the pulses in the signal and reference branch, respectively.

Equation 2.13 shows that the signal measured on the LIA is related to the multiplication of the spectra of both pulses in the frequency domain.

Consequently, the interference signal is sensitive to changes in the spectral densities of the pulses. For example, if the spectrum of one of the pulses changes in comparison to the other one, the cross-correlation will be influenced since the spectral overlap changes. However, the measured interference signal is not sensitive to changes in the spectral density, which occur outside of the bandwidth of the spectra of both pulses. Due to the fact that the pulse in the reference branch propagates just through air, we do not expect any changes in its spectral density during propagation. Consequently, the bandwidth of the reference pulse defines the spectral regime, where the interference signal is sensitive to variations in the spectrum of the pulse in the sample. For example, second harmonic generation cannot be visualized by this interferometric approach as long as it happens only in the sample and the change in the spectral density occurs outside of the bandwidth of the pulse in the reference branch.

Since the cross-correlation depends on the spectral phase of both pulses it can be used to extract information about dispersion. In a balanced interferometer, the only term that remains from the phase difference $\gamma_s(\omega) - \gamma_r(\omega)$ in Eq. (2.13) is caused by the dispersion of the sample under investigation. Therefore, the spectral phase of the measured interference signal, which can be extracted by Fourier transforming the time signal, is directly related to the dispersion relation $\mathrm{k}(\omega)$ of the sample.

If a pulse travels through a dispersive medium the pulse envelope will generally reshape and the spectrum will acquire a phase which is related to the dispersion relation $\mathrm{k}(\omega)$ of the material. This can be mathematically stated as

$$\gamma_\mathrm{s}(\omega) \;=\; \mathrm{k}(\omega) \cdot \mathrm{z}, \tag{2.14}$$

where z is the propagation distance. In case of a structure, for example a waveguide, $\mathrm{k}(\omega)$ represents the dispersion relation of the guided mode.

Since, the cross-correlation depends on the spectral shape as shown in Eq. (2.13) all the different coefficients of the dispersion relation (see section 1.2.2) will influence the interference signal. As a consequence, this operational mode of our near-field microscope is suited to investigate the impact of dispersion on pulse propagation. Further, if the pulse in the reference is known in amplitude and phase, by for example a separate measurement using frequency-resolved optical gating (FROG) [99], the pulse in the sample

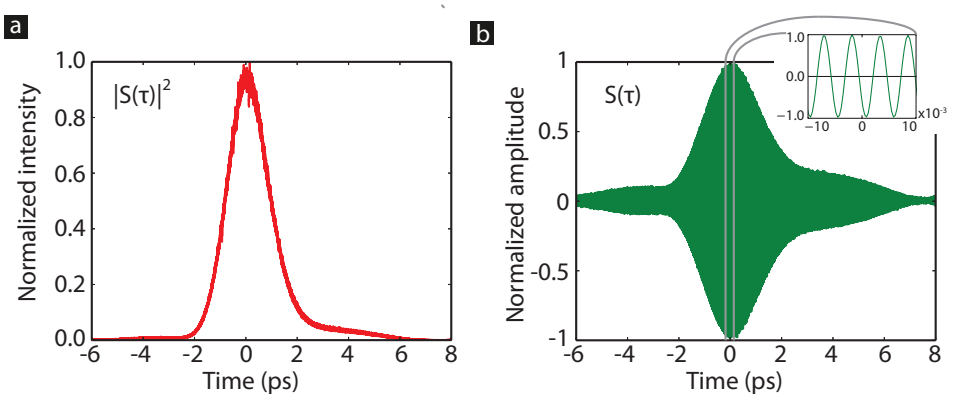

Figure 2.7: Exemplary time-resolved near-field microscope measurement where the delay line is scanned and the probe is kept at a fixed position. a) Intensity and b) real part of the complex electric field of a 2 ps pulse propagating in a PhCW. The inset in b) shows a zoom to illustrate that we resolve the interference fringes

can be uniquely reconstructed from the cross-correlation. In conclusion, scanning the optical delay delivers local temporal information about the pulse at the fixed position of the near-field probe.

From now on we will, for the sake of simplicity, assume that the measured quantity $S(\tau)$ is synonymous with the phase-resolved electric field related to the pulse propagating in the investigated waveguide. This is, as the derivation above shows, only a simplification. The comparison would be strictly true only if the reference pulse was an infinitely short pulse, i.e., a Dirac delta function, so that the cross-correlation would directly deliver the electric field of the pulse in the signal branch.

A typical example of such a delay-line scan measurement is shown in Fig. 2.7. Here, the near-field probe was parked on a PhCW and light from a pulsed laser with a pulsed length of 2 ps was coupled into the sample. The left panel presents the measured intensity as a function of the delay time between both interferometer branches. We define the point in time when the pulses exactly overlap and therefore the cross-correlation is maximum as zero point for the time axis. The intensity measured over time represents a roughly Gaussian shaped pulse centered around t=0 ps. This is expected as the cross-correlation of two Gaussian pulses delivers also a Gaussian shaped

wave packet. The pulse has been subject to dispersion in the waveguide and as a consequence the FWHM width of the cross-correlation function is larger than the 2 ps of the Fourier-transform limited pulse emitted by the laser. The right panel presents the quadrature component $X(\tau)$ extracted by the LIA which equals the electric field amplitude multiplied by the cosine of the phase difference. In detail, a curve can be seen which consists of an envelope modulated by closely spaced fringes. Since the envelope resembles the electric field amplitude, which is the square root of the intensity curve, the wave packet shows a broader temporal width. The inset is a zoom in in the graph around t=0 ps, which illustrates the fringes created by the multiplication of the envelope with the cosine of the phase. Between two maxima there is a phase difference of 2π which equals the time period related to the carrier frequency of the pulse.

2.5.2 Measuring a snapshot of the spatial mode profile in time

In this operation mode, which is described in detail in the literature [100], the delay line is kept at a constant location and the probe is scanned over the sample. As a result, we measure a snapshot of the spatial field distribution of the in-plane electric field at one point in time. Since we change the path length of the signal branch of the interferometer by moving the probe, we only obtain an interference pattern at positions on the sample where the path difference lies within the coherence length l_{coh} of the laser, which is proportional the coherence time τ_{coh}. Consequently, a spatially localized interference pattern is extracted, which spatial extension along the propagation direction is given in first approximation by $v_g \cdot \tau_{coh}$. This statement is an approximation which holds in the case of negligible dispersion, otherwise the measured interference signal will spatially extend due to the pulse envelope reshaping. By changing the optical delay line position, the spatial position on the sample where the interference signal is visible moves. That is, by adjusting the delay time we can track the evolution of the spatial mode profile in time. The signal that is measured can be expressed as:

$$S(x,y) \;=\; C_s\, e^{-\imath\Delta\phi(x,y,\tau_0)}\, \frac{1}{2T} \int_0^T |E_s(x,y,t+\tau_0)||E_r(t)|\; dt, \qquad (2.15)$$

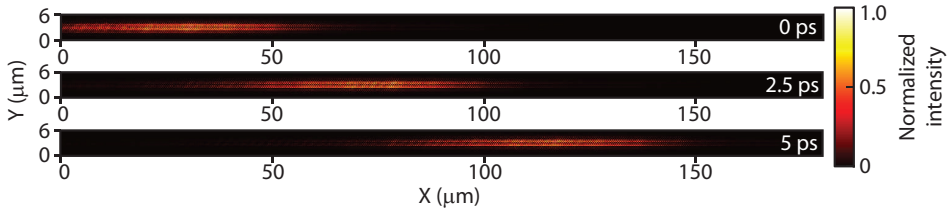

Figure 2.8: Two-dimensional field profile measurements of the intensity of a 2 ps pulse propagating in a PhCW by scanning the probe over a $180 \times 6\,\mu m^2$ *large area for three different delay line positions. Shown is the measured intensity normalized for each frame separately. The waveguide is, as before, located at* $y = 3\,\mu m$ *running along the x-direction. It can be seen how the pulse enters at t=0 ps the scan range from the left. As time progresses the measurement tracks how the wave packet moves to right while it shape stays the same.*

where τ_0 is a fixed delay time. This equation looks very similar to Eq. (2.12) presented for the other operational mode. For every spatial position (x,y) we measure a cross-correlation between the pulses in the two interferometer arms. Importantly, there is a difference to note. The phase of the interference signal that we now measure depends on position as described in section 2.4. Thus, the oscillations that are visible are related to the spatial frequency spectrum, i.e., the wavevector components. In addition, the effect of dispersion is less trivial to extract, since each spatial snapshot in time is built up by scanning the near-field probe over the sample surface. For every data point that the spatial snapshot consists of the pulse has propagated a different distance and accumulated a different phase. Thus, we can easily visualize the change of the pulse in space but not its evolution in time.

A typical example of a series of two-dimensional mode profile measurements is shown in Fig. 2.8. This measurement series illustrates how it is possible to track the spatial field profile of a 2 ps pulse as it propagates in a PhCW. The figure was produced by scanning the near-field probe over a $6 \times 180\,\mu m$ area for three different delay line positions while light from a 2 ps pulsed laser is coupled into the sample. The row of missing holes is again located around $y = 3\,\mu m$. In the first measured frame, it can be seen how the pulse enters the scan range from the left. The inter-

ference pattern is maximum around x = 35 µm and decays to shorter and longer propagation distances. As a result, a wave packet with a FHWM of 35 µm is measured. This spatial extension resembles the expected value for a 2 ps pulse propagating at a group index of 17. As the point in time, that is investigated, is shifted to later times by moving the optical delay line the measured interference pattern moves to the right. In the second frame, the maximum of the wave packet has moved to x = 80 µm, while its shape remains unaltered. Finally, the interference pattern is centered around x = 120 µm in the last frame. In this example, the pulse length, as observed in the snapshots, remains constant. The measurement shows how the spatial field profile of a pulse propagates in space, as time progresses. By tracking the maximum of the pulse over time it is possible to extract the group velocity. The wave packet has moved by 85 µm in a time of 5 ps. This movement represents a group index of 17, which agrees with the determination of the spatial extent of the interference pattern. The fact that the pulse shape does not change significantly illustrates that dispersion is negligible over a propagation distance of 100 µm for the 2 ps pulse.

The decision about which mode of operation is used depends on the information that is required for the experiment. In general, there is a three-dimensional parameter space, one temporal and two spatial parameters, for each measurement series. It is very time consuming to achieve a high resolution in all these parameters. Usually, if there is an interest in the spatial evolution of a propagating pulse the near-field probe will be scanned for a few delay positions and therefore a high resolution in space is achieved. In contrast, if the major interest lies in the temporal evolution and the dispersion it is more useful to perform a series of delay line scans at a small number of locations.

2.6 Conclusion

By means of an aperture near-field microscope operated in collection mode it is possible to investigate light propagating in waveguiding structures. Including the near-field probe in an interferometric setup allows for phase-sensitive measurements of the guided mode. Temporal dynamics of pulse propagation inside waveguides can be investigated by integrating an optical delay line in the near-field microscope and using a light source with limited coherence time. Alternatively, local spectral information will be gained by

means of the near-field microscope, if the light detected up by the probe is spectrally analyzed. The different features and characteristics of the setup were illustrated by performing various measurements on a PhCW.

3

Tracking the spectral evolution of a propagating pulse

ABSTRACT: In this chapter we demonstrate nanoscale photonic point-to-point measurements to characterize a single component inside a composite nonlinear device. We perform spectrally resolved near-field microscopy on ultrashort pulses propagating inside a slow-light PhCW, which is part of a larger sample. A power study reveals a reshaping of the pulse's spectral density, which we model using the NLSE. With the model we are able to identify the various physical processes governing the nonlinear pulse propagation. Finally, we contrast the near-field measurements with transmission measurements of the complete composite sample to elucidate the importance of gaining local information about the evolution of the spectral density.

3.1 Introduction

The ever increasing demands for speed in telecommunication has led researchers to develop a broad variety of all-optical signal-processing elements such as switches [11], demultiplexers [101], buffer lines [102, 14], dispersion compensators [103] or signal regenerators [104, 105]. Many of these devices were demonstrated with PhCWs [51], which have emerged as a promising platform for integrated photonic circuits [46], as described in section 1.5.

Nonlinear optical effects, which allow for the control of light with light [7], are crucial for all-optical signal processing. Conventionally, nonlinear optical properties of a device (e.g. a waveguide) are experimentally determined by analyzing the properties of a transmitted laser pulse for different input powers [106, 107, 108, 109]. In contrast to the linear optics regime, where only the characteristics of the different devices inside the circuit matter, in the nonlinear regime the order in which the different components are arranged is also crucial. Thus, it is a challenging task to extract the characteristics of individual components of an integrated photonic circuit from a single transmission measurement. What is missing is a photonic analogue to electronic point-to-point measurements [110], which would characterize the performance of each component within a nanophotonic chip, instead of measuring the effect of all processes accumulated in the sample.

Near-field microscopy has the potential to address this need. Various operation modes of near-field microscopes have been implemented, as described in chapter 2, that allow the investigation of pulses propagating inside photonic structures. However, local spectral point-to-point measurements on a single component on a photonic chip that, for example, characterize a high intensity ultrashort pulse propagating in the nonlinear regime are so far missing.

In this chapter, we demonstrate how a near-field microscopy technique can be used to track the spectral evolution of such a pulse inside a single component of a more complex photonic chip. We measure the changes of the spectral density as the ultrashort pulse propagates through a slow-light PhCW by monitoring the shape, peak amplitude, mean wavelength and width of the pulse spectrum. Numerical calculations reveal that the spectral reshaping is caused by the interplay between dispersion, nonlinear and free-carrier effects. Finally, we show that the information gained by near-field microscopy allow us to model the pulse propagation inside the PhCW without the need to model the propagation in the rest of the sample,

as is the case when only regular transmission spectra are available.

3.2 Sample and experimental setup

As a model system for our experiment we use a five component sample (Fig. 3.1a). There are two polymer access waveguides, one for each facet, and the silicon PhCW that is connected to the access waveguides with two silicon spot-size converters. The polymer waveguides consist of SU-8 photoresist, are a few millimeters long and have a large cross-section (a width and a height of roughly 5 µm and 2 µm, respectively) to enhance the efficiency of the light incoupling [111]. Each spot-size converter is a 50 µm long inverse taper, whose purpose is to funnel the light from the polymer access waveguides to the PhCW. The PhCW has a length of 80 µm and is therefore at least 10 times shorter than each of the access polymer waveguides.

The PhCW consists of a 220 nm thick silicon membrane which is perforated with air holes. The holes have a radius of 0.29a and are periodically arranged in a triangular lattice (a = 420 nm). One row of holes is not present in the $\Gamma - K$ crystal direction, creating the waveguide. The sample was fabricated by electron-beam lithography, subsequent dry etching and sacrificial wet etching to release the membrane [112]. The two rows of holes directly adjacent to the waveguide are shifted by -0.11a and 0.06a, respectively, to create a spectral slow-light regime with low GVD [59]. A negative shift is defined here as a displacement from the position dictated by the triangular lattice towards the waveguide and a positive shift as a displacement away from the waveguide. To enhance the coupling between the spot-size converters and the slow-light PhCW the first and last ten periods are stretched to a value of 440 nm.

We measure the group index n_g characteristics by means of Fourier transform spectral interferometry [113]. The result, presented in Fig. 3.1b, indicates that there is a plateau of $n_g \sim 60$ between 1577 and 1587 nm. The group index diverges for longer wavelength as the cut-off is approached. For wavelengths shorter than 1577 nm the group index tends to a value of 5. We also calculate the dispersion relation of the slow-light PhCW using MIT Photonics Band (MPB) package [114]. The extracted group index is in good agreement with the MPB calculation (dashed and solid blue curve in Fig. 3.1b, respectively).

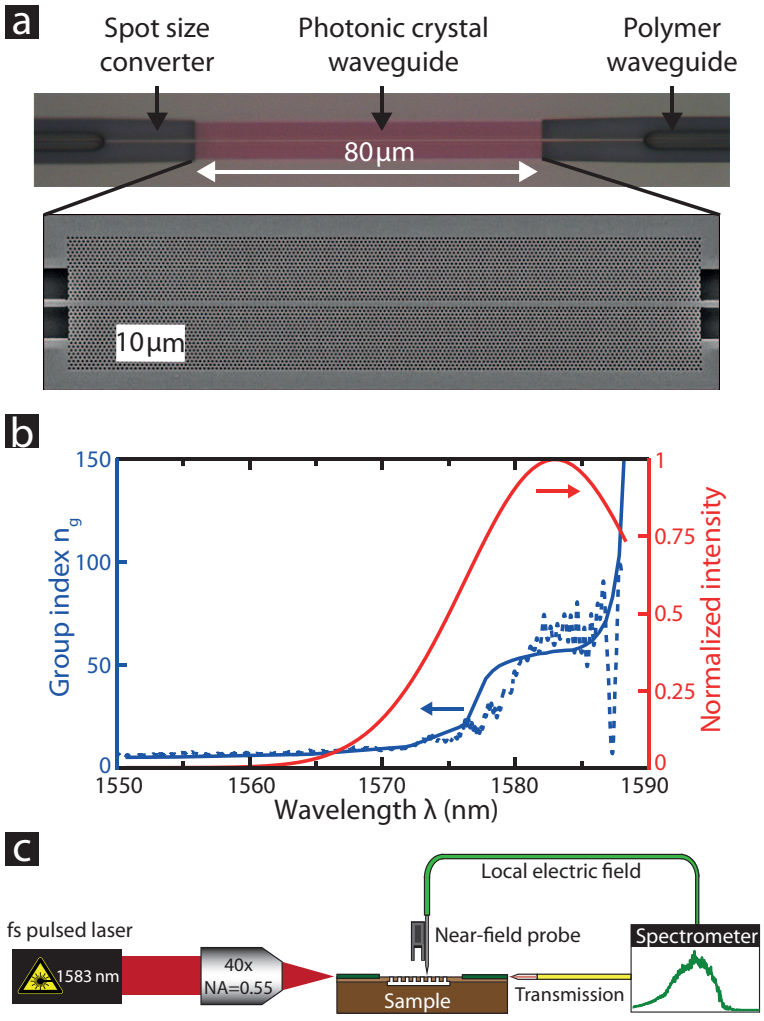

Figure 3.1: a) Optical microscope picture of the central part of the photonic sample. The PhCW is visible in the middle. At the sides, the silicon spot-size converters and part of the polymer access waveguides can be seen. The inset shows a scanning electron micrograph of the silicon PhCW. b) The measured (dashed) and calculated (solid) group index distribution as a function of wavelength (blue, left axes) and the spectral density of the laser coupled into the sample (red, right axis). c) Schematic of our experimental setup.

As shown in Fig. 3.1c, we end-fire couple femtosecond pulses centered at 1583 nm, which are generated by an optical parametric oscillator (Spectra Physics OPAL) into our sample using a 40x aspheric lens (NA=0.55). At the end facet of the sample a lensed fiber collects the transmitted light, which is then spectrally analyzed. The laser delivers bandwidth-limited pulses of a temporal length of 250 fs with a repetition rate of 80 MHz and a concomitant bandwidth of 16 nm (FWHM). To investigate nonlinear optical effects the laser power coupled into the sample can be varied by a neutral density filter. The values of the input power mentioned in this chapter are all determined before the incoupling lens. A maximum limit for the input power of 26 mW is chosen for all experiments to avoid damage to our sample, which was found to occur at ~ 30 mW.

Near-field measurements are performed by means of a home-built spectrally resolved near-field microscope, described in section 2.3. For each spatial measurement point the spectrum is collected while scanning the near-field probe transversally over the waveguide in order to average out the complex lateral field distribution of the PhCW Bloch modes [115]. Note that the resolution is limited by the aperture size which is in our case ~ 250 nm. In principle, the resolution could be pushed further into the nanoscale by decreasing the aperture size which would, however, strongly decrease the amount of collected light.

3.3 Experimental results

First, transmission measurements are performed to characterize the nonlinear response of the complete sample. Figure 3.2a shows spectra measured for six different average input powers ranging from 1.1 to 25.8 mW. The dependence of the shape of the transmitted spectrum on the input power is a clear signature of the presence of nonlinear effects [107]. The most obvious feature is that the peak amplitude does not scale linearly with the input power as shown in Fig. 3.2b. The maximum value of the spectrum increases until 10.5 mW. For higher input powers the peak amplitude declines.

The second feature that can be observed is a blueshift of the spectral density $P(\lambda)$, which we quantify by calculating the mean wavelength $\overline{\lambda}$ of each spectrum

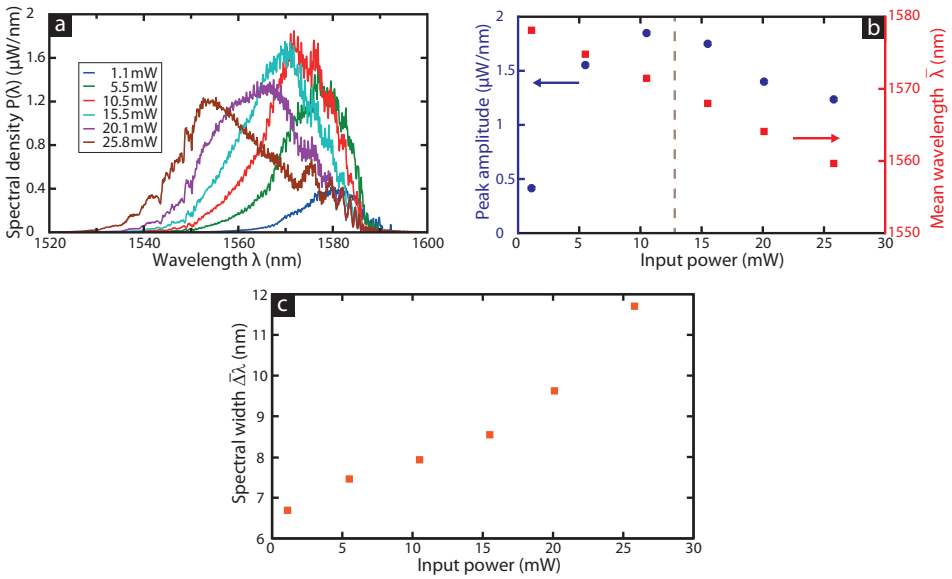

Figure 3.2: a) Transmission spectra for different average input powers. b) The dependence of the peak amplitude and the mean wavelength of the transmission spectra on the input power. The gray dashed line marks the boundary between the regions where the peak amplitude increases, and where it decreases with input power. c) Spectral width of the transmission spectra for the different average input powers.

$$\bar{\lambda} = \frac{\int \lambda\, P(\lambda)\, d\lambda}{\int P(\lambda)\, d\lambda}. \tag{3.1}$$

Figure 3.2b depicts the dependence of $\bar{\lambda}$ on input power. It is clear that the mean wavelength blueshifts at higher powers. In the linear optical regime, we expect to observe a Gaussian-shaped spectrum with a cutoff around 1588 nm, which is indeed the case for low input powers. However, for increasing input power the spectrum changes in shape. In addition to the observed blueshift at higher input powers, the spectral density broadens.

The width of the spectra can be quantified by calculating their second moment, i.e., variance $\Delta\bar{\lambda}^2$, which is defined by

$$\Delta\overline{\lambda}^2 \;=\; \frac{\int\,(\overline{\lambda}-\lambda)^2\;\mathrm{P}(\lambda)\;\mathrm{d}\lambda}{\int\;\mathrm{P}(\lambda)\;\mathrm{d}\lambda}. \tag{3.2}$$

where $\overline{\lambda}$ is the first moment, i.e., mean wavelength, as defined in Eq. (3.1).

The change of the spectral width, which is the square root of the variance, of the transmission spectra with input power is shown in Fig. 3.2c. It is obvious that the spectra get broader with increasing input power. By going from 1.1 to 25.8 mW the spectral width nearly doubles from 7 to 12 nm. In summary, the power dependence of the transmission spectra is clearly indicative of nonlinear pulse propagation.

The transmission spectra represent the response of the complete composite sample. The question that now arises is which of the observed spectral changes occur in the PhCW, and which are due to the other four components of our sample. In order to answer this question, we perform in-situ near-field microscope measurements of the pulse propagating inside the PhCW. Each of the measurements, presented in Fig. 3.3a-c, consists of 19 spectra collected at positions evenly distributed over a distance of 50 µm along the PhCW, for the different input powers. These measurements show that we can determine the spectra of the propagating pulse as a function of position and thereby gain access to its spectral evolution at the nanoscale.

For all input powers we observe various seemingly abrupt amplitude changes between the spectra taken at successive propagation distances. This modulation in the amplitude is an artefact caused by the Bloch nature of the photonic modes in the waveguide. That is, the locally measured electric field amplitude is strongly dependent on the exact position of the probe within a single unit cell [90] and the positional accuracy is mainly limited by the thermal drift and the size of the investigated area of several tens of μm^2. However, the shape of the spectral density does not depend on the probe position within a unit cell. While it is tempting to normalize the data, in doing so we would lose any information about a possible amplitude drop due to absorption, and so we analyze the unnormalized spectra.

Beside these abrupt amplitude variations there is no significant drop in amplitude of the spectral density with propagation visible for an input power of 1.1 mW (cf. Fig. 3.3a). That is, there is no significant absorption occurring inside the PhCW at this low input power. From this and the fact that the shape of the spectrum of the pulse is the same throughout the waveguide, we conclude that nonlinear effects are negligible here. At

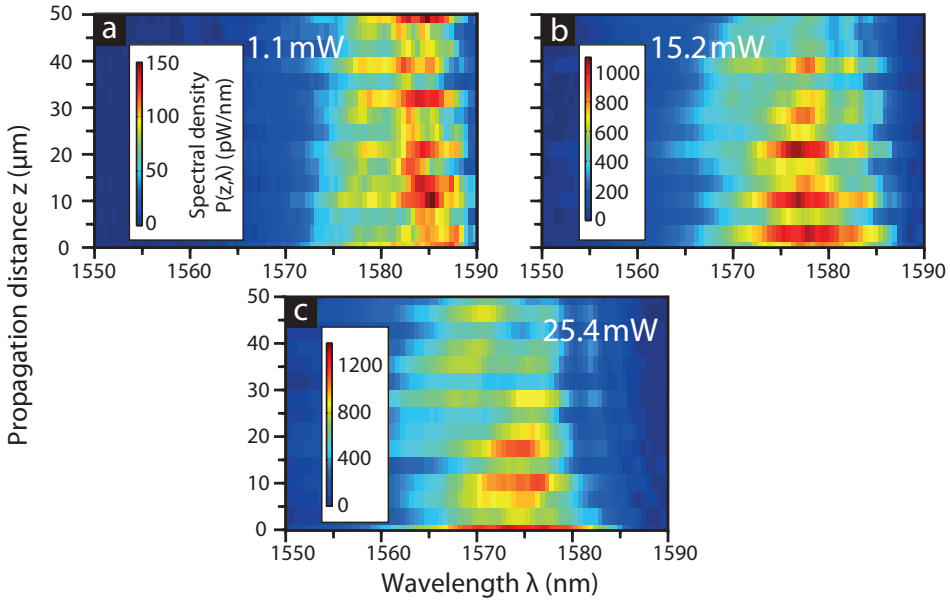

Figure 3.3: Tracking the spectral density of the pulse propagating inside the PhCW. Three near-field measurement series' showing the evolution of the spectral density for average input powers of a) 1.1 mW, b) 15.2 mW and c) 25.4 mW.

15.2 mW the evolution of the spectral density starts to show evidence of nonlinear effects (cf. Fig. 3.3b), since the peak amplitude decays by 50 % in the first 50 µm. For the highest investigated input power, close to the damage threshold, shown in Fig. 3.3c, the amplitude decay of the spectral density occurs even faster. The peak amplitude of the spectral density decreases by 50 % in the first 30 µm. Thus, this series of spectra demonstrate that the pulse experience power-dependent losses during propagation inside the PhCW.

Interestingly, we observe a power dependence of the spectral density at the beginning of the PhCW. To quantify the spectral changes that occurred before the PhCW, we investigate a series of spectra taken after a propagation distance of a few microns after the start of the PhCW for different input powers, shown in Fig. 3.4a. There are 4 different features which can be analyzed: shape, peak amplitude, mean wavelength and spectral width.

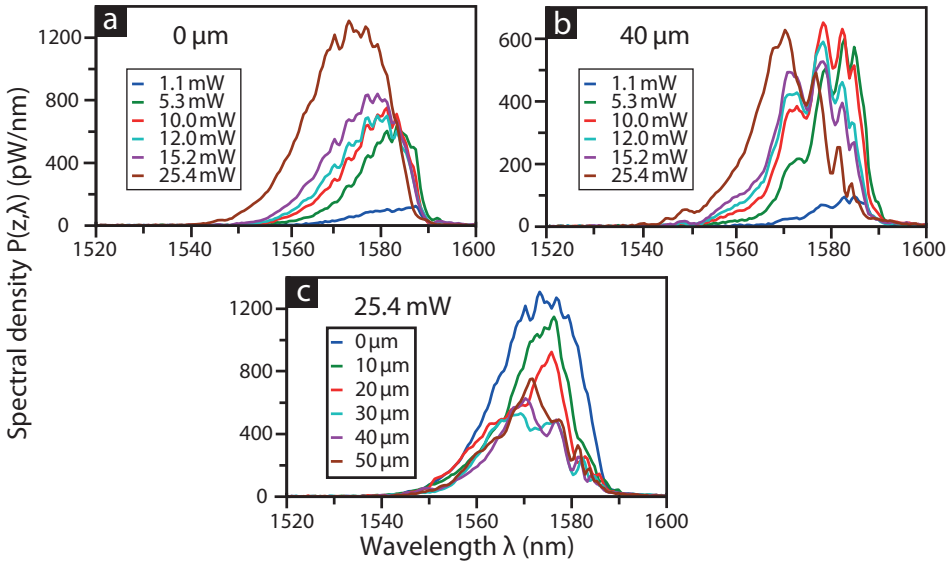

Figure 3.4: Evolution of the shape of the spectral density. A series of spectra taken at the beginning a) and after 40 µm *propagation b) in the slow-light PhCW for different average input powers. c) A series of spectra taken in* 10 µm *steps at an average input power of 25.4 mW.*

First, the shape of spectra at the input of the PhCW remains the same for all input powers, i.e., a Gaussian cut-off at longer wavelength. Second, the peak amplitude of the spectra does not scale linearly with input power (cf. blue dots in Fig. 3.5a). Third, there is a power-dependent blueshift of the spectral density. This wavelength shift can be quantified using Eq. (3.1). As shown in Fig 3.5b, a change of the input power from 1.1 to 25.4 mW results in a blueshift of 8 nm. Fourth, the spectra broaden slightly with input power, i.e., the spectral width (defined in Eq. (3.2)) increases by ~ 1.5 nm between the spectra measured at 1.1 mW and 25.4 mW (cf. blue dots in Fig. 3.5c). These observations suggest that the intensity of the pulse is sufficiently high for nonlinear effects to play a role in the access waveguide or the silicon inverse taper.

To quantify the effect of the PhCW on the changes in the laser spectrum, we measure a series of spectra after 40 µm propagation inside the slow-light PhCW (Fig. 3.4b), for the same range of input powers. A com-

parison of Fig. 3.4a and Fig. 3.4b makes it obvious that the shape of the spectral density changes significantly with input power. Note that after 40 µm inside the PhCW, the spectra measured by near-field microscopy begin to resemble those measured in transmission (Fig. 3.2a). This observation, together with the fact that the shape of the spectra at the beginning of the PhCW is not power-dependent (here we consider a blueshift not a change in shape), shows that the reshaping of the spectral density happens inside the PhCW.

The peak amplitude of the spectra at 40 µm also scales in a nonlinear fashion with input power, but in a more drastic fashion than at the beginning of the PhCW as shown in Fig. 3.5a. At 10 mW the peak amplitude reaches its maximum value, after which it shows a small drop, until finally recovering for 25.4 mW. This scaling of the peak amplitude shows qualitative agreement with the trend observed in the overall transmission spectra (Fig. 3.2b), other than at the highest input power.

In addition, a power-dependent blueshift can be again observed near the end of the PhCW (cf. red squares in Fig. 3.5b). At an input power of 1.1 mW the spectrum has a mean wavelength of 1580 nm which decreases to a value of 1570 nm when the input power is increased to 25.4 mW. Interestingly, this wavelength shift of 10 nm is only slightly larger than the shift observed at the beginning of the PhCW. Moreover, since the transmission spectra exhibit a blueshift roughly twice as large, this suggests that most of the shift in wavelength of the spectral density occurs in the other components of the sample.

A similar observation can be made for the spectral broadening presented in Fig. 3.5c. By comparing the spectral width of the two measurement series we conclude that only a small fraction of the overall spectral broadening occurs inside the PhCW. The transmission spectra show a broadening of 5 nm (cf. Fig. 3.2c) which is three times larger than the broadening observed in the PhCW. Thus, together with the blueshift, the broadening of the spectral density occurs mainly in the other components of the sample, and not in the PhCW. This may seem unexpected, particularly given the slow-light enhancement and the spatial confinement of the light in the PhCW, yet it can be explained with two reasons. First, the pulse is temporally broadened due to dispersion before it enters the PhCW giving rise to a decreased peak amplitude. Second, the blueshift of the spectral density already before the PhCW causes the pulse to experience smaller group

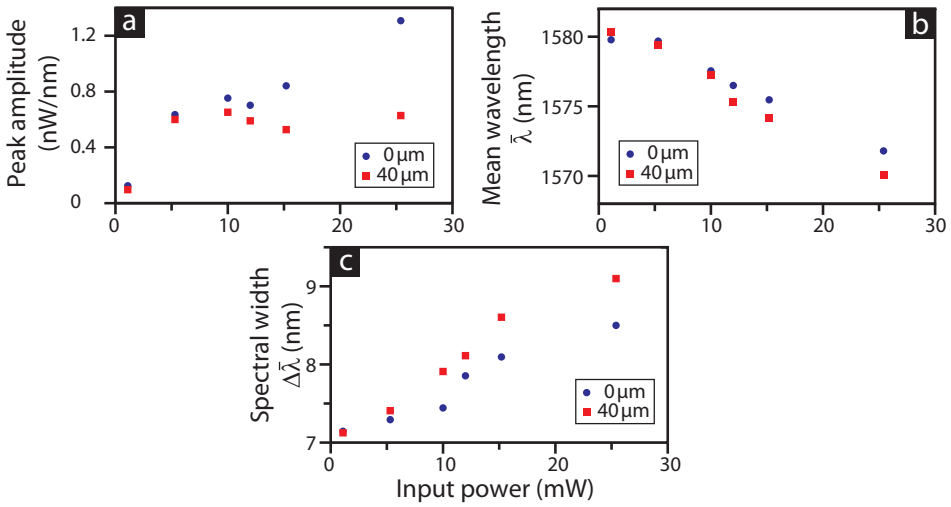

Figure 3.5: Quantifying the changes in the spectral density. a) Peak amplitude , b) mean wavelength and c) spectral width of the spectra series' shown in Fig. 3.4a-b.

indices than would be *a priori* assumed. In essence, the slow-light PhCW has a major effect on the reshaping and the scaling of the peak amplitude, but the blueshift and the broadening of the spectral density occurs mainly in the other components of the sample.

There remains the question about the cause of the spectral reshaping. To answer it we investigate the evolution of the spectral density inside the PhCW at an input power of 25.4 mW by comparing spectra at different locations. This is shown in Fig. 3.4c for six spectra, taken in 10 µm steps. This measurement suggests that there is no energy redistribution inside the spectrum, e.g., energy transfer from the long wavelengths to the shorter ones, since the spectral density taken at the beginning of the PhCW possesses the highest amplitude for each wavelength. Instead it seems more likely that the spectral reshaping originates from different decay behavior of different spectral components, i.e., an increased amplitude drop at the long wavelength side.

In essence, the near-field measurements allow us to separate the spectral reshaping happening inside different devices of an integrated photonic circuit on the nanoscale which is not possible by means of transmission

Parameter	Name	Value
$A_{3,\mathrm{eff}}$	Effective mode area	$0.66\,\mu\mathrm{m}^2$
α	Linear absorption coefficient	20 dB/cm [57]
$\beta_{2\mathrm{PA}}$	2PA coefficient	1 cm/GW [117]
n_2	Kerr coefficient	$6 \cdot 10^{-14}\,\mathrm{cm}^2/\mathrm{W}$ [117]
σ	FCA cross-section	$1.45 \cdot 10^{-21}\,\mathrm{m}^2$ [19]
k_c	FCD coefficient	$1.35 \cdot 10^{-27}\,\mathrm{m}^3$ [17]
τ_{rec}	Free-carrier life time	450 ps [11]

Table 3.1: Parameter names and values used in the numerical calculations. The effective mode area is determined by MPB calculations, whereas the other values are taken from the literature.

measurements. Additionally, the near-field microscopy measurements show that although the polymer waveguides are at least one magnitude longer than the PhCW, most of the spectral reshaping occurs inside the PhCW. This observation confirms the potential of slow-light for enhancing nonlinear optics.

3.4 Modeling and discussion

To gain more insight into the physical processes playing a role in the reshaping of the spectral density we model pulse propagation by means of the NLSE [8], that is described in detail in section 1.2.3. Here, we take dispersion, linear losses due to scattering, 2PA, SPM and free-carrier effects into account. Since the spectrum of our pulse covers a broad range of different group indices we take the full dispersion relation $k(\omega)$ of the PhCW into account. Therefore, we split the NLSE into two equations, one which deals with the nonlinear optical effects and the free-carrier dynamics (based on Eq. (1.11), where β_2, β_3 and $\alpha_{3\mathrm{PA}}$ are set to zero), and one which considers the dispersion [116]. Additionally, Eq. (1.12) (with $\alpha_{3\mathrm{PA}}$ set to zero) has to be solved to describe the temporal evolution of the free-carrier density. The meaning and the value of the parameters used in the model can be found in table 3.1.

Concerning the free-carrier dynamics, 2PA is the only generation source as we are working in silicon with near-infrared light where single photons do not possess enough energy to bridge the electronic band gap. The free-

carrier lifetime has a value of a few hundred picoseconds in silicon structures featuring a large surface area [11]. Since the temporal pulse length is much shorter than the free-carrier lifetime, the amount of carrier recombination during pulse propagation is negligible. Moreover, free-carrier accumulation between pulses is disregarded since the time between subsequent laser pulses is 12.5 ns and therefore much longer than the carrier lifetime.

In contrast to the nonlinear effects and the free-carrier dynamics which are dealt with in the time domain, it is easier to treat dispersion in the frequency domain. Here the temporal broadening of the pulse envelope can be described as a simple differential equation for the spectral density $\widehat{\mathrm{A}}(\mathrm{z}, \omega)$:

$$\frac{\partial \widehat{\mathrm{A}}(\mathrm{z}, \omega)}{\partial \mathrm{z}} \;=\; \mathrm{i}\mathrm{k}(\omega - \omega_0)\widehat{\mathrm{A}}(\mathrm{z}, \omega), \tag{3.3}$$

where $\widehat{\mathrm{A}}(\mathrm{z}, \omega)$ is the temporal Fourier transform of $\mathrm{A}(\mathrm{z}, \mathrm{t})$.

We fit our model to the measured pulse evolution by adjusting only two parameters: a simple scaling factor modeling the near-field probe pickup-efficiency, and a number that describes the chirp the pulse experiences in the polymer access waveguide and the silicon spot-size converter. This latter parameter determines the temporal length of the pulse at the beginning of the PhCW. As starting conditions we use the first spectrum, taken at the beginning of the PhCW, and set the free-carrier density $\mathrm{N_c}$ to zero. The best agreement between the model and the experimental results is achieved with a temporal length of 1.38 ps (FWHM). This amount of temporal broadening is reasonable considering the few millimeter distance that the pulse has to propagate through the sample before it enters the PhCW. The blueshift of the spectral density, which occurs either inside the polymer access waveguide or the silicon spot-size converter, is taken into account in the modeling by shifting the center frequency of the pulse in a one-time fit to the spectrum measured at the beginning of the PhCW (cf. Fig. 3.4a).

In addition, the slow group velocity of the light inside the PhCW is accounted for, since it enhances nonlinear effects as well as interactions of the pulse with free carriers [57]. The slow-light enhancement is discussed in detail in section 1.5.2 leading to effective parameter values, which scale differently with the slowdown S. It is crucial to account for the frequency dependence of the slowdown factor S, which is mimicked by solving our model

several times, once per investigated wavelength, and taking the group index valid at that wavelength into account for the slow-light enhancement. Thus, for the sake of simplicity our approach inherently assumes that S is constant and we only investigate how one specific spectral component evolves with propagation. If we wanted to investigate the evolution of the complete spectrum of the pulse, we would have to slice the spectral density and calculate the evolution of these slices by solving the model repeatedly. To minimize the computation effort and still show that this approach delivers accurate results, we investigate only three different wavelengths, namely 1565, 1575 and 1580 nm, which feature different group indices with values of 7, 18 and 53, respectively.

Figure 3.6 presents a comparison between typical modeling results and data taken from the near-field measurements (Fig. 3.3c). The figure shows how the three spectral components decay with propagation inside the PhCW. Clearly, the longest wavelength experiences the fastest amplitude decay. In contrast, the amplitude of the shortest wavelength stays constant. In all cases we find an excellent quantitative agreement between the modeling and the experimental results, using material parameters found in literature. Over the small wavelength range that our pulses span the material parameters of the PhCW are practically constant while the group index varies greatly (cf. Fig. 3.1b). Hence, different wavelengths of light within the PhCW experience vastly different slowdown factors, and it is this dispersion of the slow-light enhancement that causes the observed spectral density reshaping.

The rapid amplitude variation with distance visible in the experimental data originate from the positioning uncertainty of the probe inside the PhCW unit cell, as mentioned before. Consequently, the error bars represent the standard variation of the intensity distribution of the guided mode inside a unit cell of the PhCW. Details about the calculation of the error bars can be found in the appendix of this chapter. It is obvious that the error bar for the longest wavelength is too small to explain the magnitude of the amplitude variation at this wavelength. The reason for this discrepancy is as yet unknown.

We now turn to discuss the influence of the different physical effects that occur during the pulse propagation, which can be separated in two categories: (I) those that lead to losses and (II) those that change the shape of the spectrum. There are three processes which might lead to an

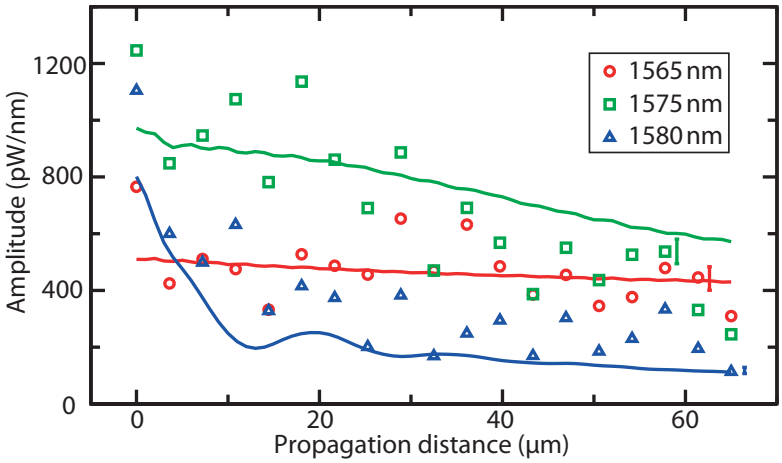

Figure 3.6: The experimentally (points) and theoretically (solid curves) determined spectral amplitude as a function of propagation distance at three different wavelengths. The experimental data is taken from Fig. 3.3c where the average input power is 25.4 mW. For each wavelength an error bar is depicted on the right side of the figure.

amplitude decay with propagation: scattering, 2PA and FCA. The linear losses due to scattering are too small to have a significant impact over a 50 µm distance which we also observe in our measurements, since there is no attenuation visible at the lowest input power (cf. Fig 3.3a). Thus, the measured amplitude decay at higher powers is mainly caused by 2PA and FCA.

SPM and FCD are usually considered to be the source for spectral reshaping such as a blueshift [19]. However, in our experiment both processes do not have a significant influence on the spectral shape, since there is no wavelength shift of the complete spectrum or spectral broadening with propagation visible (cf. Fig 3.4c). Instead, the reshaping is caused by dispersion of the PhCW, which in general has a threefold influence. First, a large dispersion stretches the pulse temporally and therefore limiting its peak intensity. Second, a wavelength dependence of the effective materials parameters discussed above is created. Third, it also causes a wavelength dependence of the free-carrier effects leading to an enhanced decay of the slower propagating spectral components, i.e., longer wavelengths. This is

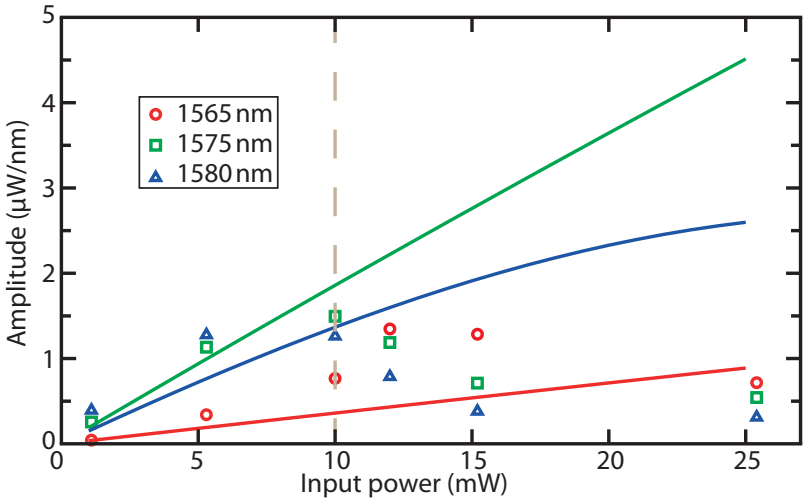

Figure 3.7: The experimentally (points) and theoretically (solid curves) determined spectral amplitude as a function of average input power for 3 different wavelengths. The experimental data is taken from Fig. 3.2a. The gray dotted line marks the input power after which the measured and calculated evolutions of the spectral density differ significantly.

explained by the build-up of the free-carrier density in time between the rising and trailing edge of a single pulse so that the trailing edge, containing longer wavelengths, will experience enhanced FCA and FCD [118]. In essence, the spectral reshaping stems from the wavelength-dependent slowdown factor S and an interplay of dispersion and the temporal dynamics of the free carriers.

Next, we demonstrate that a similar approach, which uses the transmission spectra from the entire composite sample (cf. Fig. 3.2), does not accurately predict the spectral evolution in the PhCW. We again apply the model using the same parameter values and assume that there are no nonlinear effects inside the polymer access waveguide and spot-size converter. Only the temporal broadening that occurs before the PhCW is taken into account.

We try to model the evolution with input power of the same three wavelengths as before and compare it with experimental data taken from the transmission measurements, as shown in Fig. 3.7. There is a clear discrep-

ancy between the model and the experiment. First, the model no longer reproduces the scaling of the amplitudes with input power. The measured amplitudes of all spectral components show a decrease with input power for the highest input powers, whereas the modeling results feature a steady increase. Second, the blueshift visible in the measurement is not reproduced by the model. In the measured data, at the lowest input powers the longest wavelength exhibits the highest amplitude, whereas for high input powers the shortest wavelength has the highest amplitude, while the model does not exhibit this behavior. Hence, the model can reproduce neither the peak amplitude scaling nor the power-dependent spectral reshaping visible in the transmission measurements. Note that we here found no set of physical parameters that allow reproducing the experimental results.

Overall, it seems that the discrepancy between our transmission measurements and the model can be explained by a power-dependent absorption process, which is missing or underestimated in the modeling approach at higher input powers. We understand this discrepancy in terms of the blueshift that occurs before the PhCW. The blueshift transfers energy to a spectral region with higher dispersion, so that the spectral density covers a larger range of group indices. This leads to a dramatic enhancement of the reshaping, as explained above, for increasing input power.

This interpretation can also be backed up with our experimental observations. For input powers higher than 15.2 mW, we observed a change in the spectral reshaping in the transmission spectra (Fig. 3.2a) as well as in the near-field measurements (Fig. 3.4b). The measured spectral density is no longer centered on the flat dispersion band at 1580 nm, but shifted towards 1570 nm, where the group index changes significantly with wavelength. Thus, the strong reshaping goes hand in hand with and is actually influenced by the blueshift before the PhCW. In essence, the failure of the model to reproduce the evolution of the transmission spectra of the composite structure shows that obtaining the nonlinear optical behavior of the PhCW that is part of a composite structure is far from trivial, since the other components may have a non-negligible influence.

3.5 Conclusion

In conclusion, we presented a near-field microscopy technique which can be used to test and evaluate nonlinear pulse propagation inside single com-

ponents of integrated photonic circuits on the nanoscale in analogy to the wafer testing applied in the electronic industry. This approach allowed us to gain information about the evolution of the spectral density inside the composite sample and to unravel the different physical processes occurring during ultrashort pulse propagation. Specifically, the observed spectral reshaping is mainly caused by nonlinear optical effects inside a slow-light PhCW and can be understood by an interplay between dispersion, free-carrier effects and a wavelength-dependent slow-light enhancement of various nonlinear effects. Reaching the same insight with only conventional transmission measurements, which reflect the behavior of the complete sample, is far from trivial, since the characteristics of the different components influence each other in a complex manner in the nonlinear optical regime.

Appendix

Experimental amplitude variations due to Bloch mode profiles

As mentioned above there is a positional inaccuracy when placing the near-field probe always at a single position inside a unit cell of the PhCW, throughout the measurements. The Bloch modes of the PhCW exhibit a significant amplitude modulation within a single unit cell [90]. As a consequence, we observe an amplitude modulation of the entire spectra taken by the near-field microscope. To quantify the possible variation of the signal, we simulate the intensity of the mode inside the PhCW by using MPB [114]. To obtain a coarse estimate of the amplitude modulation in the experiment we convolute the calculated intensity profile with a circle of 250 nm to mimic the effect of the aperture size of the near-field probe. For a more detailed description of the image formation of a PhCW Bloch mode in near-field microscopy the reader is referred to [81]. The results for the three wavelengths, which are also investigated and modeled in the main text, are shown in Fig. 3.8a-c.

Since we scan the near-field probe transversally over the PhCW to counteract the different extension of the mode profiles visible in the MPB calculations, we integrate the simulated intensity distribution over the x-axis resulting in sinus curves with different modulation depths as shown in Fig. 3.8d-f. The error bars in Fig. 3.6 are calculated by determining the

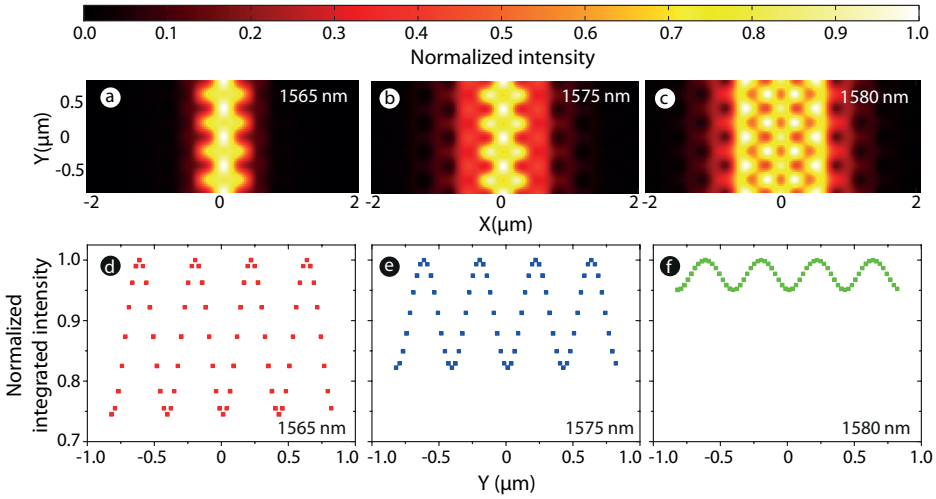

Figure 3.8: Calculated intensity distribution of the mode guided in the PhCW convoluted with a 250 nm diameter circle for a wavelength of a) 1565 nm, b) 1575 nm and c) 1580 nm for four unit cells of the PhCW. Corresponding transversally integrated intensity curves.

ratio of the standard variation to the mean value of these integrated intensity curves, which are listed in table 3.2. It is clear that the intensity profile at the shortest wavelength features the biggest modulation along the propagation direction leading to the largest error bar. For increasing wavelength, the modulation decreases.

Wavelength	Mean	Standard variation	Ratio
1565 nm	0.87	0.09	10.38 %
1575 nm	0.91	0.063	6.93 %
1580 nm	0.98	0.018	1.8 %

Table 3.2: Mean value, standard variation and their ratio for the curves shown in Fig. 3.8d-f.

4

Soliton fission in InGaP photonic crystal waveguides

ABSTRACT: In this chapter we describe the first direct observation of soliton fission in a PhCW. We investigate the propagation of a second-order soliton in an InGaP PhCW, by directly visualizing the time evolution of a picosecond pulse launched in the structure with time-resolved near-field microscopy. We observe how a wave packet breaks apart into three wave packets after a record short fission length. We compare the experimental results with a semi-analytical NLSE model that describes the nonlinear pulse propagation. The model shows that the soliton fission is caused by free-carrier effects, which is the first proof that free carriers can behave as a significant perturbation for soliton propagation. Finally, we study the temporal dynamics of the wave packets generated in the fission event, where we observe their acceleration and deceleration.

4.1 Introduction

The interplay between GVD and SPM can generate waves which are called temporal solitons [20]. These nonlinear waves show a special behavior as they propagate through dispersive media, as discussed in section 1.2.5. The archetypical example of a temporal soliton is a wave packet which does not show any changes in both the temporal and the spectral domain.

Additional effects other than GVD and SPM may disrupt the balance required for soliton propagation. As a consequence, higher-order solitons will be perturbed and they will break apart into several fundamental solitons, which is called soliton fission. In optical fibers it has been shown that, for example, Raman scattering [22] or higher-order dispersion like TOD [21] can initiate such a soliton fission event.

Concurrently with soliton fission, very often supercontinuum generation occurs [119], i.e., the generation of extremely broadband white light radiation that is spatially coherent. These special light sources have been proven to be extremely useful in a variety of different applications, ranging from frequency metrology [25] to optical communications [26].

In recent years there has been a drive to integrate supercontinuum generation on chip. That is, researchers try to generate soliton fission on much shorter length scales than in PhC fibers, where soliton propagation is typically observed. Recently, it has been demonstrated that soliton propagation can also occur in nanoscale waveguides [108, 120], where a high nonlinearity can be achieved and the dispersion can be engineered. A waveguiding structure that is ideally suited to investigate temporal soltions is a PhCW. In this waveguide there is a large degree of freedom to design and tailor the dispersion [59]. Further, large nonlinearities can be reached through a contribution of high spatial confinement and slow-light enhancement [55]. So far, the temporal dynamics of soliton propagation in PhCWs have been studied by a combination of transmission measurements and numerical modeling [61, 121].

A direct visualization and detailed investigation of a soliton fission event, which is the seed process for supercontinuum generation, has thus far been lacking. A better understanding of this event might enable supercontinuum generation on short length scales on an integrated chip, providing a compact broadband light source for performing, for example, on-chip spectroscopic measurements.

In this chapter we investigate the fission of a second-order soliton prop-

agating in a PhCW. A time-resolved near-field microscope enables us to directly investigate the temporal evolution of the wave packet during propagation. Since the higher-order soliton propagates inside a semiconductor waveguide different physical effects can occur than in optical fibers. We demonstrate that in the PhCW the soliton is perturbed by free-carrier effects which is shown for the first time to be the trigger for a fission event. Moreover, we report a record short fission length of 166 µm. Additionally, we explore the propagation velocity of the various wave packets created in the fission event. We show that there is a time delay between different wave packets, which increases with increasing power. Whereas some wave packets exhibit an acceleration with power others decelerate.

4.2 Soliton propagation and transmission measurements

To observe the breaking apart of a higher-order soliton on a length scale, which is available on a photonic chip, we require a waveguide which features a strong dispersion, i.e., a short L_D. Consequently, we choose for our experiment a 1.5 millimeter long PhCW (illustrated in Fig. 4.1a). This structure is created by perforating a 190 nm thin indium gallium phosphide (InGaP) membrane with air holes periodically arranged in a triangular lattice. The lattice has a period of a = 471 nm and the positions and the radii of the holes closest to the line defect have been altered to design the dispersion of the guided mode (see inset in Fig. 4.1a). A detailed description of the dispersion engineering can be found in [122]. In the wavelength region between 1550 and 1557 high group indices (i.e. ranging between 12 and 18) are achieved together with anomalous dispersion, visible as a negative GVD β_2 coefficient (shown in Fig. 4.1b-c). Further, it has been shown that other effects beside GVD and SPM, e.g., like the generation of free carriers [123], can have a significant on light propagation in InGaP PhCWs. Consequently, we potentially fulfill the conditions required for observing soliton fission. Due the use of a wide gap semiconductor like InGaP (E_g = 1.9 eV) 2PA does not occur for wavelengths in the telecom regime. Thus, the Kerr effect and therefore SPM is dominant and nearly ideal soliton dynamics can be observed [61]. This is in contrast to two-photon absorption limited materials like silicon where free-carrier effects are usually dominant. Further, there are short inverse tapers at the end facets of the sample to

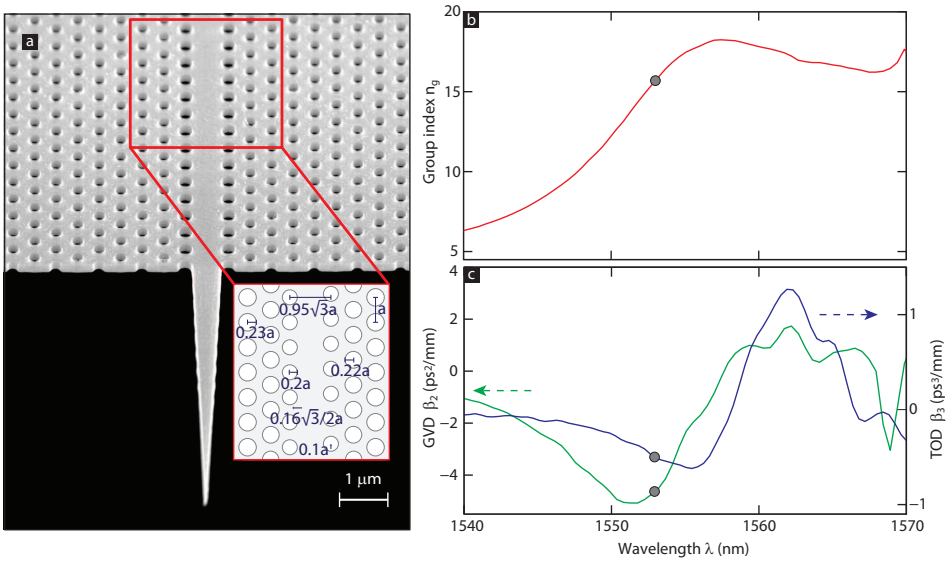

Figure 4.1: PhCW and its dispersion properties. a) SEM micrograph of the PhCW consisting of a thin InGaP membrane perforated by air holes. The inset illustrates the geometry changes for engineering the dispersion of the guided mode. b) Group index n_g of the guided mode as a function of wavelength. c) GVD (green line) and TOD (blue line) coefficients as functions of wavelength. The gray dot marks the graphs for the wavelength with which the experiment is performed.

minimize the insertion loss [124]. Consequently, the sample consists only of the PhCW and the inverse tapers. This is contrast to the more complicated structure of the sample investigated in chapter 3.

We use a 2.2 ps (FWHM) fiber laser (PriTel), which delivers hyperbolic-secant-shaped pulses, as the light source. We couple the laser light into our sample with a 30x objective (NA = 0.4). We chose 1553 nm as center wavelength since, at this wavelength the PhCW features anomalous dispersion ($\beta_2 = -4.6\,\mathrm{ps}^2/\mathrm{mm}$), as required for soliton propagation, and a large group index ($n_g = 15.7$). The GVD leads to ad dispersion length of $L_D = 333\,\mu\mathrm{m}$. The TOD is negligible small, since the corresponding dispersion length is more than an order of magnitude larger than for GVD: $L'_D = 0.183 \cdot T_0^3/|\beta_3| = 3.69\,\mathrm{mm}$ with $\beta_3 = -0.53\,\mathrm{ps}^3/\mathrm{mm}$, which is considerable longer than the PhCW. With the focusing lens at the input facet

we obtain an incoupling efficiency of $\sim 15.9\,\%$ (insertion loss of $-8\,\mathrm{dB}$). As a consequence, the pulse in the waveguide has a peak intensity of 5.3 W for a time-averaged input power of $1300\,\mu\mathrm{W}$, resulting in $L_{NL} = 93\,\mu\mathrm{m}$. At this input power, we actually excite a second-order soliton, as can be seen by inserting the dispersion length and the nonlinear length into Eq. (1.13).

As a first step we measure the spectral density of the pulse transmitted through the sample. We use a lensed fiber ($NA = 0.4$) to collimate the light exiting the end facet of the sample. The transmitted light is spectrally analyzed with an optical spectrum analyzer (OSA). A power study is performed to track the spectral changes occurring due to nonlinear optical effects occurring inside the PhCW. Figure 4.2 shows the measured spectral densities of the transmitted light for peak powers of 0.4, 2.9 and 5.3 W normalized to their respective maximum amplitude. As can be seen for the lowest peak power of 0.4 W, the transmission spectrum consists of a hyperbolic-secant-shaped envelope. This overall shape is modulated with small fringes with a periodicity on the subnanometer regime. These fringes are probably caused by an etalon effect. The periodicity of the fringes would be related to an optical path length in the millimeter regime, depending on the group index of the component where the etalonning occurs. Consequently, there are various optical elements, which could be the origin of the fringes by forming a Fabry-Pérot cavity. Most probably, the fringes are not caused by the reflections at the end facets of the sample, since the reflectivity is very small (i.e. 1.3 % [124]). The envelope is symmetric around a center wavelength of 1553 nm, as expected.

By increasing the peak intensity to 2.9 W the envelope of the transmission spectrum changes in shape, developing a dip at a wavelength of 1553 nm. Correspondingly, the envelope of the transmission spectrum now features two peaks, one at a wavelength of 1551.5 nm and one at a wavelength of 1553.8 nm. Moreover, the spectral density is no longer symmetric around 1553 nm, but the amplitude of the peak at shorter wavelengths is roughly twice that of the other peak. Finally, by increasing the peak power to 5.3 W the envelope of the transmission spectrum becomes even more antisymmetric. While there are still two peaks, the peak at shorter wavelengths shifts to 1550.5 nm, whereas the position of the other peak stays roughly constant. Further, there is a larger amplitude difference between the two peaks. The amplitude of the peak at longer wavelengths is much less pronounced, reaching only 16 % of the amplitude of the second peak.

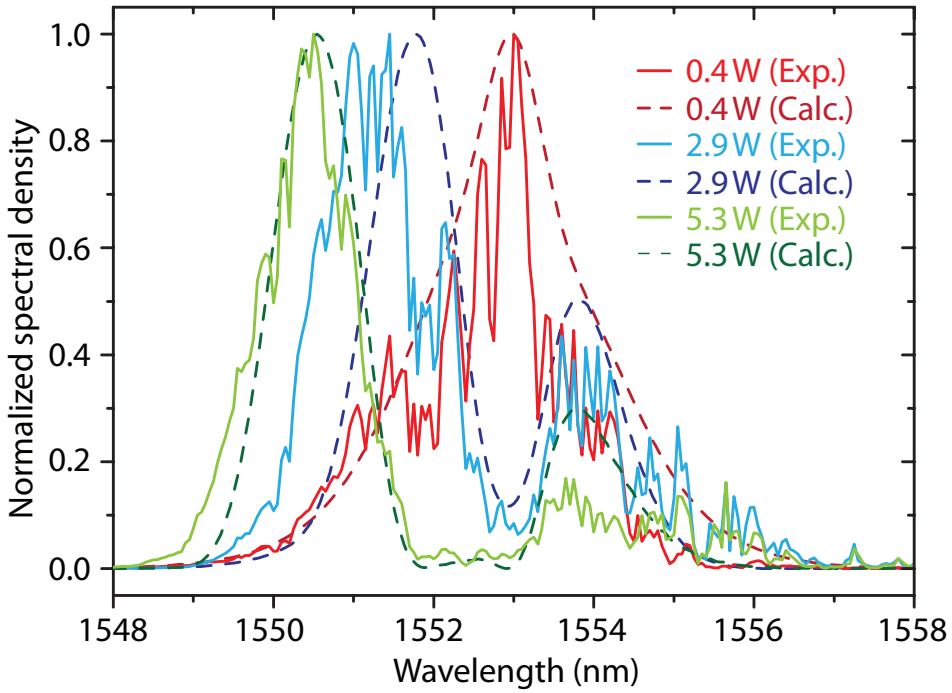

Figure 4.2: Normalized spectral densities of pulses transmitted through the PhCW for three different peak power as measured in experiment (solid lines) and as obtained from calculations with the NLSE (dashed lines).

We compare the measured transmission spectra with a modeling result to gain insight into the pulse propagation in the PhCW. We use the NLSE (see section 1.2.3). In the auxiliary equation to describe the temporal evolution of the free-carrier density we ignore free-carrier recombination, because the free-carrier lifetime is much longer than the pulse length. The parameters for the linear and nonlinear properties used in the NLSE and their corresponding values are described in table 4.1. Here, we listed the effective values, which already include the slow-light enhancement and the effective mode areas as discussed in sections 1.2.3 and 1.5.2.

To model the evolution of the transmission spectrum with increasing power we calculate the spectral density of the pulse after propagation through the 1.5 mm long PhCW. Additionally, we account for pulse propagation through 2 m of optical single mode fiber before the waveguide. It

symbol	parameter name	value
α	Linear absorption coefficient	$40\,\mathrm{dB/cm}$
β_2	GVD coefficient	$-4.6\,\mathrm{ps^2/mm}$
β_3	TOD coefficient	$-0.53\,\mathrm{ps^3/mm}$
γ_{eff}	Effective nonlinear parameter	$1792\,(\mathrm{W\cdot m})^{-1}$
$\alpha_{3,\mathrm{eff}}$	Effective 3PA parameter	$2.5\cdot10^{-26}\,\mathrm{m^3/W^2}$
$k_{c,\mathrm{eff}}$	Effective free-carrier dispersion coefficient	$-3.7\cdot10^{-27}\,\mathrm{m^2}$
σ_{eff}	Effective free-carrier absorption coefficient	$2.8\cdot10^{-21}\,\mathrm{m^2}$
$A_{3,\mathrm{eff}}$	Effective mode area (for $\chi^{(3)}$ effects)	$0.33\,\mu\mathrm{m^2}$
$A_{5,\mathrm{eff}}$	Effective mode area (for $\chi^{(5)}$ effects)	$0.35\,\mu\mathrm{m^2}$

Table 4.1: Model parameters and their corresponding values. The values of α, β_2 and β_3 are measured by low-coherence reflectometry [125]. The effective 3PA coefficient $\alpha_{3,\mathrm{eff}}$ is extracted from an input-output power measurement as described in literature [109], whereas the effective mode areas $A_{3,\mathrm{eff}}$ and $A_{5,\mathrm{eff}}$ are determined with FDTD simulations. The value of the Kerr coefficient n_2 required to calculate γ_{eff} is taken from literature [126]. The values for the FCA and FCD parameter are extrapolated from data known for III-V semiconductor and the Drude model [127]. The enhancement of the various parameters due to the slowdown in the PhCW is already included.

turns out that the spectral density of the pulse is slightly broadened due to SPM in the fiber. We can observe good quantitative agreement between the modeled and measured spectral densities. For a peak power of 0.4 W the model predicts a symmetric spectrum centered around the wavelength of 1553 nm, which matches very well the envelope of the measured transmission spectrum. The spectral fringes are missing since we did not take any possible cause into account in the model. Moreover, since the calculation results show such good agreement with the experimental results, we see no problem in neglecting the spectral fringes. The model is also able to describe the main features of the spectral evolution for the other two peak powers. For example, the formation of the dip at 1553 nm and the increasing asymmetry are well reproduced. Consequently, our model seems to be a good representation of the pulse propagation in the PhCW and thus we continue to use the NLSE with the used parameters for all further calculations.

4.3 Predicting soliton fission

Having compared model calculations to the measured input-output characteristics, we continue to use the model to predict what happens inside the sample during pulse propagation. We investigate how the temporal envelope changes with propagation distance. For a low peak power of 0.4 W we mostly observe a symmetric broadening of the envelope (see Fig. 4.3a). Concurrently, the peak amplitude decays. The peak intensity is so low that we are still in the linear optical regime and GVD dominates the pulse evolution.

At a peak power to 5.3 W we observe that a higher-order soliton is generated, as predicted above (see Fig. 4.3). The temporal compression, which is typical for a higher-order soliton, is clearly visible in the first 160 µm of propagation. At the point of highest temporal compression, which happens after a distance of $\sim 166\,\mu m$ in agreement with Eq. (1.16), the soliton splits into three wave packets. These three wave packets propagate with different group velocities, and therefore they separate in time. One wave packet arrives earlier meaning that it features a higher group velocity than the higher-order soliton and the one wave packet that does not change its propagation speed (and therefore remains centered at time zero). The last wave packet features a lower group velocity than the higher-order soliton and as consequence shows a shift to positive times with distance. Most of the energy resides in the faster propagating wave packet and the least energy is contained in the slower propagating wave packet. All wave packets broaden in time and exhibit a corresponding decay in peak amplitude.

This temporal splitting of generated the wave packets is typical for a soliton fission event and is related to changes in the spectral density of the guided mode [128]. We have observed that at high peak powers the transmission spectrum splits into two peaks, which shift away from the central wavelength with increasing peak power (cf. Fig. 4.2). The splitting of the spectrum explains the different group velocities for the wave packets generated by the soliton fission event. Due to the dispersion relation of the guided mode a wavelength shift translates to a change in group index. Most of the energy in the transmission spectrum showed a blueshift with increasing peak power. These spectral components constitute the wave packet, which features a higher group velocity. The spectral density contained in the peak shifting to the longer wavelength side forms the wave packet that exhibits a lower group velocity. Finally, the spectral compo-

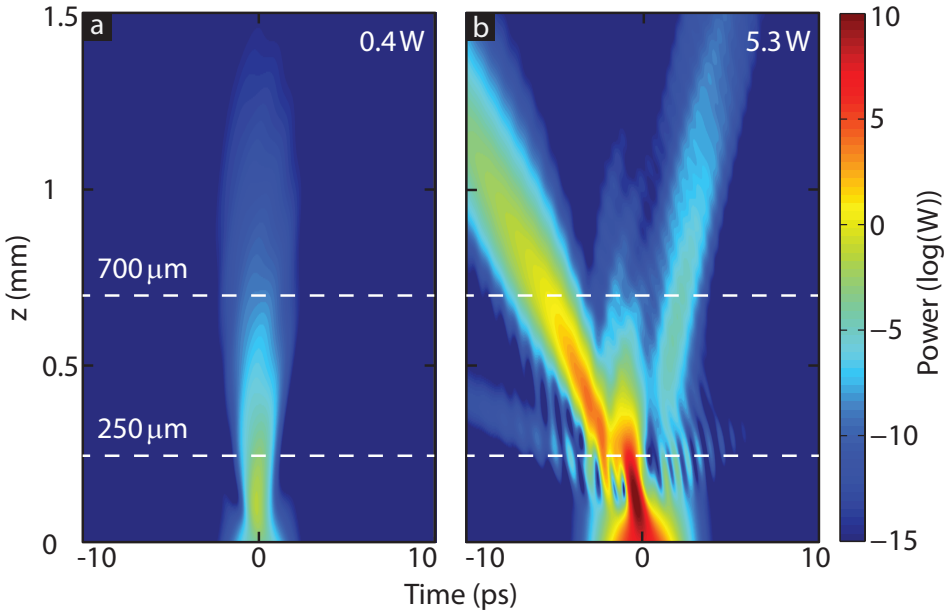

Figure 4.3: NLSE modeling of the evolution of the temporal pulse envelope during propagation inside the PhCW. a) For a peak power of 0.4 W the pulse broadens symmetrically due to GVD. b) At a peak power of 5.3 W, a higher-order soliton is generated, which fissions after a propagation distance of 166 µm *into three wave packets. The white dashed lines indicate the propagation distances at which near-field microscope measurements are performed.*

nents that do not shift in wavelength give rise to the wave packet, which shows no change in group velocity.

4.4 Direct measurement of soliton fission

The model predicts a soliton fission event during propagation inside the PhCW. We use a time-resolved near-field microscopy to experimentally visualize the temporal evolution of a pulse during propagation. First, we measure at an average input power of 0.4 W peak power at two propagation distances: 250 µm and 700 µm (shown as white lines in Fig. 4.3). At this power, we expect to be in the linear optical regime as discussed for Fig. 4.3a.

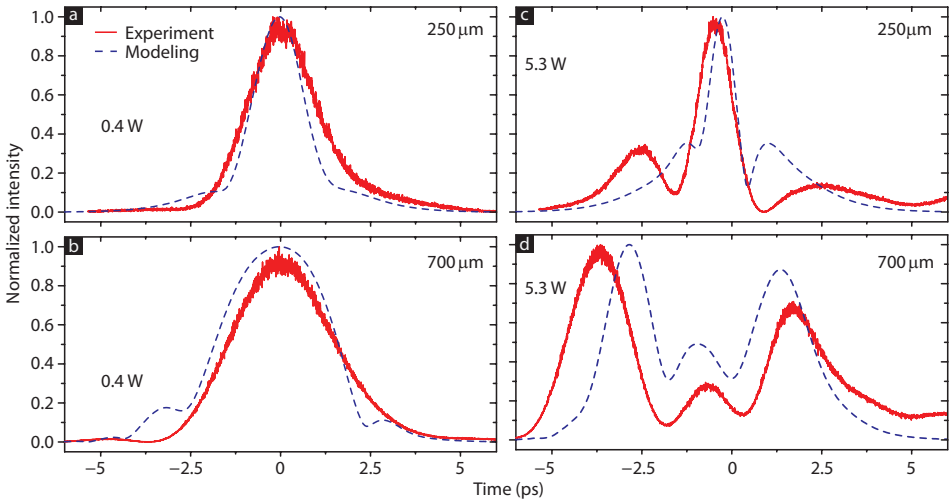

Figure 4.4: Comparison of near-field microscope measurements with NLSE modeling results of the temporal pulse envelope. At a peak power of 0.4 W we observe a Gaussian wave packet in the experiment (red solid line) as well as in the modeling (blue dashed line). By propagating a distance of 450 µm *from* 250 µm *(a) to* 700 µm *(b) away from the entrance facet the pulse envelope shows a symmetric broadening by 40 %. By increasing the peak power to 5.3 W the pulse exhibits a temporal compression of the main wave packet and the emergence of extra wave packets at a propagation distance of* 250 µm *(c). After a propagation distance of* 700 µm *the indications of the soliton fission having occurred are more pronounced (d), since the satellite pulses now contain most of the energy.*

At 250 µm, we measure the Gaussian shaped pulse envelope with a FHWM of 2.1 ps shown in Fig. 4.4a, which basically represents the pulse length of the laser as expected. At 700 µm we observe a pulse envelope which is symmetrically broadened around the zero point in time to a FWHM of 2.96 ps (see Fig. 4.4b). This shows that the pulse has broadened by 40 % by propagating 450 µm in the PhCW. This observation nicely agrees with the calculated dispersion length of 330 µm. Moreover, the fact that the pulse has only broadened symmetrically around the zero point in time proves that higher-order dispersion is negligible, in agreement with the calculated dispersion length of TOD $L_{D'} = 3.69\,\text{mm} >> 450\,\mu\text{m}$.

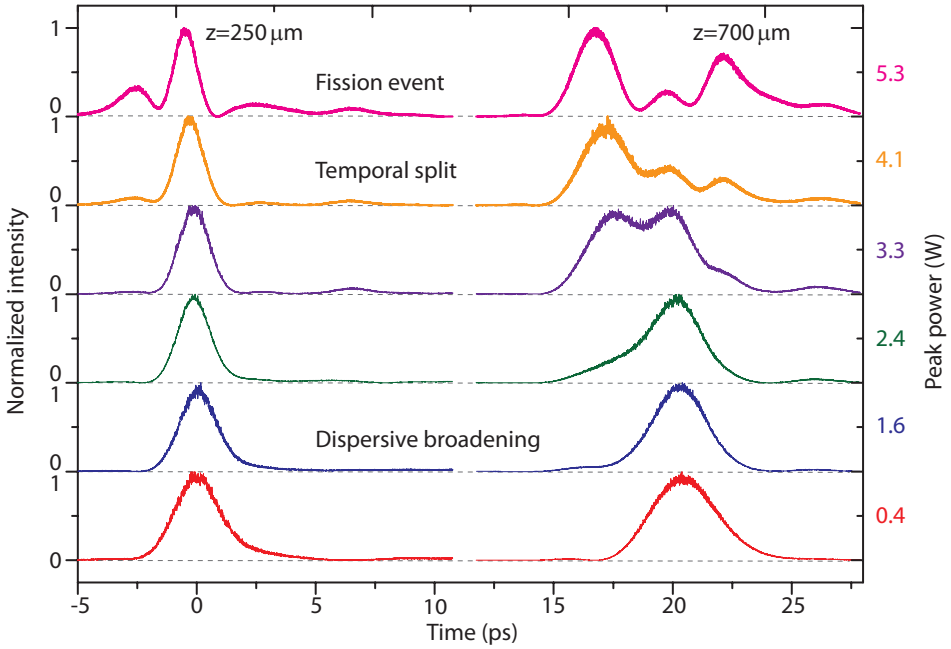

Figure 4.5: Experimental power study of the pulse envelope reshaping. Time-resolved near-field measurements at propagation distances of 250 µm *and* 700 µm *are shown for varying peak power. The curves for different peak powers are vertical shifted by an offset for clarity. At a propagation distance of* 250 µm *mainly a temporal compression of the pulse with increasing peak power can be seen. After a propagation of* 700 µm *the emergence of extra wave packets generated by the soliton fission becomes apparent. With increasing peak power two additional wave packets besides the main wave packet appear and increase in relative amplitude.*

Since, we are interested in the fission of a higher-order soliton we repeat the measurement at a peak power of 5.3 W. After a propagation distance of 250 µm we observe a pulse envelope, which consists of a main wave package that is temporally compressed to a FWHM of 1.08 ps, as expected for a higher-order soliton (see Fig. 4.4c). Further, there are extra wave packets emerging, one to longer and one to shorter times, which are the first indications of the soliton fission that we expect should have occurred before this point. At a propagation distance of 700 µm the features of a soliton fission are more pronounced, as can be seen in Fig. 4.4d. Since the amplitude of the central wave packet decays with propagation, the satellite pulses grow in relative amplitude, until they even overtake the former main peak in amplitude. Thus, the higher-order soliton has broken apart and the fission event has generated two additional wave packets. Further, a small fraction of the energy has remained in the original wave packet, which decays in amplitude due to dispersion, since its peak intensity is no longer enough to sustain a fundamental soliton.

We compare the cross-correlation near-field measurements with results from the model using the NLSE, shown as blue dashed lines in Fig. 4.4. In general, there is good qualitative agreement between the experimental and modeling results. For a peak power of 0.4 W the model also predicts only a symmetrical temporal broadening of the main wave packet. There is one discrepancy between the experiment and the calculation. The NLSE predicts the emergence of side shoulders at a propagation distance of 700 µm, which are not observed in the experimental results. The origin for this discrepancy is as yet unknown. When the peak power is increased to 5.3 W the NLSE results show the same features that we described for the experimental results. There is a temporal compression and emergence of extra wave packets at a propagation distance of 250 µm. Moreover, the model also reproduces the change in the relative amplitudes of the wave packets noticed in the experimental result after 700 µm. The qualitative agreement between the experiment and model confirms our interpretation that the observed features are caused by a fission event of a higher-order soliton. The event is experimentally found to occur before 250 µm, which is consistent with the calculated fission length of 166 µm.

To observe the transition from the linear regime, where the pulse only broadens temporally due to GVD, to the nonlinear regime, where a soliton fission event occurs, we also perform a power study. In detail, we measure

the temporal pulse envelope of 6 different peak powers ranging between 0.4 and 5.3 W after the pulse has propagated a distance of 250 and 700 µm. The results of this power study are presented in Fig. 4.5, where subsequent measurements are shifted vertically for better comparison. After a propagation distance of 250 µm we mainly observe the gradual temporal compression with increasing peak power. A peak power between 2.4 and 3.3 W is required for emergence of extra wave packets. This observation indicates that the soliton fission is caused by a nonlinear optical effect, which scales with intensity. At a propagation distance of 700 µm we see the gradual increase of the amplitude of the satellite pulses relative to the main wave packet with increasing peak power. This observation shows that more energy is transferred to the wave packets generated in the fission event when the intensity is higher. Further, there is an increasing separation in time visible between the different peaks with increasing peak power. Please note that a fourth wave packet is also visible in the measurements to longer times. We did not observe this wave packet in the model. The cause of the emergence of this satellite pulse is not understood yet.

4.5 Free carriers as the cause of the soliton fission

So far we have not discussed what physical effect causes the soliton fission. To answer this question we turn to the modeling. In the NLSE we can include or exclude physical effects as desired. GVD and SPM are always included. Potentially there are two effects in our waveguide which might cause a fission: TOD or free-carrier effects, where the free-carriers are generated by 3PA. PhCWs are usually highly dispersive structures and it has been shown that free carriers can have a significant influence on pulse propagation in semiconductor waveguides. In contrast, in optical fibers, where soliton is usually investigated, free-carrier effects are negligible, but Raman scattering, for example, is much more dominant. Raman scattering can be excluded in this case, because it requires ultrashort pulses in the femtosecond regime to be efficient [121], while we are working with picosecond long pulses.

In the case that we only include TOD, the NLSE calculation predicts that at a peak power of 5.3 W we generate a higher-order soliton which does not break apart, but shows a periodic evolution with propagation (see Fig. 4.6a). This result illustrates that the amount of higher-order dispersion

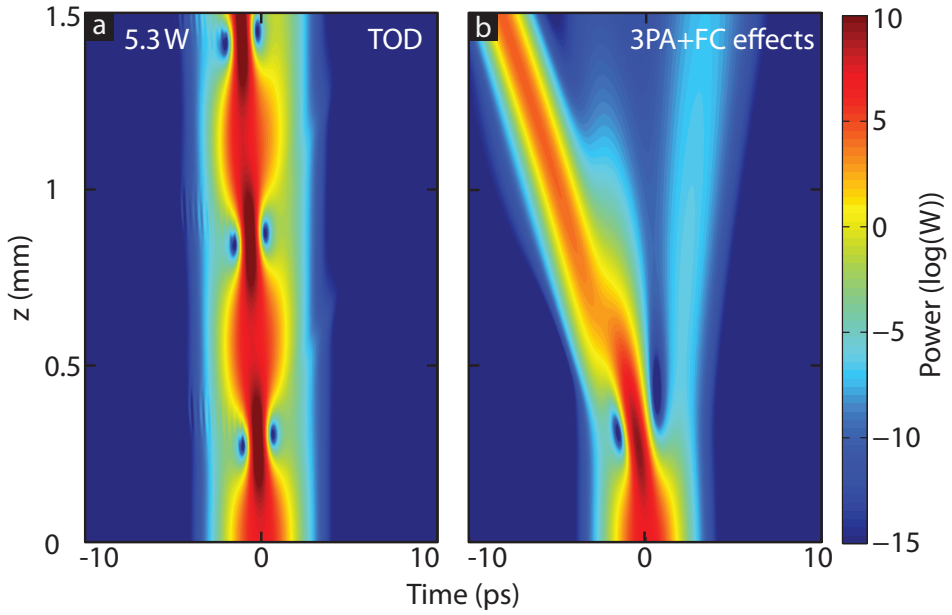

Figure 4.6: Modeling the perturbation of the propagation of a higher-order soliton. a) When TOD is included in the NLSE, with GVD and SPM, the soliton stays together and shows its characteristic periodic behavior with propagation distance. b) In contrast, by including free-carrier effects instead of TOD, the soliton breaks apart, showing that free-carrier effects cause the soliton fission.

is not strong enough to rip the soliton apart. This observation is consistent with our prior observation of the symmetric broadening of the pulse at low input powers.

In the case that we only include free-carrier effects, i.e., free-carrier absorption and free-carrier dispersion, we observe a fission of the higher-order soliton (see Fig. 4.6b). This proves that the free-carrier effects are actually the cause of the fission event. The result that free carriers, created by 3PA, are responsible for the soliton fission is consistent with the observation in the measurement that the fission event only happens above a certain threshold peak intensity, due to the higher nonlinear character of 3PA as compared to 2PA. This is the first time that it has been observed that free carriers can perturb the propagation of a higher-order soliton.

4.6 Temporal dynamics of the different wave packets

In soliton fission events observed in optical fibers it is common that the different emerging wave packets show different temporal dynamics, i.e., they exhibit a different group velocity [119]. Understanding the propagation behavior of the various pulses might enable better waveguide designs for improved supercontinuum generation. To investigate the behavior of the wave packets in our experiment we turn again to time-resolved near-field measurements, which allow the extraction of the group velocity of the various wave packets. Here, we change the laser wavelength to 1555 nm, where n_g, GVD and TOD coefficients have values of 17.3, $-2.6\,\mathrm{ps}^2/\mathrm{mm}$ and $-0.6\,\mathrm{ps}^3/\mathrm{mm}$, respectively. Although we have now changed the wavelength from 1553 nm, we expect to observe a similar evolution of the pulse with propagation distance and peak power as discussed above.

To extract the group velocities of the different wave packets, we measure several interference traces at five different propagation distances ranging from 300 to 1000 µm for peak powers ranging from 0.4 to 5.3 W. As first step, we investigate the group velocity of the main wave packet in the linear optical regime, i.e., at the lowest peak power. Three representative near-field measurements, which illustrate the shift in the temporal position of the collected wave packet with distance, are shown in Fig. 4.7a. We fit a straight line to the observed temporal position of the maximum amplitude of the wave packet over propagation distance to extract the group velocity and the group index of the wave packet, respectively (cf. Fig. 4.7b). This approach is only valid as long as the pulse does not reshape, which is the case here. It is found that the pulse propagates with a group index of 16.4, which fits nicely to the value of 17.3 expected from the calculated dispersion relation.

As discussed above, our model predicts a change of the group velocity of the two additional wave packets that are generated in the soliton fission event. In addition, we observed a shift of the temporal positions of the satellite pulses with increasing peak power in the experiment. To investigate these temporal dynamics of the various wave packets we make a detailed analysis of the time-resolved near-field microscopy measurement. By tracking the temporal position of the peaks in the measured temporal envelope at different propagation distances as function of peak power al-

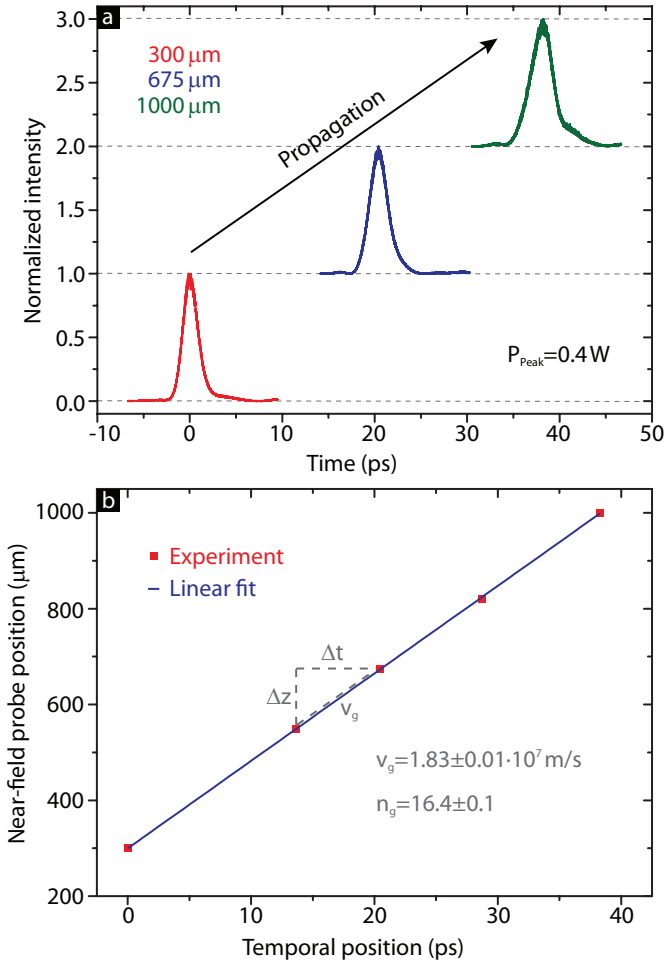

Figure 4.7: Extracting the group velocity of a wave packet from time-resolved near-field measurements. a) A series of near-field measurements at three different propagation distances along the waveguide at a peak power of 0.4 W. We observe that as the propagation distance increases, the pulse arrives at later times. b) Corresponding temporal shift of the wave packet with propagation distance. The slope of a straight line fit (blue line) is the group velocity and inversely proportional to the group index of the pulse, respectively.

lows the determination of a change in the group velocity. A negative time shift of the peak with increasing peak power denotes an acceleration, since it indicates that the wave arrives earlier at the same spatial point. Correspondingly, a positive time shift describes a deceleration. To relate the temporal position of a peak to a group velocity we have to assume negligible temporal reshaping, which is a valid assumption for each individual wave packet considering the low higher-order dispersion observed before. The model also predicted no drastic reshaping of the different pulses with propagation.

In the measurements we can observe up to four wave packets. To distinguish the wave packets we number them according to their appearance in time. The pulse appearing at the earliest point in time is called wave packet 1, the second appearing pulse is wave packet 2 and so on. These wave packets are not all always visible, since most of them are generated in the soliton fission event. Consequently, most of the wave packets require a certain peak power or propagation distance to show up in the measurement, except for wave packet 2, which represents the original pulse that undergoes the fission event. An example of two typical measured temporal envelopes is shown in Fig. 4.8a. Here, the near-field measurements are taken at a propagation distance of 1000 µm and for peak powers of 2.4 and 4.1 W, respectively. At this propagation distance and for this high peak power, we observe all four wave packets, which indeed feature a time shift with increasing peak power.

The time shifts of the four wave packets extracted from the series of near-field measurement are summarized in the Fig. 4.8b-e. Here, the zero point in time indicates for each wave packet the time where it can be observed for the first time. This does not need to happen at the lowest peak power or the shortest propagation distance, for example the first wave packet is not visible at a propagation distance of 300 µm.

For wave packet one and two a consistent negative time shift with increasing peak power and propagation distance can be observed. Moreover, the time shift is usually a nonlinear function of the peak power. In connection with the dispersion relation, this acceleration could be explained by a blueshift with propagation of the spectral density, as explained above.

The behavior of the third and the fourth wave packet is more complex. In general, it is hard to see a conclusive trend. The wave packets seem to shift to negative times at some propagation distances and to positive

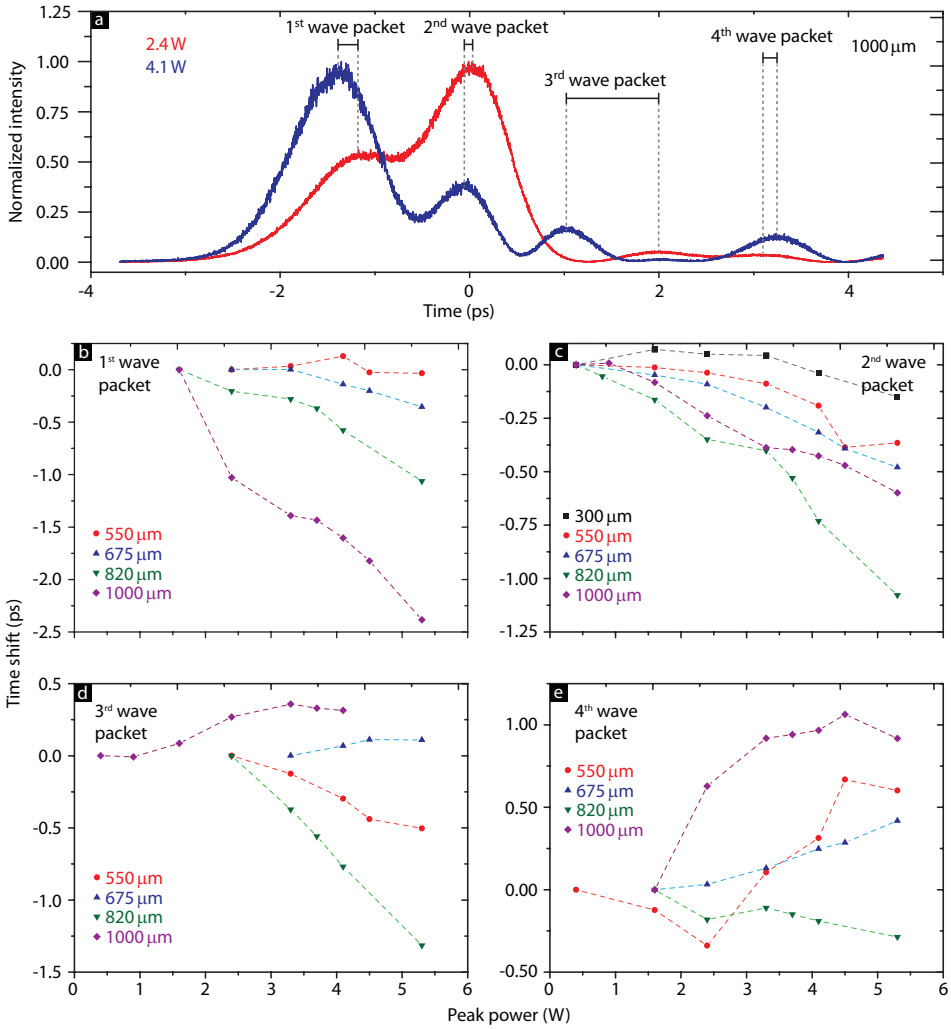

Figure 4.8: Observing acceleration or deceleration of wave packets in the near-field measurements. a) Two typical measurements at a propagation distance of 1000 µm *for a peak power of 2.4 (red line) and 4.1 W (blue line), respectively. Here, four wave packets are visible, which shift in time as the peak power increases. The time shift for the four different wave packets are shown in panels b)-e).*

times at others. This observation might be caused by the fact that here the time shifts are smaller than for the first and second wave packet and there is a larger uncertainty in extracting the position of the less pronounced peaks here. However, after a propagation distance of 1000 µm the third and fourth wave packet both show a slight shift to positive times, i.e., the waves are decelerated. This behavior can be explained by the assumption that these pulses consist of the spectral components, which redshift with propagation and peak power.

4.7 Conclusion

In conclusion, we have shown how it is possible to directly measure and visualize a soliton fission event as it happens inside a PhCW. Due to the strong dispersion and enhancement of nonlinear effects in this nanophotonic waveguide, we could investigate soliton propagation on a length scale of a few hundred microns, which is at least an order of magnitude shorter than what can be achieved in optical fibers. As a result, we were also able to observe a record short fission length of 166 µm, after which the higher-order soliton broke apart into several wave packets. Further, we proved that in the semiconductor waveguide, free-carriers are the major perturbation for soliton propagation and introduced therefore a new mechanism for soliton fission. Finally, we investigated the temporal dynamics of the different wave packets generated in the soliton fission. The results discussed in this chapter represent a step towards implementing an on-chip supercontinuum source by using nonlinear pulse propagation in a nanophotonic waveguide.

5

Ultrashort-pulse propagation on Au nanowires

ABSTRACT: In this chapter we explore the potential of plasmonic nanowires for ultrafast photonics by comparing the properties of the guided SPP to that of the mode guided in a silicon nanowire. For this purpose, we combine ultrafast near-field microscopy measurements of gold nanowires with mode simulations to study modal properties such as mode width, propagation length, fundamental mode cut-off, GVD, and TOD. Using this information we show that, for ultrashort-pulse propagation, plasmonic waveguides can outperform their dielectric counterparts. In particular, we demonstrate that the ohmic losses, which are unavoidable in the gold nanowire, cause less peak amplitude decay for ultrashort-pulse propagation than the high dispersion and the presence of a mode cut-off in a silicon nanowire.

5.1 Introduction

In the past several years guided plasmonic modes of metallic nanowires (NWs) have emerged as a promising basis for nanophotonic circuits [29]. Interestingly and in stark contrast to conventional dielectric waveguides, decreasing the geometric cross-section of the NWs results in an increased confinement of the plasmonic mode [37]. In addition, it has been predicted [41] and experimentally demonstrated[129] that as SPPs are confined, they also slow down. Such a slowdown is beneficial for applications in telecommunication, as it enhances light-matter interactions [130] allowing for elements with smaller footprints [31].

Currently, most photonic devices rely on dielectric waveguides, such as ridge or photonic crystal waveguides [86, 131, 132, 133, 134]. These dielectric structures do not suffer from the inherent ohmic losses found in plasmonic materials. Nevertheless, the guided mode of dielectric waveguides does experience geometrical dispersion in addition to the intrinsic material dispersion. In contrast, the dispersion of plasmonic structures is dominated by their material dispersion and it has been predicted that they can support the broad bandwidth necessary to exhibit sub-fs dynamics [135, 136]. In fact, high-harmonic generation has been observed when the localized plasmon modes of nanoantennas are driven by femtosecond pulses [137, 138, 139]. Further, excitation of metallic nanostructures with femtosecond lasers has enabled studies of their plasmonic resonances [140, 141].

Recent research has raised hopes that plasmonic waveguides might be a viable platform for ultrashort-pulse propagation. Not only have the dispersion relations of various plasmonic waveguides been calculated and measured [142, 143, 144], but pulse propagation on these structures has also been studied [145, 146, 147, 148]. From these, and other measurements, the group velocities of the different plasmonic modes have been determined [146, 149], and even used for spatio-temporal control experiments [150, 151]. However, while many of the properties of plasmonic waveguides are known, it remains unclear exactly how ultrashort pulses behave and reshape as they propagate on such structures. More importantly, it remains to be shown whether there are regimes of pulse propagation where plasmonic waveguides can outperform their more established dielectric counterparts.

In this chapter we explore ultrashort-pulse propagation on plasmonic NWs to demonstrate their potential for ultrafast photonics on subwavelength dimensions. We use a series of near-field measurements in con-

junction with finite-element method (FEM) calculations to investigate the properties of the plasmonic modes on Au NWs. We then compare these properties of the plasmonic modes to those found on dielectric waveguides. We show that while the plasmonic waveguides outperform their dielectric counterparts in the achievable spatial confinement, the plasmonic mode suffers from a finite propagation length and a lower group index. We demonstrate, however, that the SPP guided in the Au NW experiences much less dispersion than light guided in a Si NW. In particular, for ultrashort-pulse propagation the decrease in peak intensity due to temporal pulse reshaping in a dielectric waveguide can be stronger than the decrease due to the ohmic losses experienced in a plasmonic waveguide.

5.2 Sample and setup

We study ultrashort-pulse propagation on plasmonic waveguides by experimentally and theoretically characterizing the properties of lithographically fabricated Au NWs (Fig. 5.1a). We fix the Au thickness to 50 nm and vary the width between 40 and 240 nm (Fig. 5.1b), where the maximum width is chosen so that our NW is not leaky over the whole bandwidth of the laser pulses. This way the geometrically dependent properties of the guided modes can be determined. In both the experiments, which are carried out with phase- and time-resolved near-field microscopy [97] (see section 2.5), and the FEM simulations (using the COMSOL multiphysics software package), we study the propagation of telecom (centered at 1550 nm) wavelength, femtosecond pulses. Experimentally, we excite SPPs by illuminating a hole array, whose periodicity has been carefully selected to resonantly couple free-space radiation to plasmons on the Au-glass interface and not on the Au-air interface [35]. These interface SPPs are then adiabatically transformed into NW plasmons with a taper [37]. In these measurements we use a 250 nm aperture probe, which delivers a good trade-off between the signal-to-noise ratio and the optical resolution. For the simulations, the dispersive material refractive index of Au is taken from the literature [152], and the refractive index of the BK7 glass substrate (of our samples) is fixed at 1.5.

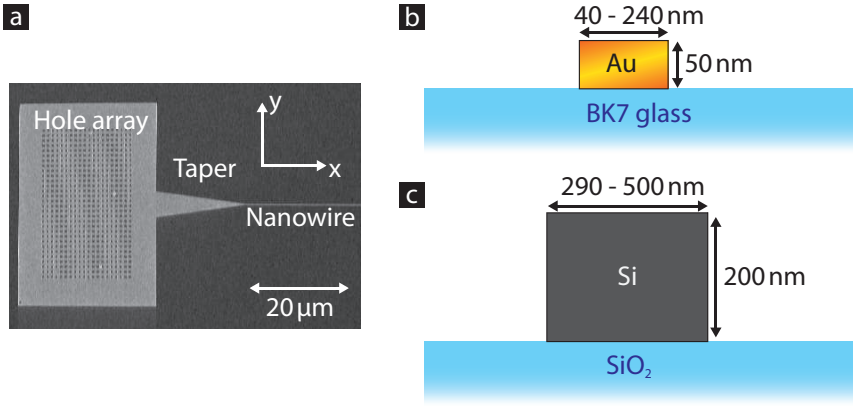

Figure 5.1: Sample geometry. a) Micrograph of a typical plasmonic structure consisting of a hole array, a taper, and a NW. The hole array and the taper are required to efficiently excite the mode on the Au NW with free-space illumination. Schematic of the cross section of b) a Au NW and c) a Si NW showing the dimensions of the waveguides.

5.3 Spatial confinement of the nanowires

One of the fundamental advantages of plasmonic waveguides, over dielectrics, is that they are expected to strongly confine light to the waveguiding region. Consequently, we begin by investigating the spatial confinement of the plasmonic modes. We measure the in-plane field amplitude and phase of the guided SPPs in the NW, using CW illumination. We Fourier filter [115] our signal and create the in-plane intensity maps of the SPPs, an example of which is shown in Fig. 5.2a for a 240 nm wide NW. Here, we see how a SPP propagating from left to right is funneled from the taper into the NW (starting around $y = 6\,\mu m$). For a wide taper width, an optical signal can only be observed at the edges of the Au layer. As the taper width narrows, the electric field of the SPP "wraps around" the NW, and consequently we can detect a signal above the NW. In fact, we measure the highest intensity at the beginning of the NW, which then decays with propagation due to the ohmic losses of the SPP.

We can quantify the spatial confinement of the mode by averaging intensity cross-cuts in the x-direction along the NW and fitting a Gaussian function to this averaged cross-cut. Since there might be small variations

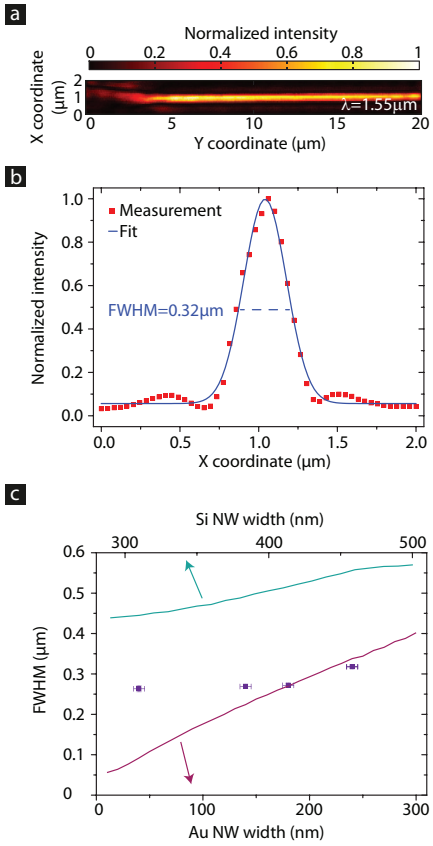

Figure 5.2: Mode width of the NWs at a wavelength of 1.55 µm. *a) Measured spatial intensity map of a SPP propagating on a 240 nm wide Au NW with CW laser excitation. The funneling of the SPP from the taper left of the NW is observed between 0 and* 4 µm. *b) Cross-cut in the x-direction after normalizing and averaging the NW intensity profile of a) and a corresponding Gaussian fit. The SPP guided by the Au NW has a mode width of* 0.32 µm. *c) Dependence of the mode width on the NW width for the Au NW (measurements shown by symbols and simulations by the purple curve) and the Si NW (cyan curve). A decrease of the mode width with decreasing NW width can be observed. The plasmonic structure exhibits a stronger spatial confinement than the dielectric waveguide.*

between the cross-cuts of the intensity at different propagation distances, we do not take a single line as representative for the whole NW. Instead, we average along the y-direction over a number of cross-cuts. Furthermore, we confine the averaging procedure to intensity cross-cuts along the actual NW, i.e., from y = 6 µm to y = 20 µm in Fig. 5.2a. In detail, we sum the measured two-dimensional intensity distribution along the y-direction over the NW, divide by the number of cross-cuts and normalize this averaged quantity. Using this procedure the averaged intensity cross-cut of the optical signal on the NW shown in Fig. 5.2b is calculated. We repeat this fitting procedure for different NW widths to determine the dependence of the mode width on the NW cross-section. The results of these measurements are depicted as purple squares in Fig. 5.2c. As expected, we observe that the mode width decreases, and hence the confinement increases, as the NW cross-section decreases. Note that the horizontal error bars (±5 nm) are due to uncertainties in the determination of the NW width, while our uncertainty in the FWHM (∼ 10 nm) is too small to be visible in Fig. 5.2c.

This trend of increasing confinement for smaller NWs is reproduced by the simulations (solid purple curve in Fig. 5.2c). There is, however, a deviation between the simulated and measured mode widths, particularly for smaller NWs. This discrepancy is attributed to the finite aperture size of the near-field probe used in the experiment, which limits the smallest measurable FWHM values. Since we use a probe with a 250 nm aperture, for small NW widths the measured mode width represents the aperture size, while for larger NW widths we measure values close to the actual lateral field spread. The nearly monotonic decrease of the mode width with NW dimensions observed in the simulations confirms that the SPP can be guided on arbitrary small plasmonic waveguides.

Having established how the plasmonic NWs confine light, we turn to the dielectric waveguides and look for a geometry where similar confinement occurs. Specifically, we want to compare the plasmonic NW to an ubiquitous dielectric NW, the Si NW [11, 131, 153, 102, 154, 155, 156] (Fig. 5.1c). We fix the height of the Si NW to 200 nm and allow the width to range between 290 and 500 nm. The smallest width of 290 nm is chosen since smaller Si NWs no longer support a guided mode [157]. The dispersive refractive indices of the Si core and the silica substrate are taken from the literature [158, 159]. Since these dielectric waveguides have been extensively studied [160, 161, 162], we limit ourselves to simulations of their

properties, investigating only the Au NWs experimentally.

The simulated mode width of the Si NWs, which we show with a cyan curve in Fig 5.2c, qualitatively behaves in much the same way as the mode width of the Au NWs: the width of the mode decreases with the NW width. There are, however, a few important differences to note between the behavior of the dielectric and plasmonic waveguides. First, the mode of the Si NW is always wider than that of the Au NW. Further, whereas the mode width for the plasmonic waveguide is, in principle, not restricted to a minimum value, we find a minimum mode width for the dielectric waveguide of $\sim 430\,\mathrm{nm}$. This suggests that, if we want to compare plasmonic and dielectric waveguides with similar light confinement, we should use the narrowest Si NW available. Consequently, we will mainly consider a 300 nm wide Si NW hereafter, although we note that the mode width of this NW is still 2.0 and 1.1 times larger than that of a 140 or 300 nm Au NW, respectively.

5.4 Single-mode operation of the NWs

There are two conditions which must be fulfilled if the fundamental mode of the NW is to be useful for applications. First, the waveguide should only support one mode, as the presence of higher-order modes would lead to mode mixing in a realistic device due to imperfections. Second, this fundamental mode should be truly guided and not leaking into the surrounding. The effective mode index $n_{eff} = k(\omega)/k_0$ contains the necessary information to study the number of guided modes available in a structure. Here, $k(\omega)$ and k_0 are the wavevectors of the mode guided in the NW and for light propagating in vacuum, respectively. In essence, the number of branches, where $\mathrm{Re}(n_{eff})$ is larger than the refractive indices of the surrounding, will specify the number of modes guided in the waveguide. If, however, $\mathrm{Re}(n_{eff})$ is smaller than the refractive index of the adjacent medium light will leak into that material. Therefore, we investigate the effective mode index, which is extracted from FEM simulations, to determine the regime where the NWs support only one mode.

The two parameters which determine the number of guided modes and their properties are the NW geometry and the excitation wavelength. First, we investigate the mode characteristics when the NW width is varied while the wavelength is fixed to $1.55\,\mu\mathrm{m}$. The corresponding simulation results

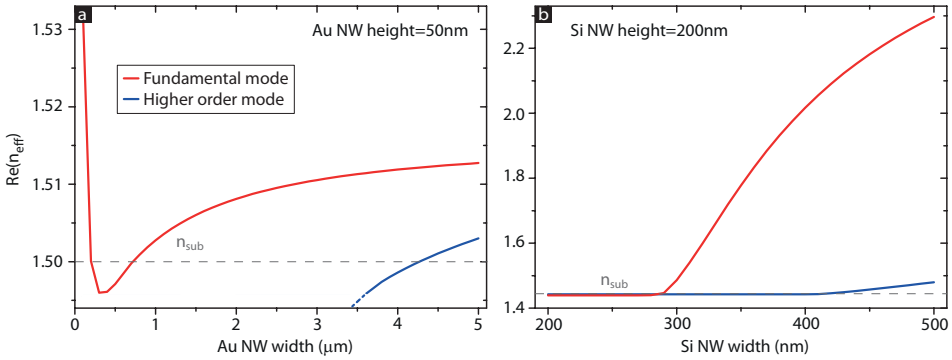

Figure 5.3: Dependence of the real part of the effective mode index on the NW width at a wavelength of 1.55 µm. *The first two modes are shown for a) a Au NW with a height of 50 nm and b) a Si NW with a height of 200 nm. The dashed gray line indicates the refractive index of the substrate* n_{sub}. *If* n_{eff} *lies above* n_{sub} *the mode is guided, otherwise it leaks into the substrate.*

are shown in Fig. 5.3. The fundamental mode of the Au NW is guided for all cross-sections. Its real part of the effective mode index first drops with narrowing width, even leaking into the substrate for NW widths between 0.2 and 0.8 µm, before diverging for widths smaller than 0.2 µm. In contrast, the next higher order mode features a cut-off NW width, i.e., this mode becomes leaky for width smaller than 3.5 µm. This means that the plasmonic waveguide features only one guided mode for nearly all narrower NW geometries (except for the small regime where the fundamental mode becomes leaky).

In contrast, the modes in the dielectric waveguide show a different characteristic. The real part of the effective mode index of the fundamental mode only drops with narrowing the NW width until the mode becomes leaky at widths below 280 nm (cf. Fig. 5.3b). Further, a second-order guided mode appears at a NW width of 420 nm. Consequently, the Si NW features only one guided mode for NW width between 280 and 420 nm. These observations show that it is more challenging to design a dielectric waveguide that supports only one mode than a plasmonic one.

Next, we determine the wavelength dependency of the guided modes for fixed NW cross-sections. The calculation results for five geometries, three plasmonic and two dielectric waveguides, are presented in Fig. 5.4. In

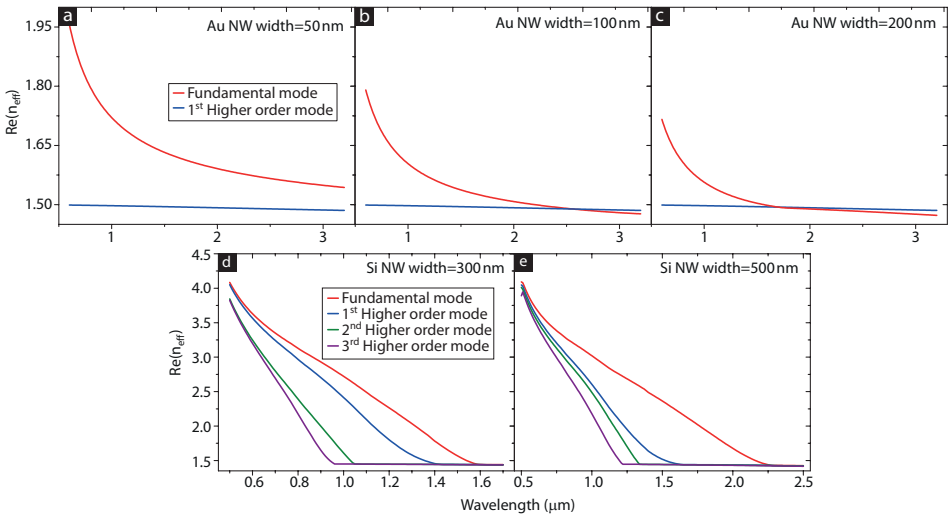

Figure 5.4: Dependence of the real part of the effective mode index on the wavelength. The first four modes are shown for a Au NW with a height of 50 nm and a width of a) 50 nm, b) 100 nm, c) 200 nm and a Si NW with a height of 200 nm and a width of d) 300 nm e) 500 nm.

all Au NWs, the real part of the effective mode index of the fundamental mode increases when the wavelength is decreased, until it diverges around a wavelength of 0.6 µm. In addition, $\mathrm{Re}(n_{\mathrm{eff}})$ increases with decreasing NW width (cf. Fig. 5.3). As a consequence, the fundamental mode is always guided for the narrowest width. In contrast, for the 200 nm wide NW, the mode becomes leaky at $\lambda \sim 1.6\,\mu\mathrm{m}$. Thus, the wider the Au NW, the smaller the spectral regime where there is only one guided mode, which does not leak into the substrate.

The Si NW again shows a different behavior. First of all, for all NW widths more modes are supported than for the plasmonic structure. Here, we will limit ourselves to the first four modes. For the smallest Si NW width, the fundamental mode is close to its cut-off wavelength λ_{cut}, which is at 1.6 µm, where it starts to leak into the substrate. In addition, for a wavelength shorter than 1.4 µm, the waveguide becomes multi-mode. The second investigated Si NW, which has a width of 500 nm, features a fundamental mode with a redshifted cut-off of 2.25 µm. However, the cut-off wavelengths of the higher order modes are also redshifted. This means that

Platform	NW width	λ_{cut} 1stmode	λ_{cut} 2ndmode	Bandwidth
Au	50 nm	-	-	$>$ 2600 nm
Au	100 nm	2750 nm	-	$>$ 2150 nm
Au	200 nm	1600 nm	-	$>$ 1000 nm
Si	300 nm	1600 nm	1400 nm	200 nm
Si	500 nm	2250 nm	1600 nm	650 nm

Table 5.1: Useable wavelength region for single-mode operation for the different NW geometries.

for this Si NW, the second mode is already guided at 1.6 µm.

In the case that it is required to work in a spectral region where the NW possesses only one guided mode, which is not leaky, the narrow Au NWs offers the largest useable bandwidth. This can be seen in table 5.1 where this bandwidth is given for the different NWs. In general, the plasmonic structure offers a larger operational bandwidth than the dielectric ones. The bandwidth in the Au NW can be increased by narrowing the NW width. The opposite holds for the Si NW. Additionally, it is important to note that the center wavelength of the single-mode bandwidth can change with the NW geometry. For the Si NW this means that the wider geometry is already multi-mode at a wavelength of 1.55 µm. That is, in the case of the high confinement dielectric waveguide, it is necessary to work close to λ_{cut} of the fundamental mode which limits the useable bandwidth for pulse propagation.

5.5 Dispersion properties

Having found that the plasmonic and dielectric NWs can confine light to similar dimensions, we set out to determine the differences and similarities of pulse propagation in these structures. An important quantity that describes the evolution of a propagating pulse in a waveguide is the dispersion relation k(ω) [8]. As discussed in section 1.2.2, the most important dispersion properties of the waveguide are quantified by the GVD and the TOD, respectively, since they specify the strongest contributions to the temporal pulse reshaping during propagation. In Fig. 5.5 both quantities, calculated from the simulated dispersion relation for several NW geometries, are presented as a function of wavelength.

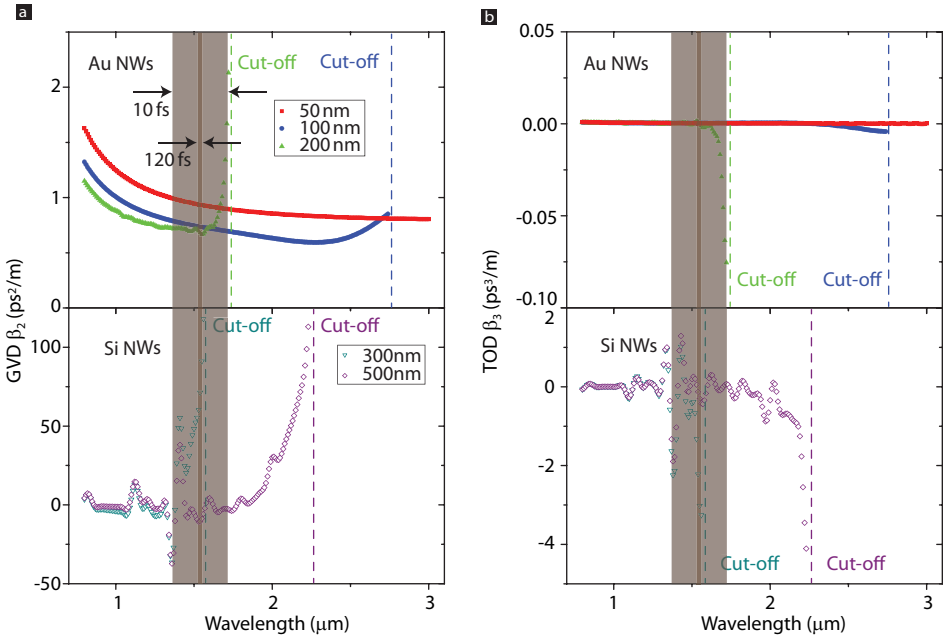

Figure 5.5: Dispersion properties of Au and Si NWs. a) The GVD coefficient as a function of wavelength. b) The TOD coefficient as a function of wavelength. Top panel: Au NWs. Bottom panel: Si NWs. The plasmonic waveguides feature two orders of magnitude smaller GVD and TOD coefficients than do the Si NWs. Dashed lines indicate the cut-off wavelengths of the correspondent modes. The shaded areas represent the spectral region populated by the FWHM bandwidth of a 10 and a 120 fs pulse, respectively. The fringes, which can be seen on top of the GVD and TOD curves of the Si NWs, are numerical artifacts from the FEM simulation and do not have a physical origin.

In general, Fig. 5.5 shows how changing the geometry affects the dispersion of the plasmonic and dielectric waveguides. The amplitude of the dispersion coefficients is increased when the NW sizes are decreased, at all wavelengths. In the case of the Au NWs, the GVD and TOD increase when the NW width is narrowed. In addition, there is a cut-off, i.e., a wavelength above which a guided mode becomes leaky, for the two wider Au NWs. In contrast, for the dielectric waveguides the dispersion curves shift to shorter wavelengths when the NW width is decreased. As a consequence, the spectral regime of high dispersion, close to the cut-off, is blueshifted. For example, the cut-off shifts from 2.25 to 1.6 µm when the NW width is decreased from 500 to 300 nm. Comparing the magnitude of the GVD and TOD for Au and Si NWs it is immediately obvious that the dispersion coefficients for the Si NWs are an order of magnitude larger than for their plasmonic counterparts. This huge difference in the magnitude of GVD and TOD shows that the dielectric waveguides are intrinsically more dispersive than the Au NWs, especially when operated close to the cut-off of the guided mode, where the dispersion coefficients diverge. Note that the fringes on top of the GVD and TOD curves of the Si NW are numerical artifacts from the FEM simulations and do not have a physical origin.

It is common to define a dispersion length L_D to quantify the distance after which dispersion significantly reshapes the pulse envelope. This means that dispersion is typically neglected for propagation distances shorter than L_D and has to be taken into account for longer distances. We chose to define L_D as the distance where the amplitude of the Gaussian pulse is broadened by $\sqrt{2}$ [8]:

$$T(z = L_D) = \sqrt{2}T_0, \tag{5.1}$$

where T_0 is the starting FWHM value of the Fourier-transform limited pulse.

It is possible to calculate the dispersion length analytically, if only GVD or TOD is taken into account [8]. However, since we investigate ultrashort-pulse propagation it is in general not valid to neglect higher-order terms. Thus, we use a different approach to extract the dispersion length. We employ a semi-analytic linear model based on the NLSE (see section 1.2.3 for more information) to calculate the temporal evolution of the pulse envelope, and hence its width, with propagation distance. Specifically, we solve the one-dimensional wave equation in the spectral domain[8]:

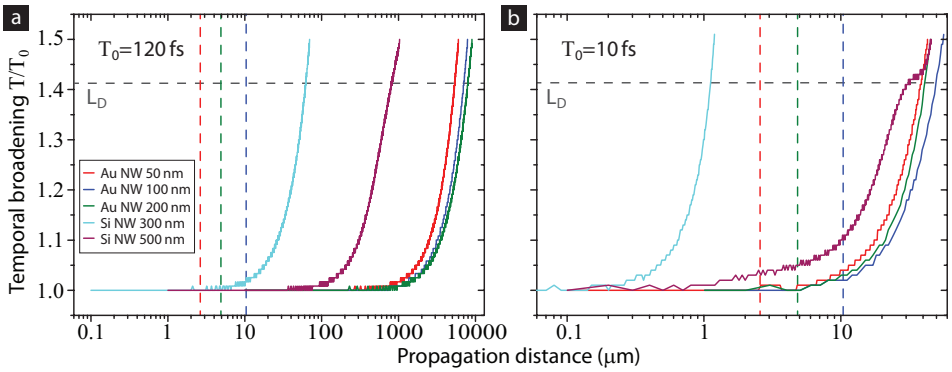

Figure 5.6: Calculated evolution of the temporal pulse width with propagation distance for a starting FWHM of a) 120 fs and b) 10 fs. Vertical dashed lines show the propagation distances after which the intensity of the pulse in the correspondent Au NW is decayed by 50 %. The intersection of the horizontal dashed gray line with the temporal pulse width marks $\mathrm{L_D}$.

$$\frac{\partial \hat{\mathrm{A}}(\mathrm{z},\omega)}{\partial \mathrm{z}} \;=\; \mathrm{iK}(\omega-\omega_0)\hat{\mathrm{A}}(\mathrm{z},\omega), \tag{5.2}$$

where $\hat{\mathrm{A}}(\mathrm{z},\omega)$ and $\mathrm{K}(\omega)$ are the spectral density of the slowly-varying pulse envelope and the frequency-dependent complex wavevector, respectively. This equation takes the linear absorption and dispersion that occur during pulse propagation into account. The solution to this equation is:

$$\hat{\mathrm{A}}(\mathrm{z},\omega) \;=\; \hat{\mathrm{A}}(\mathrm{z}=0,\omega)\cdot\exp[(-\frac{1}{2\mathrm{l}_{\mathrm{prop}}(\omega-\omega_0)} \;+\; \mathrm{ik}(\omega-\omega_0))\cdot\mathrm{z}]. \tag{5.3}$$

Here, knowledge of the dispersion relation $\mathrm{k}(\omega)$ and the propagation length $\mathrm{l}_{\mathrm{prop}}(\omega)$ for the intensity (as defined in Eq. (1.18)), which are determined with COMSOL, is required.

Figure 5.6 shows how the temporal pulse width broadens with propagation distance, for the different NW geometries. The left graph depicts the calculation result for a starting pulse width of $\mathrm{T_0} = 120\,\mathrm{fs}$. The curves for all geometries monotonically increase with propagation distance representing a temporal broadening of the pulse with propagation. This illustrates

Platform	NW width	L_D for $T_0 = 120\,\mathrm{fs}$	L_D for $T_0 = 10\,\mathrm{fs}$	l_{prop}
Au	50 nm	5.4 mm	38.0 µm	3.9 µm
Au	100 nm	7.0 mm	49.5 µm	7.2 µm
Au	200 nm	7.9 mm	41.4 µm	15.4 µm
Si	300 nm	62.2 µm	1.1 µm	∞
Si	500 nm	0.8 mm	29.7 µm	∞

Table 5.2: Calculated dispersion length for the different NW geometries. For comparison also the propagation length of the fundamental mode is given.

the fact that a Fourier transform-limited pulse only broadens due to dispersion, as long as nonlinear effects are negligible. The 300 nm wide Si NW features the steepest slope and therefore shows the shortest dispersion length (represented by the crossing point of the horizontally dashed line) of only 62.2 µm. The wider dielectric waveguide has an order of magnitude longer L_D. The Au NWs show, as mentioned above, the least dispersion and feature therefore the longest dispersion lengths, i.e., in the millimeter regime (exact numbers can be found in table 5.2).

Note, however, that the discussion so far did not take into account the ohmic losses which prevent the propagation for the SPPs of a signal over long distances. To illustrate the effect of the finite propagation length vertically dashed lines are included in Fig. 5.6 which represent the propagation distance after which the pulse intensity has decayed by 50 %. The absorption limits the feasible propagation distance on the plasmonic NWs to a few microns, whereas the dispersion length of all geometries for a pulse length of $T_0 = 120\,\mathrm{fs}$ is significantly longer.

The temporal broadening of pulses does not depend only on the amplitude of the dispersion coefficients, but also on the bandwidth of the pulse. It therefore remains to be seen how broad bandwidth pulses evolve as they propagate on Au and Si NWs. Consequently, we investigate the propagation of 10 fs pulses, which have a spectral bandwidth of 330 nm as compared to the 28 nm bandwidth of the 120 fs pulses. We note that 10 fs pulses, at 1550 nm, span only 2 optical cycles and are therefore among the shortest possible pulses at this wavelength. The right graph of Fig. 5.6 presents the temporal broadening for a pulse width of $T_0 = 10\,\mathrm{fs}$ propagating on the various NW geometries. In general, the same characteristics as before are

visible (i.e. the pulse monotonically broadens with propagation) but on a much shorter length scale. This comes from the fact that dispersion scales with the bandwidth, which is 12× larger for the shorter pulse. The 300 nm wide Si NW now features a dispersion length of only $\sim 1\,\mu m$, and the other geometries show an order of magnitude longer dispersion length. This reduced L_D suggests that a 10 fs pulse propagating a few microns should experience severe reshaping in the narrow dielectric waveguide, but not in the other geometries.

The data presented in Fig. 5.6 can also be used to investigate which process, dispersion or linear absorption, dominates the peak intensity decay. The mode propagating in the Si NWs experiences, in the ideal case, no loss and thus $l_{prop} = \infty$. Consequently, temporal reshaping due to dispersion is the sole cause for a decay in peak intensity. For the Au NWs the opposite is true. Here, the propagation length is much shorter than the dispersion length. Hence, the peak intensity decay is dominated by the linear losses in the plasmonic waveguides.

5.6 Results for pulse propagation

To experimentally investigate ultrashort-pulse propagation and to confirm if the superior dispersion properties of the plasmonic NWs are observable in experiment, we perform time-resolved measurements on the Au NWs using 120 fs long pulses. With our near-field microscope [163] we collect field transients at different positions along the plasmonic waveguide. Figure 5.7a depicts a typical measurement on a 140 nm wide Au NW of the temporal evolution of a pulse during propagation. Here, we positioned the near-field probed at four different propagation distances in the first 10 µm along the plasmonic structure and scanned the optical delay line to extract the temporal pulse envelope at these locations. In general, a Gaussian wave packet (FWHM of 120 fs) is observed, which decays in intensity and moves in time, as the propagation distance increases. When moving 9.6 µm along the Au NW, the intensity decreases by 85 % and the wave packet shifts by 60 fs.

To understand the temporal evolution of the pulse envelope, we compare the measurement to the result of the semi-analytical calculation of the pulse propagation (thin curves) using Eq. (5.3). There is good agreement between the experiment and the modeling (thick and thin curves in Fig. 5.7a). The

temporal movement of the wave packet is well reproduced, and only a small discrepancy in the intensity decay is observed. The experiment shows a slightly faster decay than the calculation.

We use the time-resolved near-field measurements to quantify both the losses and the speed at which a pulse propagates along the NW. The intensity decay with propagation is reproduced well by an exponential fit to the envelope amplitude, which yields the propagation length (l_{prop}). The increase in arrival time contains information about the group delay and can be used to extract the group velocity (v_g) and the group index ($n_g = c/v_g$), respectively, provided that no significant reshaping of the pulse envelope occurs (cf. inset in Fig. 5.7a).

The propagation loss, in the plasmonic NW, is mainly attributed to ohmic losses. Since the mode properties, such as the loss, are dependent on the width of the NW, we again investigate different NW geometries. Figure 5.7b summarizes the extracted propagation length of several temporal near-field measurements. In this figure, each symbol is the average l_{prop} from each series of measurements, while the error bars are given by the variance of those measurements. Indeed, we observe that the propagation length increases with increasing NW dimensions, as less field is confined to the metal (see insets of the modal field profiles in Fig. 5.7b). These observations are in good agreement with our simulations, although the measured propagation lengths are slightly smaller than the simulated values, indicative of an additional loss channel such as scattering from imperfections, which is not taken into account in the FEM simulation. Further, the measurements and simulations diverge for the largest NWs (width of $\sim 240\,\mathrm{nm}$). Although such a deviation has been previously observed [37], its exact cause remains unclear. It is, however, likely that leakage radiation losses into the substrate, which are known to occur for wider NWs, play a role.

We now turn to the speed at which the pulses propagate through the waveguides, which can be characterized by the group index of the mode. This parameter can be extracted by fitting a straight line to the linear time shift with propagation distance observed for the pulse in the experiment (cf. inset in Fig. 5.7a). Figure 5.7c shows a comparison of the measured and simulated group index for Au NWs of different widths, where the values and vertical error bars are again extracted from a statistical analysis of several measurements on each NW. In general, we observe the expected trend that smaller Au NW widths lead to slower SPPs [41, 146], with

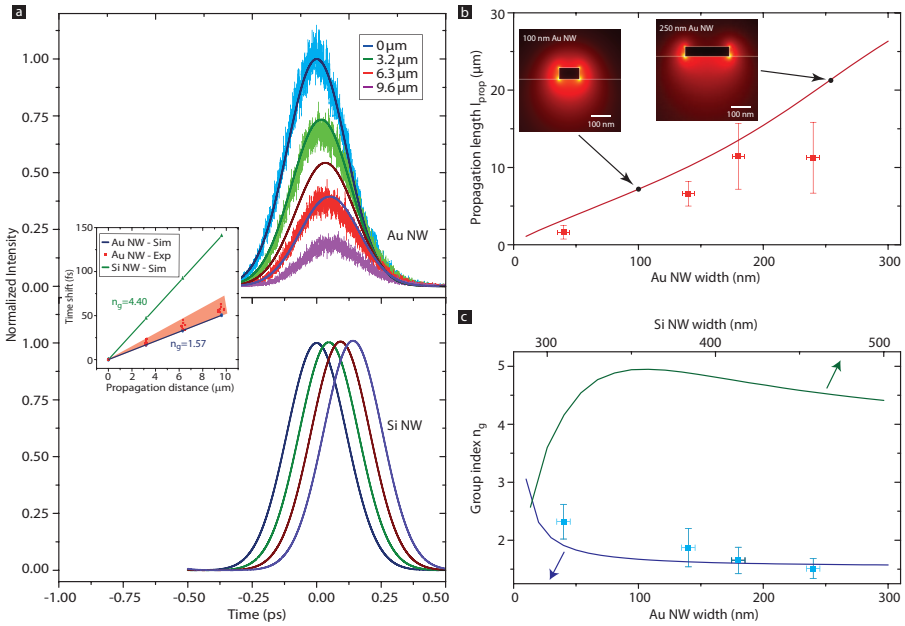

Figure 5.7: Temporal dynamics of a 120 fs pulse propagating in Au and Si NWs. a) Top panel: A comparison between a typical measurement series (thick curves) at different locations along a Au NW (width=140 nm) and a semi-analytical calculation of the pulse propagation (thin curves). The inset shows the arrival time with propagation and gives the group indices. Bottom panel: An analytical calculation of pulse propagation inside a Si NW (width=300 nm). The curves are normalized to the maximum intensity at a propagation distance of 0 µm. *Measured (squares) and simulated (curve) dependence of b) the propagation length and c) the group index on the NW width. Note that, at 1550 nm, the Si NW is ideally lossless and hence has a* $l_{prop} = \infty$. *The insets in b) show the electric field distribution of the mode guided along a 100 nm and a 250 nm wide Au NW, respectively.*

excellent agreement between experiments and simulations. The highest n_g value of 2.32 is measured for the narrowest width of 40 nm, and the simulation shows that this trend continues even further with decreasing NW width. These results show that there is a trade-off to be made in plasmonic waveguides: either there is a large slowdown combined with a huge spatial confinement and high losses, or less slowdown is achieved with a smaller confinement but also fewer losses.

Next, we compare the calculated propagation of a 120 fs pulse on Si NWs with our observations for the plasmonic structures. From the FEM simulations we again extract l_{prop} and n_g for the different NW widths, as was done for the Au NWs. In fact, at 1550 nm, Si NWs that support a guided mode are, ideally, lossless, and hence $l_{prop} = \infty$ for all widths. In contrast, n_g shows a rich width dependence. First, the group index increases with increasing NW width until it reaches a maximum of ~ 4.95 for a width of ~ 360 nm. Increasing the NW width further causes the group index to decrease again. Additionally, the mode guided in the Si NW is nearly always two- to three-times slower than an SPP propagating in a Au NW. This situation changes only for extremely small Au NW cross-sections.

As with plasmonic NWs, we can use the results of our simulations of the Si NW modes to semi-analytically calculate how 120 fs pulses would propagate on these structures. In the bottom panel of Fig. 5.7a we show the results of such a calculation, in this case for a 300 nm wide NW. In contrast to the plasmonic structure (top panel), we observe that, in the Si NW, the pulses both propagate more slowly and experience no loss. That is, other than a slightly weaker confinement, the Si NW appears to outperform the Au NW when 120 fs long pulses are considered.

In our measurements of the 120 fs pulses propagation on the Au NWs (Fig. 5.7a) we observe no reshaping of the pulse envelope. This suggests that within the 30 nm bandwidth of the pulse spectrum, dispersion is negligible. Likewise, our semi-analytic modeling of pulse propagation in the Si NWs, which uses the dispersion relation determined by simulations, shows that for this 30 nm bandwidth, dispersion is also negligible. These observations support the conclusion made from the dispersion length calculations above. For a pulse duration of 120 fs, all geometries feature a dispersion length that is much longer than 10 µm. Consequently, no temporal reshaping is visible.

We now turn to investigate the temporal evolution of the 10 fs pulses. As can be seen in Fig. 5.5, for the broad range of wavelengths contained within

these short pulses, the dispersion relation is far from flat. The dispersion length of these short pulses propagating on the narrow Si NW is shorter than 10 µm, whereas it is still several tens of microns long for the other NW geometries. Hence, temporal reshaping due to dispersion should be visible in the 300 nm wide dielectric waveguide, whereas the shape of the envelope should remain unchanged for the other NWs.

Figure 5.8 presents the results of the semi-analytical calculations performed for a pulse duration of 10 fs. It is obvious that the pulse envelope does not reshape while propagating through the plasmonic waveguides. Only the amplitude of the pulse drops due to the ohmic losses. In contrast, there is significant reshaping visible in the case of the 300 nm wide Si NW. Note that this reshaping is not caused by a nonlinear effect, in contrast to what is discussed in chapter 4. In the case of a 10 fs pulse propagating in the narrow Si NW, the Gaussian wave packet collapses into two peaks, which propagate with different group velocities and therefore separate in time with increasing propagation distance. However, when the pulse propagates in the 500 nm wide Si NW it does not show temporal reshape.

We now want to investigate which effects cause the temporal reshaping of the pulse in the narrow Si NW, which is illustrated in Fig. 5.9. As mentioned above, the pulse, which is Gaussian shaped at the start, splits into two wave packets that travel with different group velocities. The faster wave packet needs 50 fs to propagate 9.6 µm, which corresponds to a velocity of the peak of c/1.56. In contrast, the slower wave packet requires a time of 160 fs to travel the same distance. Consequently, in this second pulse the peak propagates with a velocity of c/5. The fact that the peaks of these two wave packets show such different velocities, illustrates that they are comprised of different spectral components. The fast pulse is built up by the part of the spectral density which covers the spectral region where the mode is leaky and the group index is close to the refractive index of glass. The remaining part of the spectral density is contained in the slow pulse. Thus, one reason for the temporal reshaping is the cut-off, which creates the two wave packets that propagate with completely different group velocity.

However, the splitting of the pulse into two wave packets is not the only feature visible in the evolution of the envelope. Additionally, the slow wave packet broadens temporally and develops a tail to shorter times. The FHWM of the pulse increases from 10 fs to 18 fs after propagating 9.6 µm.

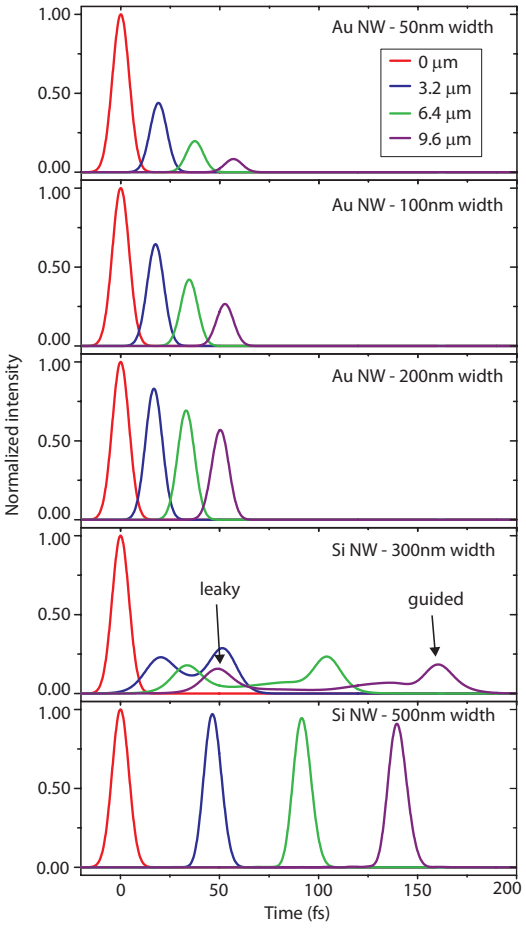

Figure 5.8: Propagation of a 10 fs long pulse on the various NWs. The pulse shows no temporal reshaping in the plasmonic waveguide; only an intensity decay due to ohmic losses is visible. In contrast, in the 300 nm wide Si NW the pulse envelope is distorted due to strong dispersion and the proximity of the mode cut-off. For a 500 nm wide Si NW the guided mode experiences much less dispersion and its bandwidth does not cross the mode cut-off. Consequently the 10 fs pulse does not temporally reshape. Note that the 500 nm wide Si NW supports two modes at this wavelength, and hence its applicability is limited. All curves are normalized to the maximum intensity of the pulse at a propagation distance of 0 μm.

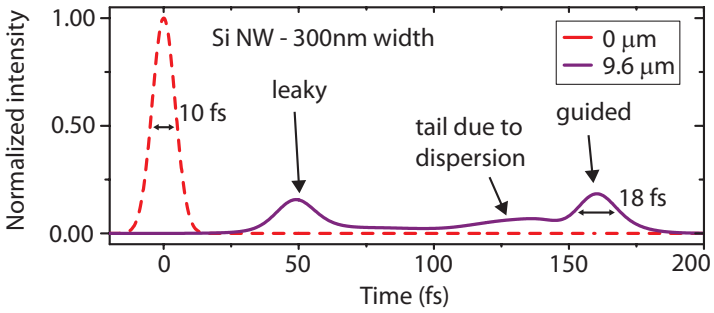

Figure 5.9: Features which are visible in the temporal reshaping of a 10 fs pulse propagating in a 300 nm Si NW. After a propagation distance of 9.6 µm *the pulse has split into two wave packets, which represent the spectral components that cover the spectral areas where the mode in the NW is guided and leaky, respectively. In addition, the pulse, which contains the spectral density in the guided regime, broadens temporally from a FHWM of 10 to 18 fs and develops a tail to shorter times.*

This significant broadening is not surprising as the dispersion length for GVD of this geometry (see above) is shorter than this propagation distance. The tail that develops during propagation can be explained by TOD. The dispersion length for TOD, defined by $L_{D'} = T_0^3/|\beta_3|$, where T_0 is the pulse width and β_3 the TOD coefficient, is 0.7 µm and is therefore significantly smaller than the propagation distance. Consequently, TOD will lead to asymmetric temporal reshaping of the pulse, as can be seen in Fig. 5.9.

This explanation can also be translated to the wider Si NW to understand why this waveguide does not show temporal reshaping of the pulse. Here, the cut-off wavelength, and therefore the highly dispersive regime, is redshifted to longer wavelengths. Since the spectral bandwidth of the pulse is not large enough so that its spectral density covers the shifted cut-off, no dispersion is visible in the 500 nm wide dielectric waveguide. However, please note that this Si NW has limited application prospects, as it supports multiple modes at the telecom wavelength of 1.55 µm. These observations of the pulse reshaping confirm that for few-cycle fs pulses in high-confinement waveguides, Au NWs display superior properties. In general, high-confinement plasmonic waveguides do not exhibit a cut-off for the guided SPP and, hence, can be used in a broad spectral range without becoming multimode (see above). Second, the Au NWs are much less

dispersive than the Si NWs.

Another important feature to consider for pulse propagation applications is the decay behavior of the peak intensity for the various geometries. The peak intensity of a pulse is crucial for applications such as nonlinear optics and contains information about the temporal reshaping during propagation. In contrast to what we observed for the longer pulses, Fig. 5.8 shows that the peak intensity of a 10 fs pulse in the wider Au NW decreases more slowly than in the narrow Si NW. In detail, in the 100 nm wide plasmonic NW the peak intensity drops to 64% of its starting value after a propagation of 3.2 µm, whereas it decreases to 29% in the case of the 300 nm wide dielectric waveguide. The higher peak intensity of the plasmonic mode persists also for longer propagation distances up to 9.6 µm. This advantageous difference, which comes from the drastic temporal reshaping that the pulse undergoes in the Si NW, can be even further increased by using a wider Au NW. Such wide Au NWs are less lossy, albeit at the cost of decreased spatial confinement, although they still feature a smaller mode width than the Si NWs. Thus, the plasmonic waveguides outperform their dielectric waveguides in the case of few cycle pulse propagation if a high spatial confinement and less temporal reshaping are needed.

5.7 Hybrid plasmonic waveguides

While we have compared the performance of plasmonic waveguides with those that are composed purely of dielectrics, there are, of course, also waveguides composed of both metal and dielectric parts. For example, dielectric-loaded plasmonic waveguides (DLSPPWs) consist of a dielectric strip on top of a metallic layer. The modal properties of dielectric-loaded plasmonic waveguides have been thoroughly investigated in the literature [143, 164] and, as can be expected, lie in between those of the pure plasmonic and dielectric waveguides. For example, a narrow dielectric strip on a metal surface will act almost like a pure dielectric waveguide, while if the strip is widened, then its modes will become increasingly plasmonic. Consequently, for these dielectric-loaded plasmonic waveguides, there is an inherent tradeoff between propagation length and mode confinement, where the prior decreases and the latter increases as the mode becomes more plasmonic. Similarly, the GVD of the mode guided in the DLSPPWs, which was found to be on average 10 ps^2/m [143], lies between the group velocity

dispersions that we find for the pure waveguides. There are also more complicated waveguide structures like hybrid plasmonic waveguides[165, 42], which feature superior modal properties, i.e., better confinement and longer propagation lengths. The dispersion in these structures is largely unknown and the topic for future research.

5.8 Conclusion

In conclusion, we demonstrated that Au NWs are promising candidates for applications where high-field confinements and ultrashort-pulse propagation are desired. We experimentally confirmed that light can be confined in smaller areas in Au NWs than in Si NWs. In addition, we show that the low dispersion and the absence of a mode cut-off in plasmonic waveguides can outweigh the inherent ohmic losses, which are absent in their dielectric counterparts, if the applied pulse is as short as 10 fs. The results presented in this chapter reveal the potential of Au NWs for ultrafast photonics on the nanometer scale. For example, the slow decay of the peak intensity of the SPP guided in Au NWs in comparison to the mode in Si NWs will be beneficial for nonlinear optics. Likewise, the negligible temporal reshaping in the plasmonic waveguides can be instrumental to implement short-range ultrafast optical communication systems.

6

Outlook and applications

ABSTRACT: In this chapter we propose a number of future research directions and applications based on the results presented in this thesis. First, we discuss how the capabilities of near-field microscopy to characterize pulse propagation can be enhanced. Introducing an intensity autocorrelation or a Frequency-Resolved Optical Gating (FROG) scheme in the near-field microscope allows a more detailed investigation of the temporal pulse envelope. Further, we illustrate how soliton fission in a nanoscale waveguide could be used to integrate a white light source on chip. Finally, we discuss the possibility of using SPM and four-wave mixing that occur during nonlinear pulse propagation for the regeneration of optical communication signals.

6.1 Complete local temporal characterization of guided light pulses

In section 2.5 we explained how a time-resolved near-field microscope can be used to track pulses as they propagate in waveguides. We characterize the signal pulse by interfering it with a reference pulse as shown schematically in Fig. 6.1a. Although, we identify the measured electric-field cross-correlation in this thesis with the temporal pulse envelope, this is strictly speaking not true. Only in the ideal case, when the reference signal is much shorter than the signal pulse, will convolution effects be prevented and the electric-field cross-correlation yield the temporal envelope of the signal pulse. A reference pulse, which is longer than the signal pulse will invalidate this equality. Moreover, when one of the pulses has a time-dependent frequency, i.e. a chirp, the electric-field cross-correlation will not represent the temporal envelope of the signal pulse anymore.

The electric-field cross-correlation used in this thesis would enable the complete characterization of the signal pulse if the reference pulse would be completely known in amplitude and phase. However, this is a chicken-egg problem. We require the complete knowledge of one pulse to measure a second one. Thus, we must first characterize the reference pulse.

The common way to characterize the temporal pulse duration is to perform an intensity autocorrelation [166], which is schematically illustrated in Fig. 6.1b. In this approach, the pulse is split into two beams, so that one beam can be delayed in time, for example by an optical delay line, in comparison to the other one. Both beams are focused and overlapped on a nonlinear crystal, which features a strong $\chi^{(2)}$ nonlinearity. In this crystal, a nonlinear effect, like second-harmonic generation (SHG) occurs. Finally, this SHG signal is recorded on a detector, like a photodiode.

This approach delivers a signal that depends on the intensity due to the fact that we use a nonlinear effect. In detail, a signal S_{AC} is measured which is proportional to the autocorrelation of the pulse intensity I(t):

$$S_{AC}(\tau) \propto \int I(t)I(t-\tau)dt, \tag{6.1}$$

where τ is the time delay introduced between the two beams.

Measuring the intensity autocorrelation only delivers information about the temporal pulse duration. However, there is no information available

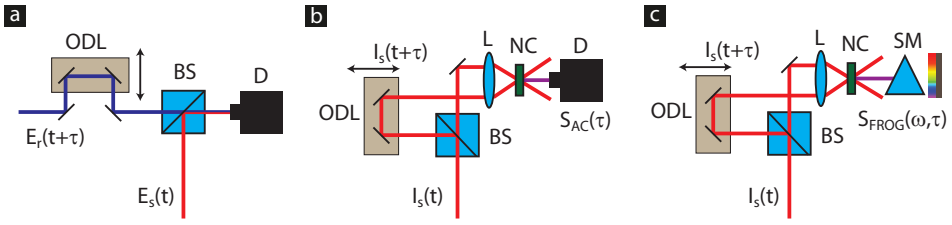

Figure 6.1: Schematics of different methods to characterize a pulse. a) The interferometric electric-field cross-correlation of the pulse with a reference pulse, b) an intensity autocorrelation and c) a FROG measurement approach are illustrated. The abbreviations used in the figure are: BS - beam splitter, ODL - optical delay line, D - detector, L- lens, NC - nonlinear crystal and SM - spectrometer.

about the detailed temporal structure of the pulse or even its phase. To correct these shortcomings a new technique was introduced, frequency-resolved optical gating (FROG) [99]. This measurement approach allows extracting the complete intensity and spectral phase time evolution of a pulse.

In FROG, nearly the same experimental setup as for intensity autocorrelation measurements can be used, only the detector is replaced by a spectrometer (cf. Fig. 6.1c). As a consequence, a spectrally-resolved autocorrelation is measured in this approach, sometimes called a spectrogram. In detail, it holds for the measured intensity $S_{FROG}(\omega, \tau)$:

$$S_{FROG}(\omega, \tau) \propto \left| \int E(t)E(t-\tau)\exp(-\omega t)dt \right|^2, \tag{6.2}$$

where ω is the angular frequency that is investigated.

To determine the complete temporal structure of the pulse the spectrogram has to be post processed. There are several numerical algorithms, which allow the retrieval of the complex temporal envelope from a FROG measurement [99].

Performing the intensity autocorrelation of the signal detected by a near-field probe would allow the local characterization of the temporal pulse length of light propagating in a waveguide. Further, the application of the FROG measurement scheme in a near-field microscope would even deliver the total temporal characterization of a pulse. As a result, more information about pulse propagation in integrated photonic structures can be gained.

There is one limiting factor for employing the intensity autocorrelation or FROG directly in a near-field microscope: the low amount of light collected by the probe. This low power will lead to a very small signal created in the nonlinear crystal, which is required in both detection schemes. A typical optical power level detected by a near-field probe is in the pico- to nanowatt regime [77]. This power level equals a pulse energy in the sub-atto- to femtojoule region for pulse repetition frequencies in the megahertz regime, as used in the laser systems applied in this thesis. Such pulse energies are on the edge of what can be measured with state-of-the-art intensity autocorrelation and FROG implementation [167, 168]. One way to increase the measured pulse energies is to use laser systems with lower repetition frequencies, i.e., in the kilohertz regime. Alternatively, it is possible to use a more sensitive measurement scheme, where, e.g., the signal detected by the near-field probe gets correlated with a very intense reference pulse. A possible implementation would be cross-correlation frequency-resolved optical gating (XFROG), which has been shown to characterize pulses with energies down to the attojoule regime [169].

6.2 On-chip white-light generation

The invention of the laser has undisputedly led to a revolution in optical sciences. This new light source enabled and was useful in a mass of new applications, examples ranging from microscopy and spectroscopy to optical communication systems, where its high brightness and its temporal and spatial coherence properties were of crucial importance [170]. Recently, a new evolutionary step of the laser has been reached by the implementation of spatially-coherent white-light sources, which are based on supercontinuum (SC) generation [171]. SC generation is the process, where the spectral density of a pulse is extremely broadened. That is, spectra spanning more than an octave are created by nonlinear optical effects in a medium [172].

Light sources, which rely on SC generation, are beneficial for a multiplicity of application areas [119]. They have been used for spectroscopy [173], pulse compression [174] and the implementation of tunable ultrashort pulsed lasers [175]. Further, SC generation sources for wavelength-multiplexing optical communication systems have been demonstrated [176]. These novel light sources are also invaluable for frequency metrology involving frequency combs [25]. These are only a few examples of a number of

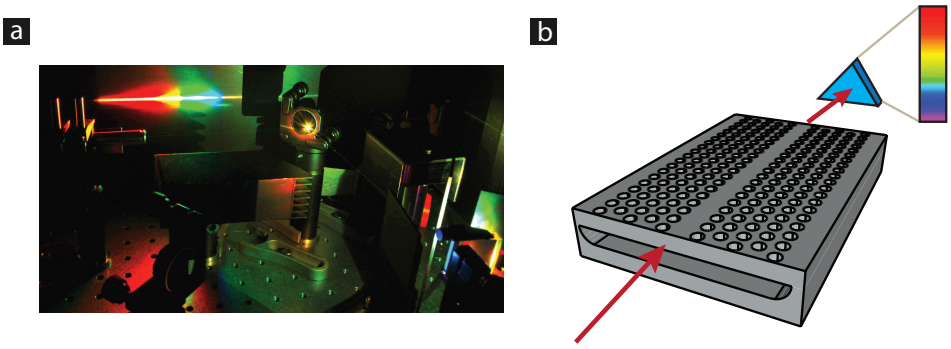

Figure 6.2: SC generation in waveguides. a) Commonly a SC is generated in centimeter to meter long PhC fibers. Here, you see the spectral content of a commercially available spatially coherent white light source based on nonlinear pulse propagation in a PhC fiber. The visible spectrum of this light source is illustrated by dispersing its emission using a grating and projecting it on a screen. b) We propose to achieve the same spectral broadening in a few hundred microns long PhCW, so that the structure could be integrated as broadband light source on a chip.

applications, where the benefits of SC generation, its spatial coherence allowing tight focusing and a large brightness and its broad bandwidth, are exploited.

SC generation is commonly achieved by injecting a short laser pulse, in the femto- to nanosecond regime, into a PhC fiber. An example of the spectrum of a spatially coherent white light source, which is based on nonlinear pulse propagation in a PhC fiber, is shown in Fig. 6.2a. SC generation can be achieved by different combinations of nonlinear effects. Perhaps the most reliable and reproducible way to create a SC spectrum is to exploit the spectral broadening related to soliton propagation and fission [119]. As a consequence, SC spectra are very often generated in PhC fibers, which allow the necessary dispersion engineering and the strong SPM effect required for solitons. In detail, it has been shown that SC generation can occur due to a fission of a higher-order soliton, and a subsequent self-frequency shifting of the generated fundamental solitons, and the emission of dispersive waves [119]. The self-frequency shift of the fundamental solitons generates the long wavelengths of the SC, whereas the dispersive wave emission is responsible for the spectral components at the short wavelength side. In

essence, SC generation in PhC fibers is, in a simplified view, based on three processes: a soliton fission event to generate several wave packets and two mechanisms to redistribute the spectral density and broaden the spectrum.

In chapter 4 we observed a soliton fission event in a PhCW on a length scale of a few hundred microns. Consequently, we can envision generating a SC spectrum by properly adjusting the design of such a waveguide. Moreover, we observed another requirement for SC generation, a blueshift of the spectral density of one of the generated fundamental solitons due to FCD. Finally, it has been reported that also dispersive wave emission can occur in a PhCW that transfers energy to longer wavelengths, if the dispersion relation is properly designed [122]. Consequently, all requirements for the generation of a SC can be met by PhCWs. We believe that by properly designing the PhCW, the interplay of the soliton fission, FCD and dispersive wave emission can be optimized and a SC can be generated, as schematically depicted in Fig. 6.2b.

Finally, we imagine a photonic circuit in which a pulsed semiconductor laser is integrated with a nanoscale PhCW to implement an on-chip SC light source. This structure would provide a very compact alternative for the spacious white light sources used nowadays. Consequently, the integrated circuit would allow performing various applications on chip, like spectroscopy or creating a frequency comb.

There are some limitations to the maximum bandwidth of a SC generated in a PhCW. The ultimate limit of the bandwidth of the SC spectrum is given by the wavelength range that is guided by the waveguide. In the case of a typical PhCW, this bandwidth will be about 100 nm, since this is roughly the useable fraction of the photonic band gap lying below the light line. Finally, the dispersion relation has to be engineered, so that the GVD is minimized. A flat dispersion relation can typically be achieved for a bandwidth of at most a couple of tens of nanometers. Consequently, it seems reasonable to generate a SC with a bandwidth of few tens of nanometers in a PhCW, which is a few hundred microns long. Thus, SC generation in a PhCW is interesting for applications, where a relatively small bandwidth and a very compact device size are required. If a broader spectrum is required, an alternative for on-chip SC generation would be nonlinear pulse propagation in less dispersive waveguides like silicon NWs [108]. Here, a SC with a bandwidth of a few hundred nanometers can be produced, but with a propagation length of a few millimeters. Thus, there is a trade-off

to be made in respect to the bandwidth of the SC and the propagation distance required for its generation.

6.3 All-optical regeneration on an integrated plasmonic platform

There are three detrimental effects that occur in optical communication networks, which limit the distance that can be covered between the source and the detector: the attenuation due to losses in the system, distortion due to temporal reshaping of the optical signals and time jitter. They are battled by the use of optical repeater devices. The optical repeater corrects these issues by providing a reamplificication, a reshaping and a retiming mechanism, which is called the 3R scheme [105]. In the ideal case, the optical repeater is an all optical device, avoiding the need for optical-to-electronical conversion, since this provides benefits in terms of energy efficiency, bandwidth and ease of integration. An integral part of the 3R scheme is the amplification of a signal, a process which is also called optical regeneration.

Optical regenerators have been implemented in waveguides using a variety of nonlinear effects. It has been shown that SPM in combination with an optical band pass filter can provide amplification and reshaping [177]. Further, an optical generator, which also performs retiming, can be implemented by using four-wave mixing (4WM). 4WM is a nonlinear process, also based on the third-order susceptibility $\chi^{(3)}$, in which four waves are interacting. The optical regeneration is achieved in this scheme by generating a new wave at a different wavelength, which acts as refreshed signal that is later filtered out. A reamplification is achieved, since the signal-to-noise ratio gets enhanced due to the nonlinear character of the wavelength transfer, i.e., noise gets suppressed. The platforms that have been used to implement all-optical signal regeneration are optical fibers [178] and silicon NWs [105], where propagation length in the kilometer and millimeter to centimeter regime are required, respectively.

One way to implement a compact optical regenerator, with a length scale of tenth of micrometers, could be based on a slow-light PhCW [179]. We have shown in chapters 3 and 4 that the SPM effect can be enhanced by up to two orders of magnitude by the slow-light enhancement in these structures. Since 4WM relies on the same nonlinearity it will experience

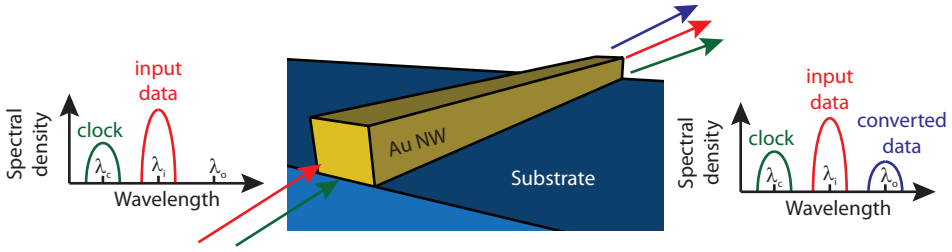

Figure 6.3: Schematics of using a gold NW as optical generator by exploiting 4WM occurring in the waveguide.

a similar efficiency boost. Further, we can imagine a photonic chip, where besides the waveguide a band pass filter is integrated, so that it features all components required for performing the optical regeneration on chip.

In chapter 5 we have demonstrated that gold NWs are interesting waveguides for ultrashort-pulse propagation due to their low dispersion. Further, it has been shown that the Kerr coefficient of gold can be orders of magnitude larger in the visible regime than the one of silica [180] leading to studies of SPM of SPPs [181] and 4WM on structured metal films [182]. Thus, we envision the possibility to implement optical regeneration in a plasmonic waveguide, as schematically depicted in Fig. 6.3. This approach would potentially allow the further reduction of the device to a few microns, due to the high spatial confinement achieved in plasmonics. Further, the plasmonic waveguide would offer a broad operational bandwidth due to the low dispersion allowing the wavelengths to be tuned over a large regime without creating a major phase mismatch. In the case that the nonlinearity in the gold alone is not strong enough, a nonlinear substrate could be used to boost the SPM or 4WM effect.

The limiting factor for building an optical regenerator using a plasmonic NW will be the ohmic losses that occur in the metal. At the moment it is not known if the propagation length in the plasmonic structure is long enough to observe efficient SPM or 4WM. By considering the typical decay of the mode in a Au NW, as investigated in chapter 5, it is obvious that the nonlinear effects have to occur on the first few microns of propagation distance. Investigating nonlinear optical effects in plasmonic waveguides is the topic of on-going research.

Bibliography

[1] G. P. Agrawal, *Fiber-optics communication systems*. Wiley, 2002.

[2] G. S. He and S. H. Liu, *Physics of Nonlinear Optics*. World Scientific Publishing, 1999.

[3] Y. R. Shen, *The Principles of Nonlinear Optics*. John Wiley & Sons, Inc., 1984.

[4] R. L. Sutherland, *Handbook of Nonlinear Optics*. Marcel Dekker, Inc., 2003.

[5] E. Garmire, "Nonlinear optics in daily life," *Opt. Express*, vol. 21, pp. 30532–30544, 2013.

[6] T. Schneider, *Nonlinear Optics in Telecommunications*. Springer, 2004.

[7] R. W. Boyd, *Nonlinear Optics*. Academic Press, 2008.

[8] G. P. Agrawal, *Nonlinear Fiber Optics*. Academic Press, 2001.

[9] A. Penzkofer, "Theoretical analysis of pulse shaping of self-phase modulated pulses in a grating pair compressor," *Opt. Quant. Electron.*, vol. 23, pp. 685–702, 1991.

[10] R. A. Soref and B. Bennett, "Electrooptical effects in silicon," *IEEE J. Quantum Electron.*, vol. 23, pp. 123–129, 1987.

[11] V. R. Almeida, C. A. Barrios, R. R. Panepucci, and M. Lipson, "All-optical control of light on a silicon chip," *Nature*, vol. 431, pp. 1081–1084, 2004.

[12] C. Manolatou and M. Lipson, "All-optical silicon modulators based on carrier injection by two-photon absorption," *J. Lightwave Technol.*, vol. 24, p. 1433, 2006.

[13] A. Opheij, N. Rotenberg, D. M. Beggs, I. H. Rey, T. F. Krauss, and L. Kuipers, "Ultracompact (3 μm) silicon slow-light optical modulator," *Sci. Rep.*, vol. 3, p. 3546, 2013.

[14] D. M. Beggs, I. H. Rey, T. Kampfrath, N. Rotenberg, L. Kuipers, and T. F. Krauss, "Ultrafast tunable optical delay line based on indirect photonic transitions," *Phys. Rev. Lett.*, vol. 108, p. 213901, 2012.

[15] S. Khan, M. A. Baghban, and S. Fathpour, "Electronically tunable silicon photonic delay lines," *Opt. Express*, vol. 19, pp. 11780–11785, 2011.

[16] X. Luo, H. Chen, and A. W. Poon, "Electro-optical tunable time delay and advance in silicon microring resonators," *Opt. Lett.*, vol. 35, pp. 2940–2942, 2010.

[17] Q. Xu and M. Lipson, "Carrier-induced optical bistability in silicon ring resonators," *Opt. Lett.*, vol. 31, pp. 341–343, 2006.

[18] O. V. Sinkin, R. Holzlöhner, J. Zweck, and C. R. Menyuk, "Optimization of the split-step fourier method in modeling optical-fiber communications systems," *J. Lightwave Technol.*, vol. 21, pp. 61–68, 2003.

[19] L. Yin and G. P. Agrawal, "Impact of two-photon absorption on self-phase modulation in silicon waveguides," *Opt. Lett.*, vol. 32, pp. 2031–2033, 2007.

[20] Y. S. Kivshar and G. P. Agrawal, *Optical Solitons: From Fibers to Photonic Crystals*. Academic Press, 2003.

[21] P. K. A. Wai, C. R. Menyuk, Y. C. Lee, and H. H. Chen, "Nonlinear pulse propagation in the neighborhood of the zero-dispersion wavelength of monomode optical fibers," *Opt. Lett.*, vol. 11, pp. 464–466, 1986.

[22] K. Tai, N. Bekki, and A. Hasegawa, "Fission of optical solitons induced by stimulated raman effect," *Opt. Lett.*, vol. 13, pp. 392–394, 1988.

[23] J. Herrmann, U. Griebner, N. Zhavoronkov, A. Husakou, D. Nickel, J. C. Knight, W. J. Wadsworth, P. S. J. Russell, and G. Korn, "Experimental evidence for supercontinuum generation by fission of higher-order solitons in photonic fibers," *Phys. Rev. Lett.*, vol. 88, p. 173901, 2002.

[24] L. Froehly and J. Meteau, "Supercontinuum sources in optical coherence tomography: A state of the art and the application to scan-free time domain correlation techniques and depth dependant dispersion compensation," *Opt. Fiber Technol.*, vol. 18, pp. 411 – 419, 2012.

[25] T. Udem, R. Holzwarth, and T. W. Hänsch, "Optical frequency metrology," *Nature*, vol. 416, pp. 233–237, 2002.

[26] H. A. Haus and W. S. Wong, "Solitons in optical communications," *Rev. Mod. Phys.*, vol. 68, pp. 423–444, 1996.

[27] S. Sanders, "Wavelength-agile fiber laser using group-velocity dispersion of pulsed super-continua and application to broadband absorption spectroscopy," *Appl. Phys. B*, vol. 75, pp. 799–802, 2002.

[28] S. Combrié, Q. V. Tran, A. De Rossi, C. Husko, and P. Colman, "High quality gainp nonlinear photonic crystals with minimized nonlinear absorption," *Appl. Phys. Lett.*, vol. 95, p. 221108, 2009.

[29] D. K. Gramotnev and S. I. Bozhevolnyi, "Plasmonics beyond the diffraction limit," *Nature Photon.*, vol. 4, pp. 83–91, 2010.

[30] D. K. Gramotnev and S. I. Bozhevolnyi, "Nanofocusing of electromagnetic radiation," *Nature Photon.*, vol. 8, pp. 13–22, 2014.

[31] T. Baba, "Slow light in photonic crystals," *Nature Photon.*, vol. 2, pp. 465–473, 2008.

[32] T. F. Krauss, "Slow light in photonic crystal waveguides," *J. Phys. D: Appl. Phys.*, vol. 40, p. 2666, 2007.

[33] H. Raether, *Surface Plasmons on Smooth and Rough Surfaces and on Gratings*. Springer, 1986.

[34] S. A. Maier, *Plasmonics: Fundamentals and Applications*. Springer, 2007.

[35] E. Devaux, T. W. Ebbesen, J.-C. Weeber, and A. Dereux, "Launching and decoupling surface plasmons via micro-gratings," *Appl. Phys. Lett.*, vol. 83, pp. 4936–4938, 2003.

[36] A. Otto, "Excitation of nonradiative surface plasma waves in silver by the method of frustrated total reflection," *Z. Phys.*, vol. 216, pp. 398–410, 1968.

[37] E. Verhagen, M. Spasenović, A. Polman, and L. K. Kuipers, "Nanowire plasmon excitation by adiabatic mode transformation," *Phys. Rev. Lett.*, vol. 102, p. 203904, 2009.

[38] E. Moreno, S. G. Rodrigo, S. I. Bozhevolnyi, L. Martín-Moreno, and F. J. García-Vidal, "Guiding and focusing of electromagnetic fields with wedge plasmon polaritons," *Phys. Rev. Lett.*, vol. 100, p. 023901, 2008.

[39] S. I. Bozhevolnyi, V. S. Volkov, E. Devaux, and T. W. Ebbesen, "Channel plasmon-polariton guiding by subwavelength metal grooves," *Phys. Rev. Lett.*, vol. 95, p. 046802, 2005.

[40] T. Holmgaard, J. Gosciniak, and S. I. Bozhevolnyi, "Long-range dielectric-loaded surface plasmon-polariton waveguides," *Opt. Express*, vol. 18, pp. 23009–23015, 2010.

[41] M. I. Stockman, "Nanofocusing of optical energy in tapered plasmonic waveguides," *Phys. Rev. Lett.*, vol. 93, p. 137404, 2004.

[42] V. J. Sorger, Z. Ye, R. F. Oulton, Y. Wang, G. Bartal, X. Yin, and X. Zhang, "Experimental demonstration of low-loss optical waveguiding at deep sub-wavelength scales," *Nature Commun.*, vol. 2, p. 331, 2011.

[43] E. Verhagen, L. Kuipers, and A. Polman, "Enhanced nonlinear optical effects with a tapered plasmonic waveguide," *Nano Lett.*, vol. 7, pp. 334–337, 2007.

[44] H. Choo, M.-K. Kim, M. Staffaroni, T. J. Seok, J. Bokor, S. Cabrini, P. J. Schuck, M. C. Wu, and E. Yablonovitch, "Nanofocusing in a metal-insulator-metal gap plasmon waveguide with a three-dimensional linear taper," *Nature Photon.*, vol. 6, pp. 838–844, 2012.

[45] I.-Y. Park, S. Kim, J. Choi, D.-H. Lee, Y.-J. Kim, M. F. Kling, M. I. Stockman, and S.-W. Kim, "Plasmonic generation of ultrashort extreme-ultraviolet light pulses," *Nature Photon.*, vol. 5, pp. 677–681, 2011.

[46] S. Noda and T. Baba, eds., *Roadmap on Photonic Crystals*. Kluwer Academic Press, 2003.

[47] J. D. Joannopoulos, S. G. Johnson, J. N. Winn, and R. D. Meade, *Photonic Crystals: Molding the Flow of Light*. Princeton University Press, 2008.

[48] P. Russell, "Optics of floquet-bloch waves in dielectric gratings," *Appl. Phys. B*, vol. 39, pp. 231–246, 1986.

[49] R. J. P. Engelen, *Ultrafast investigations of slow light in photonic crystal structures*. PhD thesis, University of Twente, 2008.

[50] M. Burresi, *Nanoscale investigation of light-matter interactions mediated by magnetic and electric coupling*. PhD thesis, University of Twente, 2009.

[51] S. G. Johnson, P. R. Villeneuve, S. Fan, and J. D. Joannopoulos, "Linear waveguides in photonic-crystal slabs," *Phys. Rev. B*, vol. 62, pp. 8212–8222, 2000.

[52] E. Chow, S. Lin, S. Johnson, P. Villeneuve, J. Joannopoulos, J. Wendt, G. Vawter, W. Zubrzycki, H. Hou, and A. Alleman, "Three-dimensional control of light in a two-dimensional photonic crystal," *Nature*, vol. 407, pp. 983–986, 2000.

[53] L. O'Faolain, X. Yuan, D. McIntyre, S. Thoms, H. Chong, R. De La Rue, and T. Krauss, "Low-loss propagation in photonic crystal waveguides," *Electron. Lett.*, vol. 42, pp. 1454–1455, 2006.

[54] P. Colman, S. Combrié, G. Lehoucq, and A. D. Rossi, "Control of dispersion in photonic crystal waveguides using group symmetry theory," *Opt. Express*, vol. 20, pp. 13108–13114, 2012.

[55] M. Soljačić and J. D. Joannopoulos, "Enhancement of nonlinear effects using photonic crystals," *Nature Mater.*, vol. 3, pp. 211–219, 2004.

[56] N. A. R. Bhat and J. E. Sipe, "Optical pulse propagation in nonlinear photonic crystals," *Phys. Rev. E*, vol. 64, p. 056604, 2001.

[57] C. Monat, B. Corcoran, M. Ebnali-Heidari, C. Grillet, B. J. Eggleton, T. P. White, L. O'Faolain, and T. F. Krauss, "Slow light enhancement of nonlinear effects in silicon engineered photonic crystal waveguides," *Opt. Express*, vol. 17, pp. 2944–2953, 2009.

[58] R. De La Rue and C. Seassal, "Photonic crystal devices: some basics and selected topics," *Laser Photon. Rev.*, vol. 6, pp. 564–597, 2012.

[59] J. Li, T. P. White, L. O'Faolain, A. Gomez-Iglesias, and T. F. Krauss, "Systematic design of flat band slow light in photonic crystal waveguides," *Opt. Express*, vol. 16, pp. 6227–6232, 2008.

[60] B. Corcoran., C. Monat, C. Grillet, D. J. Moss, B. J. Eggleton, T. P. White, L. O'Faolain, and T. F. Krauss, "Green light emission in silicon through slow-light enhanced third-harmonic generation in photonic-crystal waveguides," *Nature Photon.*, vol. 3, pp. 206–210, 2009.

[61] P. Colman, C. Husko, S. Combrie, I. Sagnes, C. W. Wong, and A. D. Rossi, "Temporal solitons and pulse compression in photonic crystal waveguides," *Nature Photon.*, vol. 4, pp. 862–868, 2010.

[62] M. Ohtsu and H. Hori, *Near-Field Nano-Optics: From Basic Principles to Nano-Fabrication and Nano-Photonics*. Springer, 1999.

[63] A. V. Zayats and D. Richards, eds., *Nano-Optics and Near-Field Optical Microscopy*. Artech House, 2008.

[64] E. A. Ash and G. Nicholls, "Super-resolution aperture scanning microscope," *Nature*, vol. 237, pp. 510–512, 1972.

[65] D. W. Pohl, W. Denk, and M. Lanz, "Optical stethoscopy: Image recording with resolution $\lambda/20$," *Appl. Phys. Lett.*, vol. 44, pp. 651–653, 1984.

[66] E. Betzig, J. K. Trautman, T. D. Harris, J. S. Weiner, and R. L. Kostelak, "Breaking the diffraction barrier: Optical microscopy on a nanometric scale," *Science*, vol. 251, pp. 1468–1470, 1991.

[67] D. P. Tsai, H. E. Jackson, R. C. Reddick, S. H. Sharp, and R. J. Warmack, "Photon scanning tunneling microscope study of optical waveguides," *Appl. Phys. Lett.*, vol. 56, pp. 1515–1517, 1990.

[68] A. G. Choo, H. E. Jackson, U. Thiel, G. N. De Brabander, and J. T. Boyd, "Near field measurements of optical channel waveguides and directional couplers," *Appl. Phys. Lett.*, vol. 65, pp. 947–949, 1994.

[69] Y. Toda and M. Ohtsu, "High spatial resolution diagnostics of optical waveguides using a photon-scanning tunneling microscope," *IEEE Photon. Technol. Lett.*, vol. 7, pp. 84–86, 1995.

[70] G. H. Vander Rhodes, B. B. Goldberg, M. S. Ünlü, S. T. Chu, W. Pan, T. Kaneko, Y. Kokobun, and B. E. Little, "Measurement of internal spatial modes and local propagation properties in optical waveguides," *Appl. Phys. Lett.*, vol. 75, pp. 2368–2370, 1999.

[71] M. L. M. Balistreri, J. P. Korterik, G. J. Veldhuis, L. Kuipers, and N. F. van Hulst, "Quantitative photon tunneling and shear-force microscopy of planar waveguide splitters and mixers," *J. Appl. Phys.*, vol. 89, pp. 3307–3314, 2001.

[72] M. L. M. Balistreri, H. Gersen, J. P. Korterik, L. Kuipers, and N. F. van Hulst, "Tracking femtosecond laser pulses in space and time," *Science*, vol. 294, pp. 1080–1082, 2001.

[73] M. Abashin, K. Ikeda, R. Saperstein, and Y. Fainman, "Heterodyne near-field scanning optical microscopy with spectrally broad sources," *Opt. Lett.*, vol. 34, pp. 1327–1329, 2009.

[74] J. D. Mills, T. Chaipiboonwong, W. S. Brocklesby, M. D. B. Charlton, M. E. Zoorob, C. Netti, and J. J. Baumberg, "Observation of

the developing optical continuum along a nonlinear waveguide," *Opt. Lett.*, vol. 31, pp. 2459–2461, 2006.

[75] J. A. Veerman, A. M. Otter, L. Kuipers, and N. F. van Hulst, "High definition aperture probes for near-field optical microscopy fabricated by focused ion beam milling," *Appl. Phys. Lett.*, vol. 72, pp. 3115–3117, 1998.

[76] A. Bek, R. Vogelgesang, and K. Kern, "Apertureless scanning near field optical microscope with sub-10nm resolution," *Rev. Sci. Instrum.*, vol. 77, p. 043703, 2006.

[77] M. L. M. Balistreri, *Coherent imaging of guided optical fields.* PhD thesis, University of Twente, 2000.

[78] K. Karrai and R. D. Grober, "Piezoelectric tip-sample distance control for near field optical microscopes," *Appl. Phys. Lett.*, vol. 66, pp. 1842–1844, 1995.

[79] A. G. T. Ruiter, J. A. Veerman, K. O. van der Werf, and N. F. van Hulst, "Dynamic behavior of tuning fork shear-force feedback," *Appl. Phys. Lett.*, vol. 71, pp. 28–30, 1997.

[80] E. Betzig, P. L. Finn, and J. S. Weiner, "Combined shear force and near-field scanning optical microscopy," *Appl. Phys. Lett.*, vol. 60, pp. 2484–2486, 1992.

[81] B. le Feber, N. Rotenberg, D. M. Beggs, and L. Kuipers, "Simultaneous measurement of nanoscale electric and magnetic optical fields," *Nature Photon.*, vol. 8, pp. 43–46, 2014.

[82] A. Richter, G. Behme, M. Süptitz, C. Lienau, T. Elsaesser, M. Ramsteiner, R. Nötzel, and K. H. Ploog, "Real-space transfer and trapping of carriers into single gaas quantum wires studied by near-field optical spectroscopy," *Phys. Rev. Lett.*, vol. 79, pp. 2145–2148, 1997.

[83] N. Louvion, D. Gérard, J. Mouette, F. de Fornel, C. Seassal, X. Letartre, A. Rahmani, and S. Callard, "Local observation and spectroscopy of optical modes in an active photonic-crystal microcavity," *Phys. Rev. Lett.*, vol. 94, p. 113907, 2005.

[84] F. Huth, M. Schnell, J. Wittborn, N. Ocelic, and R. Hillenbrand, "Infrared-spectroscopic nanoimaging with a thermal source," *Nature Mater.*, vol. 10, pp. 352–356, 2011.

[85] J. D. Mills, T. Chaipiboonwong, W. S. Brocklesby, M. D. B. Charlton, C. Netti, M. E. Zoorob, and J. J. Baumberg, "Group velocity measurement using spectral interference in near-field scanning optical microscopy," *Appl. Phys. Lett.*, vol. 89, p. 051101, 2006.

[86] B. E. A. Saleh and M. C. Teich, *Fundamentals of Photonics.* Wiley-Interscience, 2007.

[87] E. Hecht, *Optics.* Addison-Wesley, 2001.

[88] L. Zehnder, "Ein neuer interferenzrefraktor," *Z. Instrumentkd.*, vol. 11, pp. 275–285, 1891.

[89] L. Mach, "Über einen interferenzrefraktor," *Z. Instrumentkd.*, vol. 12, pp. 89–93, 1892.

[90] M. Burresi, R. J. P. Engelen, A. Opheij, D. van Oosten, D. Mori, T. Baba, and L. Kuipers, "Observation of polarization singularities at the nanoscale," *Phys. Rev. Lett.*, vol. 102, p. 033902, 2009.

[91] M. L. M. Balistreri, J. P. Korterik, L. Kuipers, and N. F. van Hulst, "Local observations of phase singularities in optical fields in waveguide structures," *Phys. Rev. Lett.*, vol. 85, pp. 294–297, 2000.

[92] P. Tortora, M. Abashin, I. Märki, W. Nakagawa, L. Vaccaro, M. Salt, H. Herzig, U. Levy, and Y. Fainman, "Observation of amplitude and phase in ridge and photonic crystal waveguides operating at 1.55μm by use of heterodyne scanning near-field optical microscopy," *Opt. Lett.*, vol. 30, pp. 2885–2887, 2005.

[93] A. Korpel, *Acousto-Optics.* Marcel Dekker, Inc., 1997.

[94] W. C. Michels and N. L. Curtis, "A pentode lock-in amplifier of high frequency selectivity," *Rev. Sci. Instrum.*, vol. 12, pp. 444–447, 1941.

[95] P. A. Probst and B. Collet, "Low-frequency digital lock-in amplifier," *Rev. Sci. Instrum.*, vol. 56, pp. 466–470, 1985.

[96] J. W. Goodman, *Statistical Optics*. Wil, 2000.

[97] M. Sandtke, R. J. P. Engelen, H. Schoenmaker, I. Attema, H. Dekker, I. Cerjak, J. P. Korterik, F. B. Segerink, and L. Kuipers, "Novel instrument for surface plasmon polariton tracking in space and time," *Rev. Sci. Instrum.*, vol. 79, p. 013704, 2008.

[98] M. Sandtke, *Surface plasmon polariton propagation in straight and tailored waveguides*. PhD thesis, University of Twente, 2007.

[99] R. Trebino, *Frequency-Resolved Optical Gating: The Measurement of Ultrashort Laser Pulses*. Springer, 2002.

[100] H. Gersen, J. P. Korterik, N. F. van Hulst, and L. Kuipers, "Tracking ultrashort pulses through dispersive media: Experiment and theory," *Phys. Rev. E*, vol. 68, p. 026604, 2003.

[101] C. Koos, P. Vorreau, T. Vallaitis, P. Dumon, W. Bogaerts, R. Baets, B. Esembeson, I. Biaggio, T. Michinobu, F. Diederich, W. Freude, and J. Leuthold, "All-optical high-speed signal processing with silicon-organic hybrid slot waveguides," *Nature Photon.*, vol. 3, pp. 216–219, 2009.

[102] F. Xia, L. Sekaric, and Y. A. Vlasov, "Ultracompact optical buffers on a silicon chip," *Nature Photon.*, vol. 1, pp. 65–71, 2007.

[103] Y. A. Vlasov, M. O'Boyle, H. F. Hamann, and S. J. McNab, "Active control of slow light on a chip with photonic crystal waveguides," *Nature*, vol. 438, pp. 65–69, 2005.

[104] M. A. Foster, A. C. Turner, J. E. Sharping, B. S. Schmidt, M. Lipson, and A. L. Gaeta, "Broad-band optical parametric gain on a silicon photonic chip," *Nature*, vol. 441, pp. 960–963, 2006.

[105] R. Salem, M. A. Foster., A. C. Turner, D. F.Geraghty, M. Lipson, and A. L. Gaeta, "Signal regeneration using low-power four-wave mixing on silicon chip," *Nature Photon.*, vol. 2, pp. 35–38, 2008.

[106] O. Boyraz, T. Indukuri, and B. Jalali, "Self-phase-modulation induced spectral broadening in silicon waveguides," *Opt. Express*, vol. 12, pp. 829–834, 2004.

[107] G. W. Rieger, K. S. Virk, and J. F. Young, "Nonlinear propagation of ultrafast 1.5 μm pulses in high-index-contrast silicon-on-insulator waveguides," *Appl. Phys. Lett.*, vol. 84, pp. 900–902, 2004.

[108] I.-W. Hsieh, X. Chen, X. Liu, J. I. Dadap, N. C. Panoiu, C.-Y. Chou, F. Xia, W. M. Green, Y. A. Vlasov, and R. M. Osgood, "Supercontinuum generation in silicon photonic wires," *Opt. Express*, vol. 15, pp. 15242–15249, 2007.

[109] C. Husko, S. Combrié, Q. V. Tran, F. Raineri, C. W. Wong, and A. D. Rossi, "Non-trivial scaling of self-phase modulation and three-photon absorption in iii-v photonic crystal waveguides," *Opt. Express*, vol. 17, pp. 22442–22451, 2009.

[110] G. Roberts, F. Taenzler, and M. Burns, *An Introduction to Mixed-Signal IC Test and Measurement*. Oxford University Press, 2011.

[111] S. McNab, N. Moll, and Y. Vlasov, "Ultra-low loss photonic integrated circuit with membrane-type photonic crystal waveguides," *Opt. Express*, vol. 11, pp. 2927–2939, 2003.

[112] C. P. Reardon, I. H. Rey, K. Welna, L. O'Faolain, and T. F. Krauss, "Fabrication and characterization of photonic crystal slow light waveguides and cavities," *J. Vis. Exp.*, vol. 69, p. E50216, 2012.

[113] A. Gomez-Iglesias, D. O'Brien, L. O'Faolain, A. Miller, and T. F. Krauss, "Direct measurement of the group index of photonic crystal waveguides via fourier transform spectral interferometry," *Appl. Phys. Lett.*, vol. 90, p. 261107, 2007.

[114] S. Johnson and J. Joannopoulos, "Block-iterative frequency-domain methods for maxwell's equations in a planewave basis," *Opt. Express*, vol. 8, pp. 173–190, 2001.

[115] H. Gersen, T. J. Karle, R. J. P. Engelen, W. Bogaerts, J. P. Korterik, N. F. van Hulst, T. F. Krauss, and L. Kuipers, "Direct observation of bloch harmonics and negative phase velocity in photonic crystal waveguides," *Phys. Rev. Lett.*, vol. 94, p. 123901, 2005.

[116] R. Dekker, N. Usechak, M. Föst, and A. Driessen, "Ultrafast nonlinear all-optical processes in silicon-on-insulator waveguides," *J. Phys. D: Appl. Phys.*, vol. 40, pp. R249–R271, 2007.

[117] M. Dinu, F. Quochi, and H. Garcia, "Third-order nonlinearities in silicon at telecom wavelengths," *Appl. Phys. Lett.*, vol. 82, pp. 2954–2956, 2003.

[118] B. Corcoran, C. Monat, D. Pudo, B. J. Eggleton, T. F. Krauss, D. J. Moss, L. O'Faolain, M. Pelusi, and T. P. White, "Nonlinear loss dynamics in a silicon slow-light photonic crystal waveguide," *Opt. Lett.*, vol. 35, pp. 1073–1075, 2010.

[119] J. M. Dudley, G. Genty, and S. Coen, "Supercontinuum generation in photonic crystal fiber," *Rev. Mod. Phys.*, vol. 78, pp. 1135–1184, 2006.

[120] L. Yin, Q. Lin, and G. P. Agrawal, "Soliton fission and supercontinuum generation in silicon waveguides," *Opt. Lett.*, vol. 32, pp. 391–393, 2007.

[121] A. Blanco-Redondo, C. Husko, D. Eades, Y. Zhang, J. Li, T. Krauss, and B. Eggleton, "Observation of soliton compression in silicon photonic crystals," *Nature Commun.*, vol. 5, p. 3160, 2014.

[122] P. Colman, S. Combrié, G. Lehoucq, A. de Rossi, and S. Trillo, "Blue self-frequency shift of slow solitons and radiation locking in a line-defect waveguide," *Phys. Rev. Lett.*, vol. 109, p. 093901, 2012.

[123] C. A. Husko, S. Combrié, P. Colman, J. Zheng, A. De Rossi, and C. W. Wong, "Soliton dynamics in the multiphoton plasma regime," *Sci. Rep.*, vol. 3, p. 1100, 2013.

[124] Q. V. Tran, S. Combrié, P. Colman, and A. De Rossi, "Photonic crystal membrane waveguides with low insertion losses," *Appl. Phys. Lett.*, vol. 95, p. 061105, 2009.

[125] S. Combrié, N.-V.-Q. Tran, E. Weidner, A. De Rossi, S. Cassette, P. Hamel, Y. Jaoun, R. Gabet, and A. Talneau, "Investigation of group delay, loss, and disorder in a photonic crystal waveguide by low-coherence reflectometry," *Appl. Phys. Lett.*, vol. 90, p. 231104, 2007.

[126] M. Sheik-Bahae, D. J. Hagan, and E. W. Van Stryland, "Dispersion and band-gap scaling of the electronic kerr effect in solids associated

with two-photon absorption," *Phys. Rev. Lett.*, vol. 65, pp. 96–99, 1990.

[127] B. Bennett, R. A. Soref, and J. del Alamo, "Carrier-induced change in refractive index of inp, gaas and ingaasp," *IEEE J. Quantum Electron.*, vol. 26, pp. 113–122, 1990.

[128] Y. Kodama and A. Hasegawa, "Nonlinear pulse propagation in a monomode dielectric guide," *Quantum Electronics, IEEE Journal of*, vol. 23, pp. 510–524, 1987.

[129] V. Kravtsov, J. M. Atkin, and M. B. Raschke, "Group delay and dispersion in adiabatic plasmonic nanofocusing," *Opt. Lett.*, vol. 38, pp. 1322–1324, 2013.

[130] T. F. Krauss, "Why do we need slow light?," *Nature Photon.*, vol. 2, pp. 448–450, 2008.

[131] B. Jalali and S. Fathpour, "Silicon photonics," *J. Lightwave Technol.*, vol. 24, pp. 4600–4615, 2006.

[132] R. G. Hunsperger, *Integrated Optics: Theory and Technology*. Springer, 2009.

[133] C. R. Pollock and M. Lipson, *Integrated Photonics*. Kluwer Academic Publishers, 2003.

[134] M. Asghari and A. V. Krishnamoorthy, "Silicon photonics: Energy-efficient communication," *Nature Photon.*, vol. 5, pp. 268–270, 2011.

[135] M. I. Stockman, M. F. Kling, U. Kleineberg, and F. Krausz, "Attosecond nanoplasmonic-field microscope," *Nature Photon.*, vol. 1, pp. 539–544, 2007.

[136] M. I. Stockman, "Nanoplasmonics: past, present, and glimpse into future," *Opt. Express*, vol. 19, pp. 22029–22106, 2011.

[137] S. Kim, J. Jin, Y.-J. Kim, I.-Y. Park, Y. Kim, and S.-W. Kim, "High-harmonic generation by resonant plasmon field enhancement," *Nature*, vol. 453, pp. 757–760, 2008.

[138] T. Hanke, G. Krauss, D. Träutlein, B. Wild, R. Bratschitsch, and A. Leitenstorfer, "Efficient nonlinear light emission of single gold optical antennas driven by few-cycle near-infrared pulses," *Phys. Rev. Lett.*, vol. 103, p. 257404, 2009.

[139] M. Sivis, M. Duwe, B. Abel, and C. Ropers, "Extreme-ultraviolet light generation in plasmonic nanostructures," *Nature Phys.*, vol. 9, pp. 304–309, 2013.

[140] L. Douillard, F. Charra, Z. Korczak, R. Bachelot, S. Kostcheev, G. Lerondel, P.-M. Adam, and P. Royer, "Short range plasmon resonators probed by photoemission electron microscopy," *Nano Lett.*, vol. 8, pp. 935–940, 2008.

[141] C. Hrelescu, T. K. Sau, A. L. Rogach, F. Jäckel, G. Laurent, L. Douillard, and F. Charra, "Selective excitation of individual plasmonic hotspots at the tips of single gold nanostars," *Nano Lett.*, vol. 11, pp. 402–407, 2011.

[142] E. Moreno, l. F. J. García-Vida, S. G. Rodrigo, L. Martín-Moreno, and S. I. Bozhevolnyi, "Channel plasmon-polaritons: modal shape, dispersion, and losses," *Opt. Lett.*, vol. 31, pp. 3447–3449, 2006.

[143] A. V. Krasavin and A. V. Zayats, "Silicon-based plasmonic waveguides," *Opt. Express*, vol. 18, pp. 11791–11799, 2010.

[144] T. Leißner, C. Lemke, J. Fiutowski, J. W. Radke, A. Klick, L. Tavares, J. Kjelstrup-Hansen, H.-G. Rubahn, and M. Bauer, "Morphological tuning of the plasmon dispersion relation in dielectric-loaded nanofiber waveguides," *Phys. Rev. Lett.*, vol. 111, p. 046802, 2013.

[145] M. Sandtke and L. Kuipers, "Slow guided surface plasmons at telecom frequencies," *Nature Photon.*, vol. 1, pp. 573–576, 2007.

[146] C. Rewitz, T. Keitzl, P. Tuchscherer, J.-S. Huang, P. Geisler, G. Razinskas, B. Hecht, and T. Brixner, "Ultrafast plasmon propagation in nanowires characterized by far-field spectral interferometry," *Nano Lett.*, vol. 12, pp. 45–49, 2012.

[147] A. Kubo, N. Pontius, and H. Petek, "Femtosecond microscopy of surface plasmon polariton wave packet evolution at the silver/vacuum interface," *Nano Lett.*, vol. 7, pp. 470–475, 2007.

[148] C. Lemke, T. Leißner, A. Klick, J. Fiutowski, J. W. Radke, M. Thomaschewski, J. Kjelstrup-Hansen, H.-G. Rubahn, and M. Bauer, "The complex dispersion relation of surface plasmon polaritons at gold/para-hexaphenylene interfaces," *Appl. Phys. B*, vol. 116, pp. 585–591, 2014.

[149] P. Geisler, G. Razinskas, E. Krauss, X.-F. Wu, C. Rewitz, P. Tuchscherer, S. Goetz, C.-B. Huang, T. Brixner, and B. Hecht, "Multimode plasmon excitation and in situ analysis in top-down fabricated nanocircuits," *Phys. Rev. Lett.*, vol. 111, p. 183901, 2013.

[150] J. S. Huang, D. V. Voronine, P. Tuchscherer, T. Brixner, and B. Hecht, "Deterministic spatiotemporal control of optical fields in nanoantennas and plasmonic circuits," *Phys. Rev. B*, vol. 79, p. 195441, 2009.

[151] C. Rewitz, G. Razinskas, P. Geisler, E. Krauss, S. Goetz, M. Pawłowska, B. Hecht, and T. Brixner, "Coherent control of plasmon propagation in a nanocircuit," *Phys. Rev. Applied*, vol. 1, p. 014007, 2014.

[152] P. B. Johnson and R. W. Christy, "Optical constants of the noble metals," *Phys. Rev. B*, vol. 6, pp. 4370–4379, 1972.

[153] W. Bogaerts, R. Baets, P. Dumon, V. Wiaux, S. Beckx, D. Taillaert, B. Luyssaert, J. Van Campenhout, P. Bienstman, and D. Van Thourhout, "Nanophotonic waveguides in silicon-on-insulator fabricated with cmos technology," *J. Lightwave Technol.*, vol. 23, pp. 401–412, 2005.

[154] R. M. Osgood Jr, N. C. Panoiu, J. I. Dadap, X. Liu, X. Chen, I.-W. Hsieh, E. Dulkeith, W. M. J. Green, and Y. A. Vlasov, "Engineering nonlinearities in nanoscale optical systems: physics and applications in dispersion-engineered silicon nanophotonic wires," *Adv. Opt. Photon.*, vol. 1, pp. 162–235, 2009.

[155] R. Yan, D. Gargas, and P. Yang, "Nanowire photonics," *Nature Photon.*, vol. 3, pp. 569–576, 2009.

[156] J. Leuthold, C. Koos, and W. Freude, "Nonlinear silicon photonics," *Nature Photon.*, vol. 4, pp. 535–544, 2010.

[157] B. A. Daniel and G. P. Agrawal, "Dependence of dispersive and birefringence properties of silicon nanowires on waveguide dimensions," *Opt. Lett.*, vol. 35, pp. 190–192, 2010.

[158] E. D. Palik, ed., *Handbook of Optical Constants of Solids*. Academic Press, 1999.

[159] I. H. Malitson, "Interspecimen comparison of the refractive index of fused silica," *J. Opt. Soc. Am.*, vol. 55, pp. 1205–1208, 1965.

[160] E. Dulkeith, F. Xia, L. Schares, W. M. J. Green, and Y. A. Vlasov, "Group index and group velocity dispersion in silicon-on-insulator photonic wires," *Opt. Express*, vol. 14, pp. 3853–3863, 2006.

[161] J. Jágerská, N. Le Thomas, R. Houdré, J. Bolten, C. Moormann, T. Wahlbrink, J. Čtyroký, M. Waldow, and M. Först, "Dispersion properties of silicon nanophotonic waveguides investigated with fourier optics," *Opt. Lett.*, vol. 32, pp. 2723–2725, 2007.

[162] A. C. Turner, C. Manolatou, B. S. Schmidt, M. Lipson, M. A. Foster, J. E. Sharping, and A. L. Gaeta, "Tailored anomalous group-velocity dispersion in silicon channel waveguides," *Opt. Express*, vol. 14, pp. 4357–4362, 2006.

[163] M. Wulf, D. M. Beggs, N. Rotenberg, and L. Kuipers, "Unravelling nonlinear spectral evolution using nanoscale photonic near-field point-to-point measurements," *Nano Lett.*, vol. 13, pp. 5858–5865, 2013.

[164] B. Steinberger, A. Hohenau, H. Ditlbacher, A. L. Stepanov, A. Drezet, F. R. Aussenegg, A. Leitner, and J. R. Krenn, "Dielectric stripes on gold as surface plasmon waveguides," *Appl. Phys. Lett.*, vol. 88, p. 094104, 2006.

[165] R. F. Oulton, V. J. Sorger, D. A. Genov, D. F. P. Pile, and X. Zhang, "A hybrid plasmonic waveguide for subwavelength confinement and long-range propagation," *Nature Photon.*, vol. 2, pp. 496–500, 2008.

[166] J.-C. Diels and W. Rudolph, *Ultrashort Laser Pulse Phenomena*. Academic Press, 2006.

[167] S.-D. Yang, A. M. Weiner, K. R. Parameswaran, and M. M. Fejer, "400-photon-per-pulse ultrashort pulse autocorrelationmeasurement with aperiodically poled lithium niobate waveguidesat 1.55 μm," *Opt. Lett.*, vol. 29, pp. 2070–2072, 2004.

[168] S.-D. Yang, A. M. Weiner, K. R. Parameswaran, and M. M. Fejer, "Ultrasensitive second-harmonic generation frequency-resolved optical gating by aperiodically poled linbo3 waveguides at 1.5 μm," *Opt. Lett.*, vol. 30, pp. 2164–2166, 2005.

[169] J. Zhang, A. Shreenath, M. Kimmel, E. Zeek, R. Trebino, and S. Link, "Measurement of the intensity and phase of attojoule femtosecond light pulses using optical-parametric-amplification cross-correlation frequency-resolved optical gating," *Opt. Express*, vol. 11, pp. 601–609, 2003.

[170] C. Webb and J. Jones, eds., *Handbook of Laser Technology and Applications*. CRC Press, 2003.

[171] R. Robert, ed., *The Supercontinuum Laser Source*. Springer, 2006.

[172] X. Fang, M. Hu, L. Huang, L. Chai, N. Dai, J. Li, A. Y. Tashchilina, A. M. Zheltikov, and C. Wang, "Multiwatt octave-spanning supercontinuum generation in multicore photonic-crystal fiber," *Opt. Lett.*, vol. 37, pp. 2292–2294, 2012.

[173] H. Kano and H. Hamaguchi, "Characterization of a supercontinuum generated from a photonic crystal fiber and its application to coherent raman spectroscopy," *Opt. Lett.*, vol. 28, pp. 2360–2362, 2003.

[174] B. Schenkel, R. Paschotta, and U. Keller, "Pulse compression with supercontinuum generation in microstructure fibers," *J. Opt. Soc. Am. B*, vol. 22, pp. 687–693, 2005.

[175] Y. Deng, Q. Lin, F. Lu, G. P. Agrawal, and W. H. Knox, "Broadly tunable femtosecond parametric oscillator using a photonic crystal fiber," *Opt. Lett.*, vol. 30, pp. 1234–1236, 2005.

[176] T. Morioka, H. Takara, S. Kawanishi, O. Kamatani, K. Takiguchi, K. Uchiyama, M. Saruwatari, H. Takahashi, M. Yamada, T. Kanamori, and H. Ono, "1 tbit/s (100 gbit/s × 10 channel) otdm/wdm transmission using a single supercontinuum wdm source," *Electron. Lett.*, vol. 32, pp. 906–907, 1996.

[177] P. Mamyshev, "All-optical data regeneration based on self-phase modulation effect," in *24th European Conference on Optical Communication*, vol. 1, pp. 475–476, 1998.

[178] E. Ciaramella, F. Curti, and S. Trillo, "All-optical signal reshaping by means of four-wave mixing in optical fibers," *IEEE Photon. Technol. Lett.*, vol. 13, pp. 142–144, 2001.

[179] M. Ebnali-Heidari, C. Monat, C. Grillet, and M. K. Moravvej-Farshi, "A proposal for enhancing four-wave mixing in slow light engineered photonic crystal waveguides and its application to optical regeneration," *Opt. Express*, vol. 17, pp. 18340–18353, 2009.

[180] A. Marini, M. Conforti, G. D. Valle, H. W. Lee, T. X. Tran, W. Chang, M. A. Schmidt, S. Longhi, P. S. J. Russell, and F. Biancalana, "Ultrafast nonlinear dynamics of surface plasmon polaritons in gold nanowires due to the intrinsic nonlinearity of metals," *New J. Phys.*, vol. 15, p. 013033, 2013.

[181] J. Renger, R. Quidant, N. van Hulst, and L. Novotny, "Surface-enhanced nonlinear four-wave mixing," *Phys. Rev. Lett.*, vol. 104, p. 046803, 2010.

[182] I. De Leon, J. E. Sipe, and R. W. Boyd, "Self-phase-modulation of surface plasmon polaritons," *Phys. Rev. A*, vol. 89, p. 013855, 2014.

Summary

Optical communication systems are the backbone of the internet, which is the number one information source for our society. Currently, most switching and routing of the light signals in these systems is performed by electronics. This electronic step is the bottleneck for further increasing the data rate. All-optical signal processing, i.e., the control of light with light, can potentially overcome this problem. The most promising way for light beams to interact is to exploit nonlinear optical effects. Unfortunately, nonlinear light-matter interaction is usually very weak and inefficient. One way to significantly enhance the efficiency of nonlinear optical effects is to confine ultrashort light pulses spatially, for example, in a nanophotonic waveguide. Two of the most promising structures that confine light are the photonic crystal waveguide and the plasmonic waveguide.

Researchers have already implemented various all-optical components like switches, routers or memories, which are crucial for signal processing. The next step will consist of integrating these components onto a compact photonic chip. For designing and guaranteeing the functionality of such a complicated all-optical signal-processing chip the propagation of the light pulse inside the constituent nanophotonic structures has to be understood in detail. The common way to characterize waveguiding structures is to measure the properties of the light pulse before and after the structure. Unfortunately, when nonlinear optical effects occur in the photonic chip such an approach fails. The problem is that the superposition principle does not hold in the presence of a nonlinear response and therefore the system cannot be characterized by a single transfer function. More complications arise in the nonlinear optical regime not only because a zoo of effects can occur during light propagation, but that it matters in which sequence these nonlinear plus linear effects occur. For the photonic chip this means, for example, that not only the functionalities of the different components matter, but also in which order they are arranged. As a conse-

quence, a measurement tool is required that allows the direct measurement of the light inside the waveguiding structure to gain additional information that is usually hidden in conventional transmission experiments.

The goal of this thesis is to investigate nonlinear pulse propagation in waveguides. The tool that we use for this investigation is near-field optical microscopy. In chapter 2 we first illustrate the different benefits of this measurement technique. We show that near-field optical microscopy allows the local study of all crucial properties of a light pulse confined in a waveguide. Its phase, its temporal structure as well as its spectral density can be extracted in a non-invasive manner with a subwavelength resolution.

In chapter 3 we address the problem of extracting the characteristics of a single component of a more complex photonic chip, when nonlinear effects have to be taken into account. We demonstrate that we can track the evolution of the spectral density of a pulse as it propagates inside a photonic crystal waveguide, which is part of a more complicated structure. This waveguide slows light down and therefore enhances the efficiency of nonlinear optical effects. We compare the information gained from the local near-field microscopy measurements with transmission measurements. The comparison reveals that the tracking of the spectral density locally allows the understanding of the effects occurring inside the photonic crystal waveguide without the need to take the remaining components of the photonic chip into account, as is the case for the transmission measurement. This result shows the potential of spectrally-resolved near-field microscopy to characterize single components on integrated structures and will allow the design of more complex all-optical signal-processing circuits.

During nonlinear pulse propagation the spectral density of the light often changes. In the most extreme case, a supercontinuum spectrum is generated. Here, the spectral density of the light has broadened extremely, allowing, for example, for spatially coherent white light sources. These light sources are very beneficial for a wide range of applications from spectroscopy to frequency metrology. One way that supercontinuum generation can occur is through a soliton fission event. A soliton is a nonlinear wave, which does not change its temporal structure as it propagates. In a soliton fission event such a nonlinear wave breaks apart into several other wave packets. Soliton fission and concurrent supercontinuum generation is usually investigated in meter long optical fibers.

In chapter 4 we demonstrate that such a soliton fission can also occur

in a millimeter long photonic crystal waveguide and we can visualize the phenomenon with a time-resolved near-field microscope. We show with measurements that we can generate a soliton in the structure, which breaks apart into several wave packets after a record short propagation length. By numerical modeling we prove that the fission occurs because of the presence of free carriers. This work paves the way for the creation of compact white light sources on chip, due to the easy integration of a photonic crystal waveguide into a more complicated photonic circuit.

One problem in pulse propagation is temporal reshaping of the pulse, which usually results in temporal broadening. This temporal broadening leads to a decay of the peak amplitude and hence is detrimental for exploiting nonlinear optical effects.

Chapter 5 deals with the investigation of utrashort-pulse propagation, down to a temporal pulse length of a few femtoseconds, in a plasmonic waveguide on glass. Plasmonic waveguides are interesting for nonlinear optics, since they can confine light to arbitrarily small cross-sections. We compare the waveguiding properties of the gold structure with that of a silicon nanowire, which is a common waveguide in photonics. We prove that the plasmonic waveguide can confine light to much smaller cross-sections down to the nanometer scale. Further, we reveal that an ultrashort pulse does not reshape in the plasmonic waveguide in contrast to the silicon nanowire. As a consequence, the metallic strip is an interesting platform for performing nonlinear optical experiments.

Finally, we discuss in chapter 6 the implications of the results of this thesis. First, we present possible approaches to enhance the capabilities of a near-field microscope to characterize the temporal structure of a pulse. The resulting knowledge about the exact shape of the pulse is crucial for improved investigation of nanophotonic circuits. Further, we propose to create a compact on-chip white-light source by using supercontinuum generation in a photonic crystal waveguide. Lastly, we identify the possibilities of exploiting the knowledge gained in this thesis in all-optical communication circuits. We outline how an optical regenerator, which is a device that amplifies light pulses, can be realized using nonlinear pulse propagation in a photonic crystal or a plasmonic waveguide.

Samenvatting*

Optische communicatiesystemen vormen de ruggengraat van het internet, de grootste bron van informatie voor onze samenleving. Terwijl het transport van deze informatie met licht in glasvezels geschiedt, worden de optische signalen in deze systemen op dit moment nog steeds grotendeels met elektronica geschakeld en gerout. Deze elektronische stap is het knelpunt voor een vergroting van de datasnelheid. Volledig optische gegevensverwerking, bijvoorbeeld door middel van het schakelen van licht met licht, zou dit probleem kunnen verhelpen. De meest veelbelovende manier om lichtbundels op elkaar te laten inwerken is door middel van niet-lineaire optische effecten. Echter, deze effecten zijn typisch zwak en niet efficiënt. Een manier om de efficiëntie van niet-lineaire effecten te vergroten is door ultrakorte pulsen in de ruimte concentreren, bijvoorbeeld, in een nanofotonische golfgeleider. Twee van de meest veelbelovende structuren om licht mee te concentreren zijn de fotonisch kristal golfgeleider en de plasmonische golfgeleider.

Onderzoekers hebben inmiddels verschillende, volledig optische, componenten ontwikkeld, zoals schakelaars, routers en geheugens, die cruciaal zijn voor optische gegevensverwerking. De volgende stap is de integratie van deze componenten in een compacte fotonische chip. Om een dergelijke complexe, volledig optische chip te ontwerpen en de functionaliteit ervan te garanderen, moet de voortplanting van de lichtpuls in de nanofotonische structuren die de basis van de chip vormen, in detail worden begrepen. De meest gebruikelijke manier om golfgeleidende structuren te karakteriseren is door de eigenschappen van de lichtpuls voor en na de structuur te meten. Echter, een dergelijke aanpak volstaat niet als niet als niet-lineaire optische effecten plaatsvinden in de optische chip. Het probleem is dat het superpositiebeginsel niet geldt als niet-lineaire optsiche effecten plaatsvinden en daarom het systeem niet langer kan worden beschreven door een enkele

*Translated by Boris le Feber

overdrachtsfunctie. Meer complicaties ontstaan in het niet-lienaire regime niet alleen omdat een breed scala aan effecten kan plaatsvinden gedurende lichtpropagatie, maar ook omdat de volgorde waarin niet-lineaire en lineaire effecten plaatsvinden van invloed is. Voor de fotonische chip betekent dit dat bijvoorbeeld niet alleen de functionaliteiten van de verschillende componenten belangrijk zijn, maar dat het ook belangrijk is welke volgorde zij zijn gerangschikt. Om de informatie te verkrijgen die verborgen blijft in gebruikelijke transmissie metingen, is een meetinstrument noodzakelijk dat een directe meting van het licht in een golfgeleidende structuur mogelijk maakt.

Het doel van deze thesis is om niet-lineaire optische pulspropagatie in nanofotonische golfgeleiders te onderzoeken. Het instrument dat wij daarvoor gebruiken is een nabije-veld microscoop. In hoofdstuk 2 beschrijven wij de verschillende voordelen van deze meettechniek. Wij tonen aan dat nabije-veld microscopie het mogelijk maakt om lokaal de cruciale eigenschappen van een lichtpuls die is opgesloten in een golfgeleider, te bestuderen. De fase, de evolutie in de tijd, en het spectrum van het licht in de structuur kunnen met een resolutie beter dan de golflengte van het licht worden gemeten.

In hoofdstuk 3 behandelen wij het probleem van de karakterisering van een enkele component in een complexere fotonische chip, wanneer niet-lineaire effecten moeten worden meegenomen. Wij volgen de evolutie van het spectrum van een lichtpuls, terwijl de puls propageert door een fotonisch kristal golfgeleider, die deel uit maakt van een complexere structuur. Deze golfgeleider vertraagt licht en versterkt daardoor niet-lineaire optische effecten. Wij vergelijken de informatie vergaard uit de nabije-veld microscopie metingen met transmissie metingen aan de samengestelde structuur. Deze vergelijking toont aan dat het mogelijk is om, door lokaal de evolutie van het spectrum te volgen, de niet-lineaire effecten in een fotonisch kristal golfgeleider te begrijpen, zonder dat het noodzakelijk is om de overige componenten van de chip te beschouwen. Sterker nog, we tonen aan dat door slechts metingen aan de samengestelde structuur te doen, foutieve conclusies over de eigenschappen van de fotonisch kristal golfgeleider gauw gemaakt zijn. Dit resultaat illustreert de kracht van nabije-veld microscopie in de spectrale karakterisatie van individuele componenten van complexe optische chips en zal het mogelijk maken om complexe structuren te ontwerpen voor volledig optische gegevensbewerking.

Over het algemeen verandert het spectrum van een puls gedurende niet-lineaire pulspropagatie. In het meest extreme geval kan een supercontinuüm spectrum worden gecreëerd. In dat geval is het spectrum extreem verbreed, wat bijvoorbeeld ruimtelijk coherente wit lichtbronnen mogelijk maakt. Deze lichtbronnen zijn erg nuttig voor een breed scala aan toepassingen, zoals spectroscopie en frequentie metrologie. Een manier waarop een supercontinuüm kan worden gecreëerd is door middel van solitonsplitsing. Een soliton is een niet-lineaire golf die niet vervormt als functie van de tijd. Als een soliton splitst vervalt een dergelijke niet-lineaire golf in verschillende golfpakketen. Doorgaans worden solitonsplitsing en de creatie van supercontinuüm die daarmee gepaard gaat bestudeerd in optische fibers.

In hoofdstuk 4 tonen wij aan dat solitionsplitsing ook kan plaatsvinden in fotonisch kristal golfgeleider met een lengte van slechts enkele millimeters en dat wij dit verschijnsel tijdsopgelost kunnen visualiseren met een nabije-veld microscoop. Onze metingen tonen aan dat wij een soliton kunnen creëren die na een recordbrekend korte afstand in verscheidene golfpaketten opsplitst. Met behulp van numerieke modellen bewijzen wij dat deze opsplitsing plaatsvindt dankzij de aanwezigheid van vrije ladingsdragers. Omdat fotonisch kristal golfgeleiders eenvoudig in een optische chip kunnen worden geïntegreerd, is dit werk een grote stap in de richting van de integratie van compacte wit-licht bronnen in een optische chip.

Een probleem in de controle over pulspropagatie is dat de puls vervormt in de tijd, dit leidt meestal tot een langere puls. Omdat de intensiteit van de puls over een langere tijd wordt verdeeld, neemt maximale intensiteit in de puls af, wat zeer ten nadele van niet-lineaire effecten is.

In hoofdstuk 5 bestuderen wij de propagatie van ultrakorte pulsen, met een duur van slechts enkele femtoseconden in een plasmonische golfgeleider. Plasmonische golfgeleiders zijn interessant voor niet-lineaire optica omdat zij licht kunnen samenpersen tot willekeurig kleine doorsnedes. Wij vergelijken de eigenschapen van de plasmonische golfgeleider met die van een vaak gebruikte fotonische golfgeleider: een silicium nanodraad. Wij laten zien dat een plasmonische golfgeleider licht kan samenpersen tot nanoschaal doorsnedes. Bovendien tonen wij aan dat de puls niet vervormt in de plasmonische golfgeleider, maar wel in de silicium nanodraad. Als gevolg hiervan, is een metalen draad golfgeleider een interessant platform voor niet-lineaire optische experimenten.

Tot slot, bespreken wij in hoofdstuk 6 een antal implicaties van de re-

sultaten uit dit proefschrift. Als eerste presenteren wij mogelijke manieren om de mogelijkheden van tijdsopgeloste pulskarakterisatie met een nabijeveld microscoop te verbeteren. De kennis van de precieze vorm van een puls is cruciaal voor een verbeterd onderzoek aan nanofotonische structuren. Vervolgens beschrijven wij een mogelijke compacte wit-licht bron die gebruikt maakt van supercontinuüm generatie in een fotonisch kristal golfgeleider. Tot slot, identificeren wij verscheidene mogelijke toepassingen van de kennis die in deze thesis is vergaard. We beschrijven hoe een optische regenerator, een structuur die lichtpulsen versterkt, gerealiseerd kan worden met behulp van niet-lineare pulspropagatie in een fotonisch kristal of plasmonische golfgeleider.

Acknowledgements

In my opinion the time that research can be performed alone in an ivory tower is over. Nowadays most scientific results are achieved in big collaborations like the one operating the large hadron collider. Consequently, also my thesis is not only the result of my efforts, but I got help from an enormous amount of people, which I would like to thank here. Due to the large number of people, which were involved in performing the research leading to this thesis, it is not possible for me to make an exhaustive list. Consequently, I am sorry for the people that are not mentioned here for the sake of brevity.

First and foremost I would like to express my gratitude towards my supervisor. Without you, Kobus, this thesis would simply have not been possible. You guided me through the scientific forest and taught me to be an independent scientist. You are a great supervisor with a huge experience how to educate, motivate and supervise students. For example, you were always giving me the right comment in all situations: when I was too enthusiastic you gave me the right amount of criticism to bring me down to earth and when I was too depressed you encouraged me to continue to solve the problem. You were also very understanding and helpful concerning the various problems not related to science. For all of this and in general for giving a German electrical engineer a chance to do his PhD in physics I say thank you.

I am also very grateful for all the things I learned from the various member of the NanoOptics group. Nir, I would like to thank you for all the hard lessons I had to learn about how to write an article. It was not always enjoyable for me, but I learned a lot. Further, I would like to thank you for the help in analyzing data and the countless small advices I got from you for the daily lab work. I am also very grateful to you, Daryl, for the time you spent with in the lab to realign Phantom. Without you it would have been just a mess. Moreover, you taught me a lot about

photonic crystals. Boris, you were my long-standing comrade in the fight with the Phantom. We both struggled with the experimental challenges of near-field microscopy and the challenge to interpret the data. Also thanks for translating my summary and being my paranymph. Marko and Aron, I am indebted to you for teaching me the secrets of the Phantom and how to glue tips. Anouk, thank you for your help in performing nonlinear plasmonic experiments, especially for the fact that you borrowed me your sample. I am sorry that I destroyed most of the structures on it. I am very grateful for the group meetings, where I learned a lot, especially how to give a coherent presentation. For the endless and valuable comments I got I am very grateful to Ruben, Hakki, Lorenzo, Dries, Tobias and Jean. I also would like to thank the master and bachelor students that were in our group. I am especially indebted to Leon, whose master thesis I had the pleasure to supervise.

Chad, I would like to thank you for the very productive and enjoyable collaboration. You taught me a lot about science and performing an experiment during your visit at AMOLF. I also enjoyed the time we spent together. Moreover, I would like to thank you for the numerous modeling calculations you performed for our soliton fission experiment.

I enjoyed nearly every day at AMOLF due to the great office mates I had. Thank you Andrej, James, Nicolas, Amira, Mengqi and Hugo. I am especially very grateful for having Andrej sitting nearly four years across my desk. Thank you, Andrej, for all the useful, funny or sometimes weird conversations and for being my paranymph.

I would like to thank all members of the Center of Nanophotonics. I was taught a lot during our colloquium and poster meetings, among other things how to ask challenging questions. Furthermore, I enjoyed the endless discussions during the coffee and lunch breaks with you guys. I would like to acknowledge especially the Resonant Nanophotonics group, which had a joint meeting with our group for some time.

AMOLF is such a great place for scientists due to the extremely helpful support staff. There is a department responsible for every area of expertise necessary like software, electrical engineering or ICT. I am very grateful for all the support I got from our group technician Hinco. Thank you for all the prompt problem solutions and the perfect tips. Further, I would like to thank Marco and Sjoerd for numerous software bug fixes and Idsart for solving all kind of electronic issues. I also would like to thank Gijs

and Peter for the fabrication of nanowire samples for me. Henk-Jan, I am grateful for your work on the cover design. I am also indebted to the AMOLF management and housing team, which helped me to find a nice place to stay in Amsterdam.

The other things, which made my stay at AMOLF so enjoyable, were the social activities I undertook with my fellow researchers. Thank you Chris, Bergin, Lutz, Nuria, Sophie, Jeanette, Jochen and Clara for letting me feel welcome and at home in the Netherlands.

Ich möchte mich auch bei allen meinen Freunden in Deutschland dafür bedanken, dass sie mit mir Kontakt gehalten haben. Ihr habt dafür gesorgt, dass ich nicht ganz den Kontakt zur "normalen" Welt verloren habe und dass ich meine zahlreichen Besuche in der Heimat genossen habe.

Bei meinen Eltern und meinem Bruder mit seiner Familie möchte ich mich für ihre Liebe und grenzenlose Unterstützung bedanken. Vor allem euch, Mama und Papa, schulde ich viel Dank, da ihr diese Arbeit erst ermöglicht habt. Ihr habt mein Studium finanziert und mir in allen Dingen geholfen, wenn ich Hilfe nötig hatte, dafür vielen Dank.

Finally I would like to thank you, Ioana. You are the best thing that happened to me during my time at AMOLF. I am grateful for all the support you gave me and for the fact that you are just there for me. Now we both have to move on and we will make this big step in the unknown together. It is scary to start something new, but I am confident we can manage all problems together.